WIDE ACCEPTANCE ANGLE OPTICAL FIBER BASED DAYLIGHTING SYSTEM USING TWO-STAGE REFLECTIVE NON-IMAGING SOLAR CONCENTRATOR

By

ONUBOGU NNEKA OBIANUJU

A dissertation submitted to the Department of Electrical and Electronics Engineering, Lee Kong Chian Faculty of Engineering Science, University Tunku Abdul Rahman, in partial fulfillment of the requirements for the degree of Master of Engineering Science

November 2017

ABSTRACT

WIDE ACCEPTANCE ANGLE OPTICAL FIBER-BASED DAYLIGHTING SYSTEM USING TWO-STAGE REFLECTIVE NON-IMAGING SOLAR CONCENTRATOR

Onubogu Nneka Obianuju

Electric lighting systems in buildings account for 20% of the total global energy consumption, causing an enormous amount of CO_2 emissions even during the daytime. Thus, daylighting systems have been designed and developed to save energy and reduce CO_2 emissions. Daylighting systems use sunlight to illuminate a building via optical fibers, light pipes, etc. Daylight transmission via optical fibers has been proven to be more effective. However, most of the existing fiber-optics daylighting systems have a high manufacturing cost, low tolerance to sun pointing error and a complicated optical system having many stages of focusing in order to improve the uniformity of focused sunlight. As a contribution to the existing fiber-optics daylighting systems and to curb these problems, this study presents a novel fiber-optics active daylighting system using two-stage reflective non-imaging solar concentrator (NISC). The prototype of two-stage reflective NISC comprises a primary reflector with 80 primary facet mirrors of dimension 5 cm × 5 cm each, a secondary reflector 70 cm above the primary reflector with 20 secondary facet mirrors of dimension 8 cm × 8 cm each and plastic optical fibers for light transmission. The prototype with a collective area of

0.2 m^2 can capture solar power of 170 W which is equivalent to a power conversion efficiency of 21.4 % and is capable of uniformly illuminating a 7.56 m^2 office area with an average illuminance of 500 lx. Economic analysis was carried out on a proposed prototype collective area of 4 m^2, giving a total estimated manufacturing cost of USD 1231.20, a total payback period of 6.4 years based on the interest rate of 4 % and fuel inflation rate of 2 % and life-span of about 15 years.

ACKNOWLEDGEMENT

I would like to express my most sincere gratitude and deepest appreciation to my main supervisor Prof. Chong Kok-Keong who has the attitude and substance of a genius. I thank him for all his guidance, support, advice, motivation and drive towards making me think critically to become a better researcher. He steered me in the right direction when he noticed I went the wrong way.

My sincere appreciation goes to my co-supervisor Dr. Pua Chang Hong who always welcomed me to his office whenever I needed help or had any questions regarding my research. He was very supportive, gave me great ideas and helped me realize my mistakes.

I would also like to thank my Final Year Project students: Wong Chong Chiat, Ooi Wai Cheng, Zhe Kai Lee and Chua Tiong Chuan who all cooperated and worked with me in building the prototype. More so, my sincere gratitude goes to my research partners: Dr. Yew Tiong-Keat, Dr. Wong Chee Woon, and Weoi-Chong Tan. They helped me in performing some roof-top experiments, provided me free tutorials on LightTools software and gave me ideas in making the project work. I would also like to acknowledge Dr. Lai Soon Onn, Dr. Lim Boon Han, Dr. Ezra Morris and all Lab Assistants and Technicians for their kind support and advice all through the project.

Finally, I must express my profound gratitude to my family and friends; most especially my father: Engr. Godwin Onubogu for all his advice, contributions and great ideas towards the project. My mother, fiancé, and siblings all provided me with unfailing support and continuous encouragement throughout the research duration. This project execution would not have been possible without you all. Thank you.

APPROVAL SHEET

The thesis entitled "**WIDE ACCEPTANCE ANGLE OPTICAL FIBER-BASED DAYLIGHTING SYSTEM USING TWO-STAGE REFLECTIVE NON-IMAGING SOLAR CONCENTRATOR**" was prepared by ONUBOGU NNEKA OBIANUJU and submitted as partial fulfillment of the requirements for the degree of Master of Engineering and Science at Universiti Tunku Abdul Rahman.

Approved by:

_____
(Prof. CHONG KOK KEONG)
Date:……....
Professor / Supervisor
Department of Electrical and Electronic Engineering
Faculty of Engineering and Science
Universiti Tunku Abdul Rahman

_____
(Dr. PUA CHANG HONG)
Date:……....
Co-supervisor
Department of Electrical and Electronic Engineering
Faculty of Engineering and Science
Universiti Tunku Abdul Rahman

FACULTY OF ENGINEERING AND SCIENCE

UNIVERSITI TUNKU ABDUL RAHMAN

Date: _____

SUBMISSION OF THESIS

It is hereby certified that **Onubogu Nneka Obianuju** (ID No: **15UEM07678**) has completed this thesis entitled " WIDE ACCEPTANCE ANGLE OPTICAL FIBRE-BASED DAYLIGHTING SYSTEM USING TWO-STAGE REFLECTIVE NON-IMAGING SOLAR CONCENTRATOR" under the supervision of Prof. Chong Kok-Keong (Supervisor) from the Department of Electrical and Electronics Engineering, Faculty of Engineering and Science, and Dr. Pua Chang Hong (Co-Supervisor) from the Department of Electrical and Electronics Engineering, Faculty of Engineering and Science.

I understand that the University will upload a softcopy of my thesis in pdf format into UTAR Institutional Repository, which may be made accessible to UTAR community and the public.

Yours truly,

_____

(*ONUBOGU NNEKA OBIANUJU)*

DECLARATION

I, ONUBOGU NNEKA OBIANUJU hereby declare that this thesis is based on my original work except for quotations and citations which have been duly acknowledged. I also declare that it has not been previously or concurrently submitted for any other degree at UTAR or other institutions.

Name: ONUBOGU NNEKA OBIANUJU

Date _____

TABLE OF CONTENTS

LIST OF TABLES

LIST OF FIGURES

LIST OF ABBREVIATIONS

C_{avg}	Average solar concentration ratio (suns)
A_{fiber}	Cross-sectional area of plastic optical fiber (m^2)
CPV	Concentrator photovoltaic
dB/km	Decibel per Kilometer
dB/m	Decibel per milliwatt
2-D	2-dimensional
3-D	3-dimensional
V_{DNI}	DNI voltage (V)
DNI or **I**	Direct normal irradiance (W/m^2)
GSI	Global Solar Irradiance (W/m^2)
V_{GSI}	GSI voltage (V)
θ_1	Incident angle of the incident sunray relative to the primary facet mirror (˚)
θ_2	Incident angle of incident sunray relative to the secondary facet mirror (˚)
A_{illum}	Indoor illumination area (m^2)
kWh	Kilowatt hours
lm	Lumen
lm/W	Lumen per Watt
lx	Lux
$C_{measured}$	Measured solar concentration ratio (suns)
Mt	Million tons
mrad	milliradian

ΔV_{DNI}	Measurement error of DNI voltage
ΔV_{GSI}	Measurement error of GSI voltage
$\Delta I_{\mathrm{sc\text{-}1}}$	Measurement error of short circuit current 1
$\Delta I_{\mathrm{sc\text{-}2}}$	Measurement error of short circuit current 2
$\Delta \mathrm{C}_{\mathrm{measured}}$	Measurement error of solar concentration ratio (number of suns)
NIDC	Non-imaging dish concentrator
NIPC	Non-imaging planar concentrator
NISC	Non-imaging solar concentrator
N_{fiber}	Number of plastic optical fibers
% *VL*	Percentage of visible light in the solar spectrum (%)
POF	Plastic Optical Fiber
R_{facet}	Reflectivity of primary/secondary facet mirror (%)
Rpm	Revolutions per minute
$I_{\mathrm{sc\text{-}1}}$	Short-circuit current of concentrated solar flux (CPV cell 1) (A)
$I_{\mathrm{sc\text{-}2}}{}^{\mathrm{DNI}}$	Short-circuit current of CPV cell 2 contributed by DNI only (A)
TWh	Terawatt hours
E_{L}	The average value of direct beam luminous efficacy (lm/W)
L	The distance between the primary reflector and the secondary reflector (cm) = 70 cm
$\mathrm{Illum}_{\mathrm{theo}}$	Theoretical result of indoor illuminance (lux)
T	Thickness (cm)
L_{fiber}	Total transmission loss via fiber (%)
$T_{\mathrm{hot\ mirror}}$	Transmissivity of hot mirror to visible light (%)
$\hat{I}$	Unit vector of the incident sunray

$\hat{I}'$	Unit vector of the incident sunray on the secondary facet mirror from point **A**
$\hat{R}$	Unit vector of the reflected sunray from point **M** to the point **C**
$\hat{R}'$	Unit vector of the reflected sunray from the secondary facet mirror at point **B** to the target at point **O**
$\hat{N}$	Unit vector normal to the primary facet mirror
$\hat{N}'$	Unit vector normal to the secondary facet mirror
W	Width (mm or cm)
W/m^2	Watt/m^2

Greek symbols:

α	$\angle ACD = \angle ABF$
β	$\angle ADE = \angle AFG$
ω	Half rim angle (˚)
σ	Tilted angle of the primary facet mirror along the *x*-axis (˚)
γ	Tilted angle of the primary facet mirror along the *y*-axis (˚)
ϕ	Tilted angle of the secondary facet mirror along the *x*-axis (˚)
ρ	Tilted angle of the secondary facet mirror along the *y*-axis (˚)

CHAPTER 1

INTRODUCTION

1.1 Research Background

Fossil fuels have been relied on for many years till date for power generation. However, the increasing rate of consumption of this non-renewable energy source has led to their depletion and the release of harmful greenhouse gases made up of mostly carbon dioxide into the atmosphere. As a result, renewable sources of energy such as solar energy is being sought after to meet up with the world's growing energy demands.

It has been identified that lighting systems in a building consume a lot of energy even during the day time (Shulman *et al*., 2012). Presently, the lighting energy consumption of buildings is estimated as 30 % of the total energy generated in Malaysia (Al-Mofleh, 2009) and 20% in the world (IEA, 2011). To save building energy consumption, there has been an increasing interest in incorporating daylighting with architectural and building designs to provide natural illumination. The U.S. Green Building Council (1995) estimated that a reduction of about 50-80% of the lighting energy consumption can be achieved with the use of efficient daylighting systems in buildings. Providing daylighting via direct sunlight is a more affordable and eco-friendly way to illuminate a building compared to providing electricity via non-renewable resources. The increase in electric lighting usage will cause a

significant increase in greenhouse gas emissions due to the continuous rise in population and individual comfort demand. This justifies the need to urgently encourage energy conservation in the lighting sector.

Daylighting can be provided in a building either conventionally by using windows, sliding glass doors, skylights, light reflectors and shelves and openings (passive daylighting) or by using daylight capturing and guiding systems (active daylighting). Passive daylighting systems are stationary without solar-tracking technology while active daylighting systems use solar-tracking technology to actively follow the sun to increase the efficiency of light collection and guide light into the building for illumination (Sharp *et al*., 2014; Huang *et al*., 2013). Buildings usually have windows, but the light from the windows decreases very fast and interior areas may have little or no sun exposure making illumination inconsistent as some areas may remain dark. Alrubaih *et al*. (2013) stated that office buildings are required to have an average illuminance of 500 lx based on the UK CIBSE Code for interior lighting. However, with only windows and openings, it is difficult to achieve 500 lx all day long; thus the need for active daylighting systems. The invention and development of active daylighting systems have propagated the interest from passive to active daylighting which are preferably installed on the roof-top of buildings, where sunlight can be easily captured at all times of the day (Ullah and Shin, 2014).

Studies in the past have revealed that various kinds of conventional concentrators such as Fresnel lens, heliostat, parabolic concentrator,

compound parabolic concentrator, etc. have been employed for daylighting and tested with optical fibers coupled to their receivers to guide sunlight into the building (Muhs, 2000; Schlegel *et al*., 2004; Lingfors and Volotinen, 2013; Sapia, 2013; Ullah and Shin, 2013a; Ullah and Shin, 2013b; Ullah and Shin, 2014; Song *et al*., 2014). However, most of these concentrators have a high manufacturing cost, complicated optical system, fixed or high rim angle and/or produce non-uniform concentrated sunlight. Therefore; a novel two-stage reflective non-imaging solar concentrator (NISC) daylighting system consisted of two-stage reflectors and plastic optical fibers as a light transmission system is proposed to solve the existing problems. The two-stage reflective NISC idea was partly derived from the non-imaging focusing technology concentrator photovoltaic system application (Chong *et al*., 2009; Chong et al., 2010; Chong *et al*., 2013; Tan et al., 2014; Siaw *et al*., 2014; Yew *et al*., 2015; Tan and Chong, 2016). Since the design of non-imaging focusing technology was successful in the application of concentrator photovoltaic system, it can also be applied to an active daylighting system.

The two-stage reflective non-imaging solar concentrator daylighting system prototype was constructed and placed on the rooftop of Universiti Tunku Abdul Rahman building in Sungai Long. Mathematical analysis was performed to determine the configuration or alignment of the primary and secondary facet mirrors. Numerical simulation using ray-tracing technique was performed to analyze the concentrated sunlight at the receiver of the concentrator. To validate the simulated results, on-site data collection was carried out using the prototype concentrator.

1.2 Research Objectives

The three objectives of this research are:

1. to develop a two-stage reflective non-imaging solar concentrator (NISC) and its associated optical fiber-based daylight transmission system,
2. to analyze the technical performance of the optical fiber-based daylight transmission system using the non-imaging solar concentrator, and
3. to evaluate the economic viability of the two-stage reflective non-imaging solar concentrator.

1.3 Outline of Thesis

The organization of this thesis is as follows: Chapter 1 gives an introduction to the research, the problem under study and the research objectives. Chapter 2 is a literature review on various existing active daylighting systems using optical fibers for light transmission into the building. Chapter 3 presents an outline of the methods used in this study. Areas covered include: the concept from which the idea of the two-stage reflective NISC design emerged; the 2-D optical design of the two-stage reflective NISC; mathematical derivation of the tilting angles of the primary and secondary mirrors; the 3-D modelling of the prototype, numerical simulation using LightTools software, and prototype construction (inclusive of solar tracking and optical fiber design). In Chapter 4, experimental set-ups and procedures for all experiments are described in detail. The experimental roof-top data collection results are also presented, analyzed and compared with

the numerical simulation results. Chapter 5 elaborates on the design optimization and economic analysis of the two-stage reflective NISC and comparison of the prototype with some existing fiber-optics daylighting systems. Chapter 6 ends the thesis with a summary of the overall research outcome, conclusion and future works.

CHAPTER 2

LITERATURE REVIEW

2.1 Introduction to Daylighting

Visibility is provided by natural sunlight or artificial light (Kubba, 2012). Daylighting can be defined as introducing visible part of sunlight into a building to give a more pleasant indoor environment thus reducing the energy consumption of the building (Alrubaih *et al.*, 2013). Among other renewable sources of energy on earth, the sun is the most essential which is free, available in abundant quantity and is not affected by the everyday increase in the price of energy (Omer, 2008). People seek natural lighting in their houses and workplaces because apart from providing illumination, light has a positive effect on our well-being, safety, confidence, and efficiency (Kubba, 2012).

2.1.1 Percentage of energy consumed by lighting in buildings

As estimated by the U.S. Energy Information Administration (EIA, 2017), the residential and commercial areas in the United States consumed about 279 billion-kilowatt hours (kWh) of electricity for lighting in 2016. This was approximately 10 % of the total electricity used up by the two areas and approximately 7 % of the total electricity consumed in the United States. The Australian Energy Rating Department estimated that 10-12% of the electricity

consumption in residential buildings and 18-40% of the electricity consumption in commercial buildings are attributed to lighting (Energy Rating, 2016). In Malaysia, lighting in buildings consumes approximately 30% of the total energy produced (Al-Mofleh, 2009). Martirano (2011) estimated that average and large-sized buildings in Europe consume about 40 % of the total electrical energy for illumination in the interiors only. Lighting consumes about 132 TWh i.e.15% of the total electricity consumption in South East Asia (TERI, 2014). The International Energy Agency estimated that approximately 20% of the global buildings electricity consumption is attributed to lighting; which is equivalent to the amount of energy generated by nuclear power (IEA, 2011).

2.1.2 Daylighting as a solution to energy conservation in buildings

As lighting is one of the main energy consumers in buildings, ways of conserving lighting energy are being sought after. To achieve energy savings in lighting, the International Energy Agency (IEA, 2011) recommends that governments should encourage improved lighting systems design and management by ensuring that building codes promote daylighting and take account of minimum energy performance standards (MEPS) for lighting systems. As previously stated in the introduction section, efficient daylighting systems in a building can aid in reducing the energy consumption for lighting by 50-80% (U.S Green Building Council, 1995). A cheap and sustainable way to illuminate the interior parts of a building is the use of direct sunlight; instead of using a photovoltaic module to convert solar energy to electrical energy and

then to light energy as the conversion processes involve significant energy losses.

Natural visible light from the sun can be extracted and sent into buildings for daylighting via passive and active daylighting systems. Figure 2.1 illustrates a general idea of both systems. In Fig. 2.1, passive daylighting is illustrated with the use of a window that directly receives sunlight to illuminate the interiors of the ground floor of a building. Active daylighting is illustrated with a tracking solar concentrator that tracks the sun and receives sunlight that is transmitted via a light tube to dark locations in the building that do not have windows such as the basement. The difference between the two is defined by how the energy is collected and distributed as explained in section 1.1.

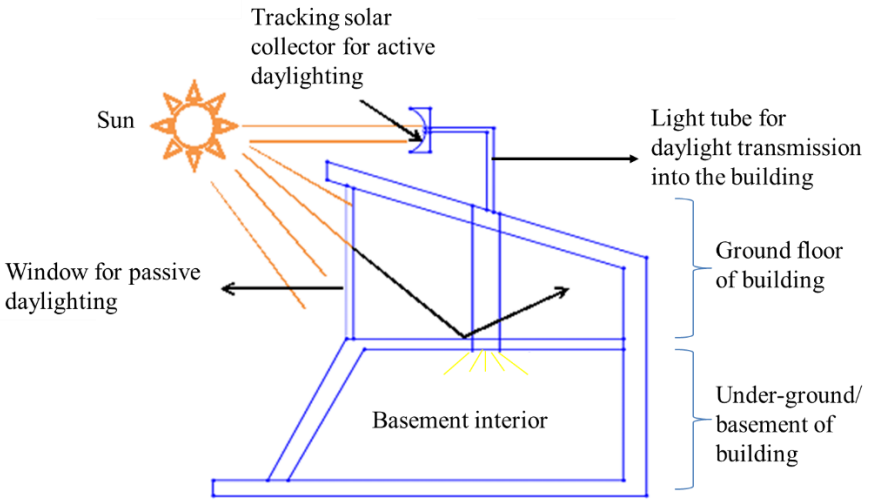

Figure 2.1: Illustration of passive versus active daylighting in a building

Some studies (Elmualim *et al*., 1999; Pohl and Anslem, 2001; Zain-Ahmed *et al*., 2002; Galasiu *et al*, 2004; Ghisi and Tinker, 2006; Jenkins and Newborough, 2007; Chow *et al*., 2013; Berardi, 2015; Ullah and Whang, 2015; Yu *et al*., 2015 and Kim *et al*., 2016) have shown energy conservation via passive and active daylighting systems in buildings. Active daylighting systems have one key advantage over passive daylighting systems which is longer effective hours. With a good sunny weather, an active daylighting system with its sun-tracking devices can start effective daylighting early in the morning and last till later in the day as compared to passive daylighting systems. In this way, light can be successfully sent to parts of the building that do not receive sunlight from passive daylighting systems such as windows. This has dragged the focus to active daylighting systems as they are more efficient. Past studies on active daylighting systems have revealed that various kinds of conventional concentrators, such as parabolic concentrator, compound parabolic concentrator, Fresnel lens, heliostat, etc. exist. These concentrators have been used to concentrate sunlight and transmit it inside the building via optical fibers for illumination. In the following section, some existing fiber-optics active daylighting systems are reviewed.

2.2 Existing fiber-optics active daylighting systems

All active daylighting systems consist of a solar concentrator for focusing sunlight, a receiver for receiving the light and light guides for directing and transmitting the light into the building. A solar concentrator is a

device that receives sunlight from a wide area and concentrates it to a smaller receiver by bending the rays of sunlight (Muhamad-Sukki *et al*., 2010). The focused light can be used for daylighting by coupling optical fibers to the receiver for light transmission. Solar concentrators are generally classified into imaging and non-imaging concentrators. Imaging concentrators such as telescopes, microscopes, parabolic shaped mirrors, etc., do not aim to produce uniform flux distribution profile at the receiver; rather they generate an image. For non-imaging concentrators, all rays entering the entrance aperture must leave the exit aperture thus producing a high concentration ratio and uniform flux distribution on the receiver. This literature reviews active daylighting systems under single-axis sun tracking and double-axis sun tracking. Just as the name implies, a single-axis sun tracking daylighting system tracks the sun in only one direction i.e. they have only one degree of freedom that acts as an axis of rotation. Double-axis tracking daylighting systems have two degrees of freedom that act as an axis of rotation, i.e. they track the sun in two directions (azimuth and elevation) and can therefore make perfect alignment with the sun at all times of the day thus achieving optimum performance all year round (Zafrullah, 2013).

2.2.1 Single-axis sun tracking - Parabolic trough daylighting system

Ullah and Shin (2014) designed a parabolic trough optical fiber-based daylighting system as shown in Figure 2.2 to illuminate the interior of a large-scale multi-floor building. It is a three-stage reflective type of linear focusing design consisting of a parabolic trough, parabolic reflector, and a trough CPC.

The parabolic trough was designed with a rectangular aperture height of 1000 mm and a rectangular aperture width of 570 mm to illuminate a 60 m^2 floor area. The parabolic trough receives sunlight and directs it to the small parabolic reflector, which collimates the light to the non-imaging trough Compound Parabolic Concentrator (CPC) and sends it to the optical fibers. The trough CPC was used to achieve a high concentration of light and is perfectly aligned to the linear array of optical fibers. Since plastic optical fibers (POFs) cannot withstand heat for long, silica optical fibers (SOFs) were coupled before POFs to reduce the heat problem using index matching gel. SOFs have good light transmissibility and heat resistance but are quite expensive; while POFs are flexible, strong, cheap, and acceptable for complex wiring in buildings. A diverging lens (combination of biconcave lens and a concavo convex lens) with a refractive index of 1.459 was employed in distributing the light from the optical fibers into the room. Artificial Light Emitting Diodes (LEDs) were used as a complementary light source to maintain a constant level of illuminance when daylight fell from the required illuminance. The advantage of their proposed system is that it can be made on a large scale; while only requiring one tracking module; nevertheless, it is has a three stage line focused complicated optical design and a high manufacturing cost of more than USD 800/m^2.

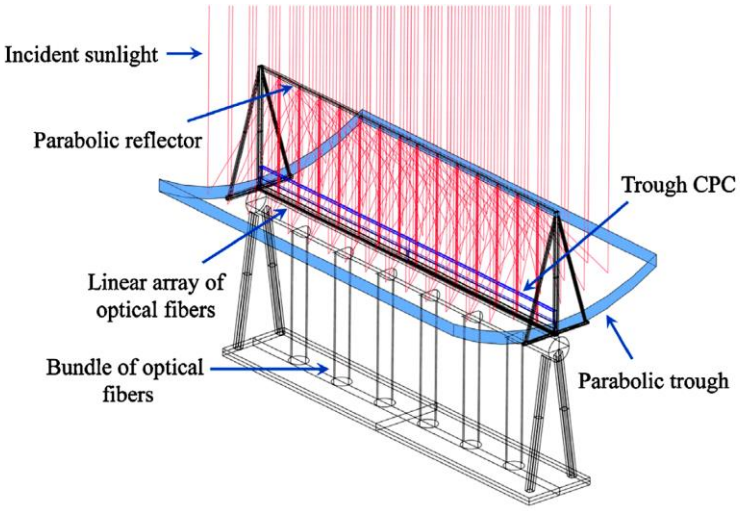

Figure 2.2: Physical layout of the parabolic trough daylighting system (Ullah and Shin, 2014)

2.2.2 Single-axis sun tracking - Linear Fresnel lens daylighting system

Ullah and Shin (2014) proposed and designed a novel approach as shown in Figure 2.3 for the linear Fresnel lens to illuminate a large-scale building interior. It is a three-stage refractive type of linear focusing design consisting of a linear Fresnel lens, collimating plano-concave lens and a trough CPC. Linear Fresnel lens of 570 mm length and 1000 mm width receives direct sunlight and focuses it to the collimating lens. The collimating lens then collimates the light to the receiver which is a linear array of optical fibers. To achieve a high concentration of light, a trough CPC was introduced directly before the optical fibers and properly aligned with the optical fibers. Thus, the collimated light from the collimating lens is guided through the trough CPC and then into the optical fibers. Just like the parabolic trough daylighting system in section 2.2.1, the same daylight transmission and distribution methods were employed. The advantage and disadvantages of this system are

similar to that of the parabolic trough daylighting system, except for its high manufacturing cost which is more than USD 600/m^2. Also, Fresnel lens is generally known to have poor efficiency due to poor hardware design.

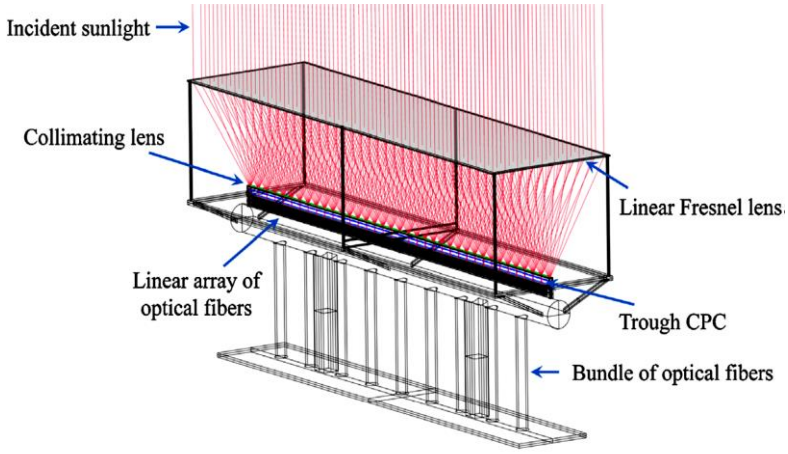

Figure 2.3: Physical layout of the Fresnel lens daylighting system (Ullah and Shin, 2014)

2.2.3 Double-axis sun tracking - Fresnel lens daylighting system

Ullah and Shin (2012, 2013a) demonstrated the possibility of transmitting uniform sunlight to the basement, store rooms, rooms without any windows and different floor areas by capturing sunlight with a linear Fresnel lens of 0.5 mm constant pitch and focusing it on a small area. The Fresnel lens had a length of 300 mm, a width of 300 mm and a focal length of 330 mm. As illustrated in Figure 2.4, direct sunrays received by the Fresnel lens are focused to a collimating plano-concave lens of 16.1 mm diameter and a 21.5 mm focal length. The plano-concave lens uniformly collimates the focused light to a bundle of optical fibers. The optical fibers consisting of SOFs and POFs, then

transmit the light to the destined area. Simulation and experimental result showed that uniform illumination was accomplished in the bundle of optical fibers and the illuminance level of each optical fiber was almost the same. The average illuminance produced by the Fresnel lens daylighting system was 675 lx. More so, when the sunlight level went lower than the required range, LED sources were used as a supplementary light to accomplish the needed illuminance of 500 lx in the room. Photocells were used to detect the available light in the room and their control algorithm retained an average illuminance of 500 lx. The disadvantage of this daylighting system is that a high concentration ratio cannot be achieved because a linear Fresnel reflector normally concentrates less than 100 suns.

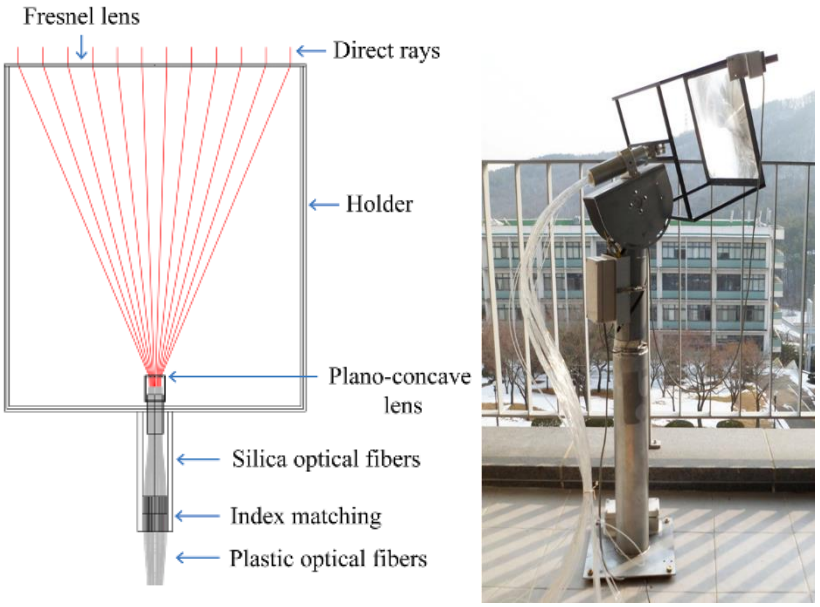

(a) (b)

Figure 2.4: (a.) Structural design of the Fresnel lens solar concentrator daylighting system (b.) Prototype of the Fresnel lens solar concentrator daylighting system with optical fiber for light transmission (Ullah and Shin, 2013a)

Muhs (2000) and Shen *et al*. (2009) presented a similar type of Fresnel lens daylighting system. Shen *et al*. (2009) demonstrated a distinctive and inexpensive way of directing sunlight to dim regions of multi-storey buildings. This hybrid (CPV and daylighting) system captures both the visible and infrared portions of sunlight with a dual-axis sun-tracking Fresnel lens concentrator. The captured sunlight is focused onto solar cells acting as openings of the optical fiber. The optical fibers directly distribute the visible portion of light into the building combined with LED lighting units in specially made luminaries to supplement lighting in the building, if needed. The solar cells transform the infra-red radiation to electricity. Figure 2.5 illustrates the Fresnel lens collector design approach (Muhs, 2000).

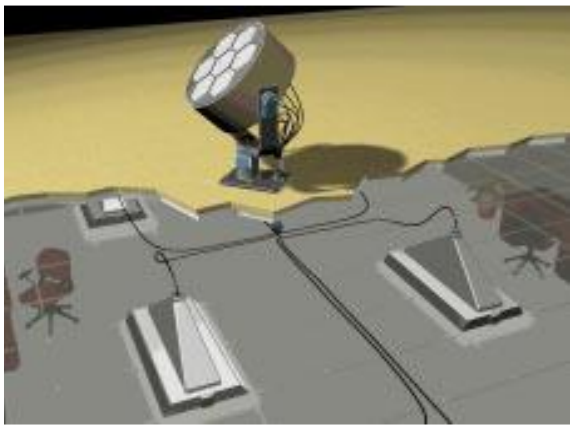

Figure 2.5: Fresnel lens collector hybrid design daylighting approach (Muhs, 2000)

Gilmore (1988) developed two models of the Himawari solar lighting system for small-scale building interiors consisting of a different number of Fresnel lenses and quartz-glass optical fibers (QOFs) in bundles. This daylighting system consists of a sun-tracking device to capture direct sunlight

throughout the day and focus it through Fresnel lens which inserts only visible light into the optical fibers. Six optical fibers were combined in each bundle with an illumination angle of 58^{o} from the fiber bundle. Luminous flux of 1920 lm was obtained per fiber cable. Although quartz-glass optical fibers were used because they exhibit low losses during light transmission, this increased the cost of the system. The uniformity of sunlight at the light capturing and distribution stages were not well defined by Gilmore (1988). The advantage of this system is that Himawari sunlight consists of only a small amount of infrared radiation and thus would not affect the temperature of a room or air cooling systems. However, the new necessity of daylighting systems is to give high illuminance of which Himawari models cannot provide.

Figure 2.6: Himawari solar lighting system
(https://suntomoon.files.wordpress.com/2012/01/img_1626.jpg)

Vu *et al*. (2016) designed and analyzed a "modified optical fiber daylighting system (M-OFDS)" with sunlight transportation in free space. The M-OFDS consists of three parts: a primary concentrator (linear Fresnel lens of 340 mm diameter and a truncated cone shaped plastic optical fiber with 6 mm

core diameter), a collimator (parabolic mirror with a focal length of 4 mm and 50 mm diameter and a 15 mm diameter convex lens with a focal length of 11 mm) and a light guide (directing flat mirrors and two linear Fresnel lenses placed perpendicularly to diffuse parallel light for indoor illumination). As shown in Figure 2.7, Fresnel lens of 340 mm diameter made from PMMA concentrates sunlight and focuses it on the piece of 6 mm diameter plastic optical fiber which transmits the light to the collimator attached at the end of the fiber. The collimated sunlight then travels in open space and is directed to the room by the flat mirrors. The result of their simulation showed 85 % uniformity of light and experimental results showed that each M-OFDS provided approximately 5000 lm with an optical efficiency of 50.7 %. This daylighting system is complicated in optical design as it consists of many stages of optical devices. Also, it cannot be applied where obstacles such as trees exist as they will block the sunrays since it functions only in free space. Furthermore, the total system costs about USD 4272 which is quite expensive for real life implementation.

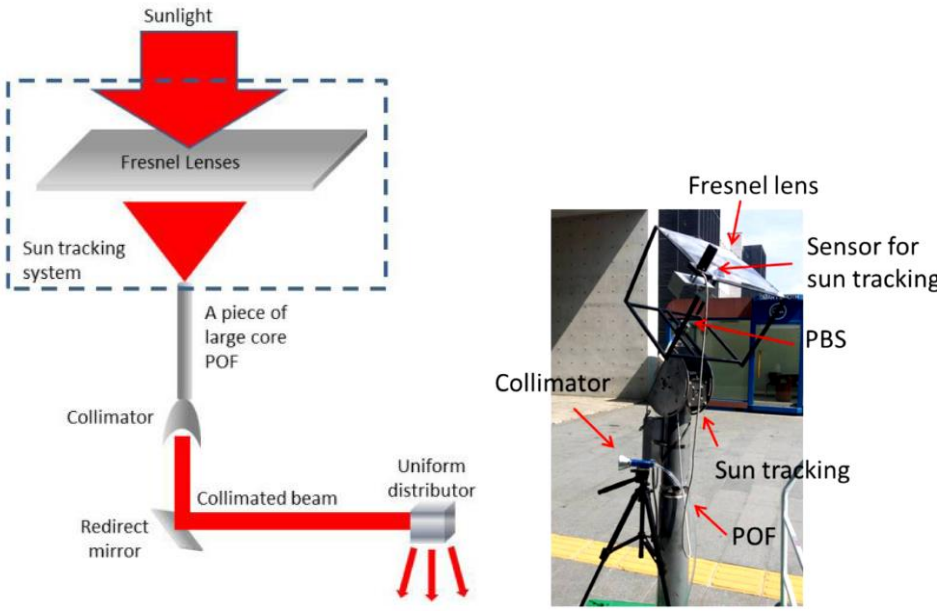

Figure 2.7: Schematic diagram of the M-OFDS (left) and a working prototype of the M-OFDS (right) (Vu *et al*., 2016)

2.2.4 Double–axis sun tracking - Parabolic Dish/mirror

Ullah and Shin (2012, 2013a) proposed and designed a two-axis parabolic mirror fiber-based daylighting system as shown in Figure 2.8. In this approach, a primary concave parabolic mirror with a diameter of 320 mm and a focal length of 128 mm captures sunlight and guides it towards a secondary convex parabolic mirror with a diameter of 13.75 mm (equivalent to the receiver's diameter) and a focal length of 5.5 mm which then collimates the light uniformly to the bundle of optical fibers for indoor illumination. Increasing the diameter of the parabolic mirror would result to a larger reflective surface area thus producing a higher efficiency. The bundle of optical fibers (SOF coupled with POF) is arranged circularly to receive maximum concentrated sunlight and transmit the light uniformly into the building (Ullah and Shin, 2013a). Experimental results indicated that uniform

illumination was obtained in the bundle of optical fibers and an average illuminance of 705 lx was attained in the building and compensated with LEDs when the level of sunlight dropped from the required range. The total cost of this system was not provided.

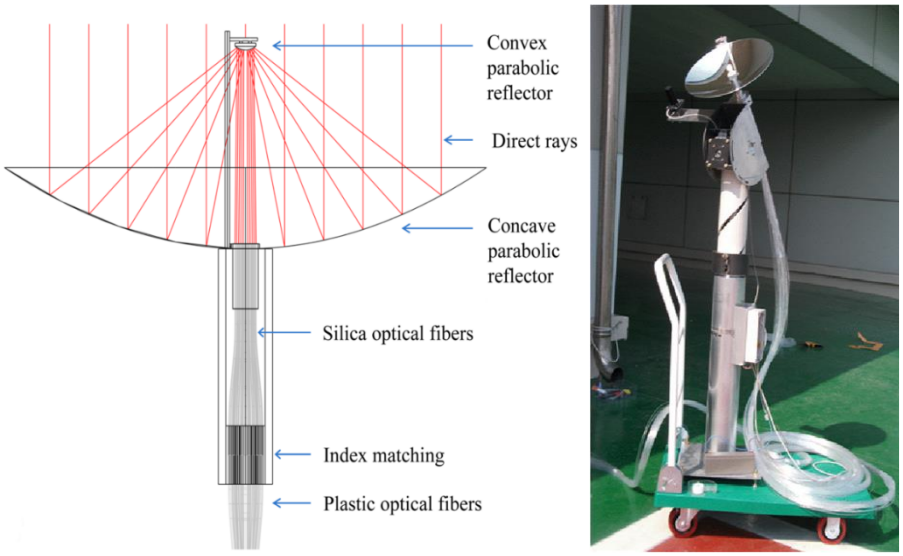

Figure 2.8: Structural design of the parabolic mirror solar concentrator daylighting system (left); Prototype of the parabolic mirror solar concentrator daylighting system with optical fiber for light transmission (right) (Ullah and Shin, 2012)

Muhs (2000) and Schelegel *et al*. (2004) respectively described and developed a similar hybrid lighting system design that uses a two-axis tracking parabolic dish concentrator. Direct normal solar radiation gathered by the concentrator is reflected onto a secondary element that divides the solar radiation into visible and infrared spectrums. The secondary element is comprised of eight faceted cold mirrors as seen in Figure 2.9 which allows visible light to be reflected and infra-red light to be transmitted. The visible

light is then reflected and focused into flexible large core polymethylmetacrylate optical fibers that transport the light into locations in the building where it is needed. The visible light is combined with artificial fluorescent lighting or electric lamps in specially designed luminaires to maintain a constant level of room lighting. The transmitted infra-red light is focused on a thermal photovoltaic array that generates electricity with the energy absorbed (Schelegel *et al.*, 2004). The advantages of this hybrid daylighting design are that its components are commercially available and it is a high-efficiency daylight source as it has no infrared component; nevertheless, the manufacturing cost for its commercial production is about USD 3000 for just a 2 m^2 collector that can illuminate only one-storey building.

(a) (b)

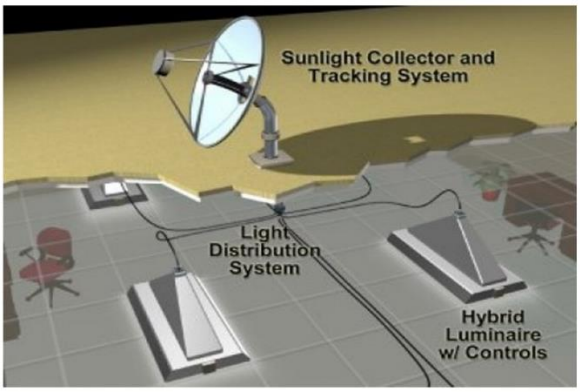

(c)

Figure 2.9: (a.) Prototype of hybrid parabolic dish concentrator (Schelegel *et al*., 2004) (b.) Secondary collector with eight faceted cold mirrors (Schelegel *et al*., 2004) (c.) Major elements of hybrid lighting systems (Muhs, 2000)

A daylighting system, composed of a highly reflective sun-tracking primary parabolic collector (PPC) was theoretically studied by Sapia (2013). A 2.6 m diameter PPC receives solar radiation and reflects it to a 1.03 m diameter secondary collector (SOE). The SOE has a surface that is transparent in the near infra-red range and has a high reflectivity in the visible range. The secondary collector reflects the visible part of the radiation to the heads of the bundles of optical fibers (3 mm diameter and 10 m long). The light travels through a total of 145 fibers until it reaches some tubular diffusing elements from which a 100 m^2 room can be illuminated. The efficiency of the parabolic collector and the secondary collector were calculated as 95 % and 90 % respectively and the overall system efficiency was calculated as 21 %. The total expected cost of the system with a total collective area of 4.48 m^2 is about 6538 euros, which is very high for real life implementation.

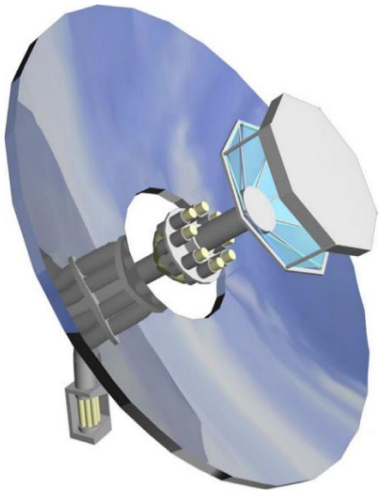

Figure 2.10: Parabolic dish daylighting system: primary parabolic concentrator (sky), bundles of optical fibers (yellow), frequency selective secondary collector (light blue)

Furthermore, a new idea of capturing high-intensity sunlight was demonstrated by Feuermann and Gordon (2002) in which a 0.2 m diameter parabolic dish was used to concentrate sunlight into a single 1 mm diameter fused-silica optical fiber through a flat mirror. Sunlight received by the parabolic dish was reflected to the flat mirror which was supposed to reflect all the sun rays into the optical fiber; rather, a major portion of the light was reflected to the outer surface of the fiber as illustrated in Figure 2.11. In their design, sunlight was collected by many small parabolic dishes which occupied a large area, making roof-top installation of the system almost impossible. Also, the cost of the system became very high as each parabolic dish required a distinct sun-tracking unit and uniform illumination could not be achieved. As a result, the system was used for solar thermal applications to generate energy instead of daylighting as it was initially designed for.

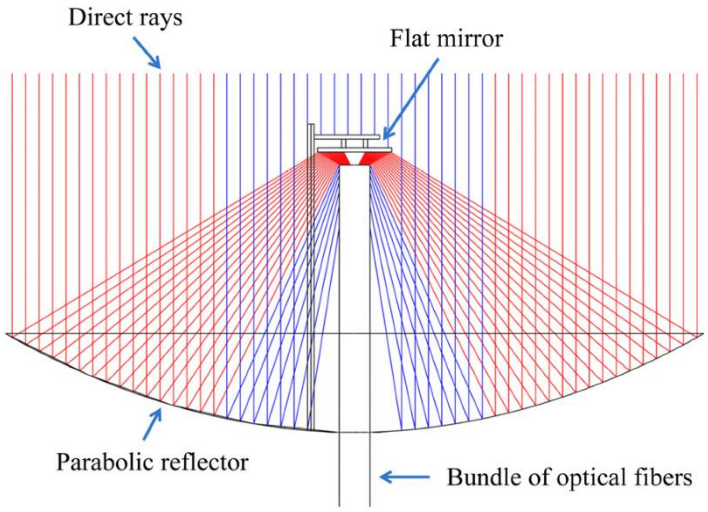

Figure 2.11: Physical layout of the parabolic daylighting system (Feuermann and Gordon, 2002)

Vu and Shin (2016) designed, analyzed and optimized an optical fiber daylighting system using plastic modified compound parabolic concentrators (M-CPC) made by combining two CPC's into one component and a dual-axis sun-tracking system of less than 3˚ angular tolerance. The M-CPC captures, concentrates and collimates direct sunlight to optical fibers for light transmission. To capture maximum level of direct sunlight, the first CPC (200 mm length, 3˚ input angle) called the primary CPC was designed with a high input area and to achieve a high concentration ratio. The secondary CPC (2.47 mm length, 31˚ output angle) was placed contrariwise so that it could be used as a collimator to collimate the light it receives from the primary CPC. The minor aperture sizes of the primary and secondary CPCs were the same to ensure the best coupling between the two CPCs. Plastic optical fiber (POF) of the same diameter as the major aperture of the secondary CPC was coupled to the major aperture of the secondary CPC for light transmission to the interior

of the building. The primary collector is comprised of 10 × 20 M-CPCs array and 200 M-CPCs with 200 pieces of POF to achieve a concentrator size of 540 mm (L) × 270 mm (W) × 212.34 mm (H). Simulation result of the prototype gave an optical efficiency of 85% at the concentration ratio of 100 suns, while their experimental result gave an optical efficiency of 65 %. The prototype gave an illuminance of 4400 lm and can illuminate a surface area of 8 m^2. The advantage of this system is its high tolerance to input angle of sunlight thus making the cost of the system low as there is no need for high-quality optics, alignment, and a very accurate tracking system. Nevertheless, even though Vu and Shin claimed it is a cost-effective design, the manufacturing cost of the M-CPC is still high considering the fact that the output aperture of the secondary CPC has to be fabricated in a special way which involves laser cutting and injection molding methods.

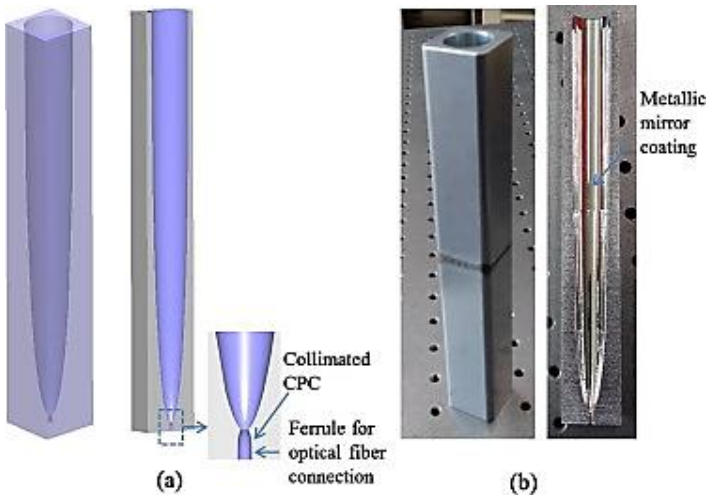

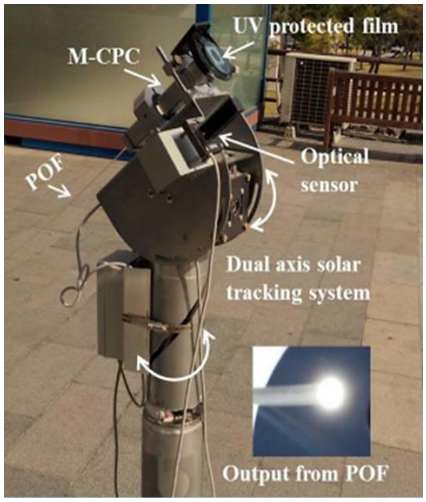

(c)

Figure 2.12: (a) M-CPC structure made in LightTools and its cross-sectional view (b) Fabricated M-CPC and its cross-sectional view (c) Prototype of M-CPC daylighting system (Vu and Shin, 2016)

2.2.5 Double-axis sun tracking – Heliostats

Ullah and Shin (2013b) proposed an economical solar tower daylighting system for delivering sunlight to all floors of a building by collecting sunlight via heliostats (circular plane mirrors), directing the sunlight with a mirror light pipe (MLP), and disseminating the sunlight with light guides. The circular plane mirrors of 0.7 m diameter each were positioned on one side of the mirror light pipe in circular arcs of radii 1.5 m, 2.5 m, 3.5 m and 4.5 m. Each circular plane mirror consisted of a double-axis sun-tracking system to track the sun throughout the daytime and direct sunlight towards a 1 m diameter focusing mirror installed 0.5 m above the mirror light pipe. The focusing mirror made an angle of 10.12^{o} relative to the ground axis and was designed to directly send in light into the MLP which is then transmitted to the

interior of the building on each floor respectively. Thirteen heliostats as illustrated in Figure 2.13 were used to illuminate five floors of 50 m^2 area each. To obtain high illumination in the building interior, the MLP was coated with prismatic optical lighting film and optical film with many layers. The MLP was also constructed in a cylinder-shaped manner to achieve uniform light. Ullah and Shin (2013b) succeeded in achieving the average minimum requirement of more than 500 lx for office illumination. They stated that their proposed daylighting system has been greatly acknowledged for its merits including ease of manageability, cost-effectiveness, the simplicity of its design, the applicability of rapid manufacturing and large scale system production. However, the cost effectiveness and energy-saving benefits of their proposed system are yet to be verified. Also, rooftop installation of this system would be a tedious process as it involves 13 heliostats.

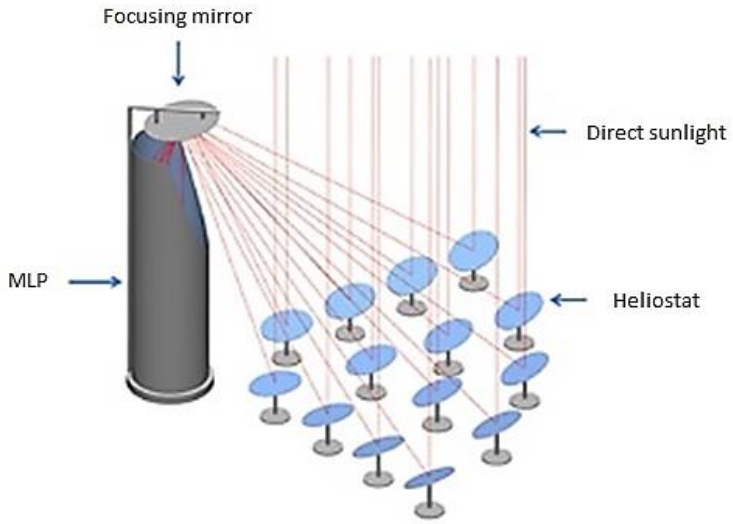

Figure 2.13: Conceptual design of solar tower with heliostat array to provide daylighting in multi-floor buildings via mirror light pipe (Ullah and Shin, 2013b)

2.2.6 Double-axis sun tracking and concentrating system

Song *et al*. (2014) proposed an active daylighting system with a high accuracy dual axis sun-tracking concentrator comprised of five lenses (100 mm in diameter each) to focus sunlight to five 10 m length optical fibers (2 mm in diameter each) for daylight transmission. Parts of the sun-tracking sub-system are labeled and shown in Figure 2.14. The sun-tracking system has a precision of 0.1^{o} to accommodate the concentrating level of the system at 2500 suns. The system had two feedback circles (coarse and fine adjustments) via an angle encoder and a unique array of photodiodes. The coarse adjustment feedback circle is dependent on predictably confirmed data on the suns direction. Various characteristics of the output signals from the photodiode array are used by the control program for fine adjustment. Results of experiments carried out showed that the overall transmission efficiency of the system could be maintained between 37 % and 40 % for a long time. Also, the five optical fibers provided an illuminance of 26.7 lx for a 4.6 m (L) × 4.2 m (W) underpass, 10 m away. Irrespective of the good tracking accuracy of this daylighting system, it has a complicated design as it requires a very high tracking accuracy with a pointing error of less than 0.07˚ to maintain the loss at 14 % or less. More so, the uniformity of light was not explained.

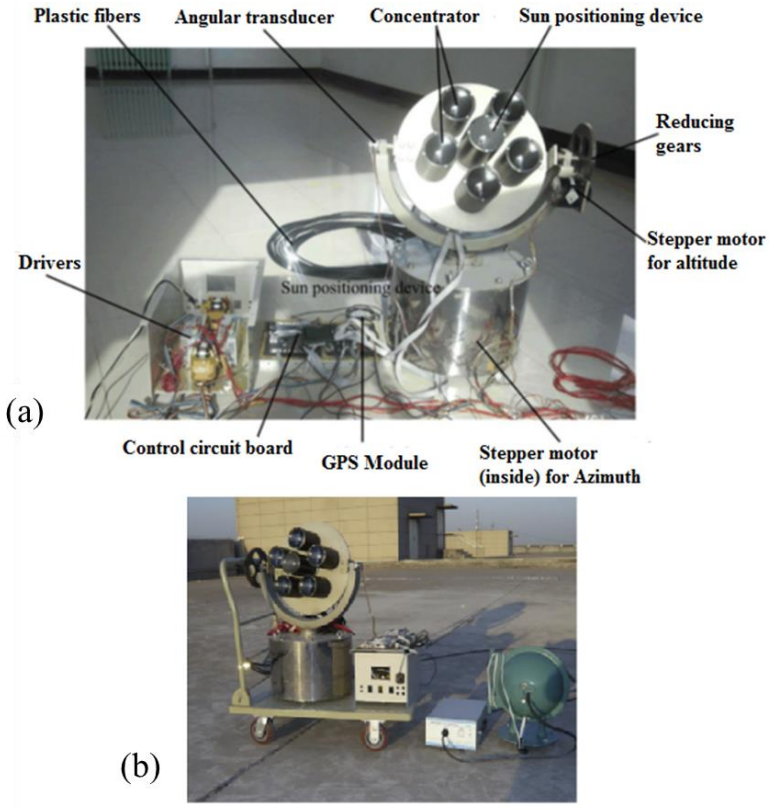

Figure 2.14: (a) Active daylighting system comprised of double axis sun-tracking and concentrating system (b) Working prototype on the roof top (Song *et al*., 2014)

Most of the studies discussed have shown that many existing fiber-optics daylighting systems are complicated in optical design, expensive, produce non-uniform focused sunlight on their receivers and are sometimes affected by pointing error of their sun-tracking system. Hence, a simple and cost-effective daylighting system called "optical fiber-based daylighting system using two-stage reflective non-imaging solar concentrator (NISC) is proposed to curb the existing problems. The proposed system carry the advantages of low and adjustable rim angle for effective collimation of daylight towards the receiver area, high tolerance to pointing error of the sun-

tracking system and focusing sunlight uniformly on the receiver. As stated by Chong *et al*. (2017), non-imaging optics is proposed because:

- The optical design of a non-imaging solar concentrator consists of many segmented facet mirrors that provide the possibility of adjusting the focal distance. When the focal distance is increased, the rim angle is reduced.
- A non-imaging optical device can produce a custom-made focused image to fit the shape and size of various receiver designs for uniform illumination.
- A non-imaging optical device can have a wider acceptance angle resulting in higher tolerances for less precise tracking.
- A non-imaging optical device can give uniform illumination that is highly required in both CPV and daylighting systems.

These advantages first inspired Chong *et al.* (2009) to design a non-imaging planar concentrator (NIPC) comprised of several flat facet mirrors to overlap uniform solar irradiance at a single target area. Due to the gap spacing among the mirrors being limited with respect to the ratio of the focal distance to the concentrator size, sunlight blocking effect among adjacent facet mirrors exist. As the ratio of focal distance to concentrator width decreases, the sunlight blocking effect among adjacent facet mirrors will increase. To solve this problem and still provide uniform illumination on the target area, the non-imaging dish concentrator (NIDC) was proposed and patented by Chong *et al.* (2014). Since NIDC concentrates sunlight by superposing all solar images of its facet mirrors into one image, the incident angles of solar rays are dependent

on the position of the facet mirrors. This can reduce the coupling loss between the solar concentrator and optical fibers even if a pointing error caused by imperfect sun-tracking exists. This previous success in the application of non-imaging focusing technology to CPV systems has led to the conviction that the same can be successfully applied in active daylighting systems. Hence the emergence of the two-stage reflective NISC. This is a new and original idea because it is the first time the non-imaging technology is being developed for daylighting application. Table 2.1 is a summary of all the literatures reviewed.

Table 2.1: Summary of the literature review on existing fiber-optics active daylighting systems

Authors	**Paper title**	**Active daylighting method/system**	**Findings and discussion**
Single-axis sun-tracking system			
Ullah and Shin (2014)	Highly concentrated optical fiber-based daylighting systems for multi-floor office buildings	Parabolic trough daylighting system	• Three-stage reflective linear focusing design comprising a parabolic trough, parabolic reflector and trough CPC. • SOFs coupled with POFs are used for light transmission. • **Advantage**: This system can be made on a large scale with only one tracking module. • **Disadvantage**: It has a complicated optical design and a high manufacturing cost (only the parabolic trough costs USD 400/m^2 and the automatic tracking module costs USD 400, making it a total of > USD 800/m^2).
		Linear Fresnel Lens daylighting system	• Three-stage refractive linear focusing design comprising a linear Fresnel lens, collimating plano-concave lens and trough CPC • SOFs coupled with POFs are used for light transmission. • **Advantage**: This system can be made on a large scale with only one tracking module. • **Disadvantage**: It has a complicated optical design and a high manufacturing cost (only the linear Fresnel lens cost USD 200/m^2 and the automatic tracking module costs USD 400, making it a total of > USD 600/m^2).
Double axis sun-tracking system			

Ullah and Shin (2012, 2013a)	Development of optical fiber-based daylighting system with uniform illumination (2012). Uniformly illuminated efficient daylighting system (2013a)	Fresnel lens daylighting system	• Two stages of focusing: Fresnel lens and plano-concave lens. • SOFs coupled with POFs are used for light transmission • **Advantage**: Simulation and experimental result showed uniform illumination in the optical fiber bundles. • The prototype produced an average illuminance of 675 lux. • **Disadvantage**: High concentration ratio cannot be achieved as the linear Fresnel reflector normally concentrates < 100 suns.
Muhs (2000)	Design and analysis of hybrid solar lighting full-spectrum solar energy systems	Fresnel lens daylighting system	• Hybrid CPV and daylighting system • POF was used for light transmission • As a hybrid system, electricity produced can be used for indoor illumination when there is no sunlight.
Shen *et al*.(2009)	Analysis of a hybrid cost-effective solar lighting system.		
Gilmore (1988)	Sun flower over Tokyo	Himawari solar lighting system using Fresnel lens	• Quartz glass optical fiber is used for light transmission • **Disadvantages**: High system manufacturing cost; the uniformity of sunlight at both the capturing and distribution stages were not well defined. • **Advantage**: Himawari sunlight contains only a small amount of infrared radiation and thus would not affect the temperature of the room.
Vu *et al*., (2016)	Cost-effective optical fiber daylighting system using modified compound parabolic concentrators	Modified optical fiber daylighting system (M-OFDS) using Fresnel lens	• M-OFDS consists of three parts: - primary concentrator (linear Fresnel lens and truncated cone shaped plastic optical fiber) - collimator (parabolic mirror and convex lens) - light guide • Sunlight is transported in open space to the room. • 85 % uniformity of light was obtained from numerical analysis • Each M-OFDS provided about 5000 lm with an optical efficiency of 50.7 %. • **Disadvantages**: Complicated optical design with many stages of optical devices; too expensive for real life implementation; the system cannot perform where an obstacle such as trees exist.
Ullah and Shin (2012, 2013a)	Development of optical fiber-based daylighting system with uniform illumination (2012).	Parabolic dish/mirror daylighting system	• Two stages of focusing: Primary concave parabolic mirror and secondary convex parabolic mirror. • SOFs coupled with POFs are used for light transmission • Experimental results indicated that uniform illumination was obtained in the bundle of optical fibers. • Average illuminance of 705 lux was attained in the building.

	Uniformly illuminated efficient daylighting system (2013a)		• **Disadvantage:** The total coat of the system was not provided.
Muhs (2000)	Design and analysis of hybrid solar lighting full-spectrum solar energy systems	Parabolic dish concentrator daylighting system	• Consists of a parabolic dish concentrator, a secondary collector (eight faceted cold mirrors) and POFs for light transmission. • **Advantages**: It is a high-efficiency daylight source as it has no infrared component and its components are commercially available. • **Disadvantages**: High manufacturing cost of about USD 3000 for a 2 m^2 collector that can illuminate only one-storey building.
Schelegel *et al*. (2004)	Analysis of a full spectrum hybrid lighting system		
Sapia (2013)	Daylighting in buildings: Developments of sunlight addressing by optical fiber	Parabolic concentrator daylighting system	• Theoretical study only • Consists of a primary parabolic dish concentrator, a secondary collector (eight faceted cold mirrors) and POFs for light transmission. • Efficiency of the primary parabolic collector was calculated as 95 %. • Efficiency of the secondary collector was calculated as 90 %. • Overall system efficiency was calculated as 21 %. • **Disadvantage**: The total expected cost of the system with a total collective area of 4.48 m^2 is about 6538 euros which is very high for real life implementation.
Feuermann and Gordon (2002)	Solar fiber-optic mini-dish concentrator. First experimental results and field experience	Parabolic dish concentrator daylighting system	• Consists of a 0.2 m parabolic dish, flat mirror and a single fused-silica optical fiber • **Disadvantages**: Sunlight was collected by many small parabolic dishes which occupied a large area and made roof-top installation of the system difficult; high system manufacturing cost as each parabolic dish required a distinct sun-tracking unit; uniform illumination could not be achieved. • Due to the above mentioned disadvantages, the system was used for solar thermal applications instead of daylighting application.
Vu and Shin (2016)	Cost-effective optical fiber daylighting system using modified compound parabolic concentrators	Modified compound parabolic concentrator (M-CPC) daylighting system	• The M-CPC consists of two CPCs (one as a concentrator, one as a collimator) combined into one component and POFs for light transmission. • The primary collector is comprised of 200 M-CPCs with 200 pieces of POF to achieve a concentrator size of 540 mm × 270 mm × 212.34 mm. • Optical efficiency of the system is 85 % based on the simulation result of the prototype and 65 % based on experimental result. • Illuminance of prototype is 4400 lm for 8 m^2 room. • **Advantage**: The system has a high tolerance to input angle of sunlight which makes the system cost effective

			as there is no need for a very accurate tracking system. • **Disadvantage**: High manufacturing cost as the CPCs have to be fabricated in a special way.
Ullah and Shin (2013b)	Concept of solar tower for daylighting in multi-floor buildings	Solar tower daylighting system using heliostats	• Consists of thirteen heliostats (circular plane mirrors) to direct sunlight to a mirror light pipe. • Five floors of 50 m^2 area each were illuminated with this system • Advantages: ease of manageability, cost-effectiveness, simple design, applicability of rapid manufacturing and large scale system production • Disadvantage: Root-top installation would be a tedious process as it involves many heliostats. • Cost-effectiveness and energy savings of the system are yet to be verified.
Song *et al*, (2014)	Daylighting system via fibers based on two-stage sun-tracking model	Optical lens (K9) concentrator daylighting system	• Comprises five optical lenses to focus sunlight to five 10 m length optical fibers. • The system has a precision of 0.1˚ to accommodate the concentrating level of the system at 2500 suns. • Transmission efficiency could be maintained between 37 % and 40 % for a long time. • Five optical fibers gave an illuminance of 26.7 lux for a 4.6 m (W) × 4.2 m (H) underpass, 10 m away • **Advantage**: Good tracking accuracy • **Disadvantage**: Complicated design as it requires a very high tracking accuracy with a pointing error of < 0.07˚ to maintain the loss at 14 % or less.

CHAPTER 3

METHODOLOGY

The flow chart in Figure 3.1 presents an outline of the methods used in this study in three phases: phase 1 (Parts A and B), phase 2 and phase 3. Part A covers the design of the two-stage reflective NISC and part B covers the hardware construction of the two-stage reflective NISC. Phase 2 covers the design and construction of the optical fibers for guiding the concentrated sunlight into the building. Phase 3 covers the system performance study and feasibility studies of the two-stage reflective NISC.

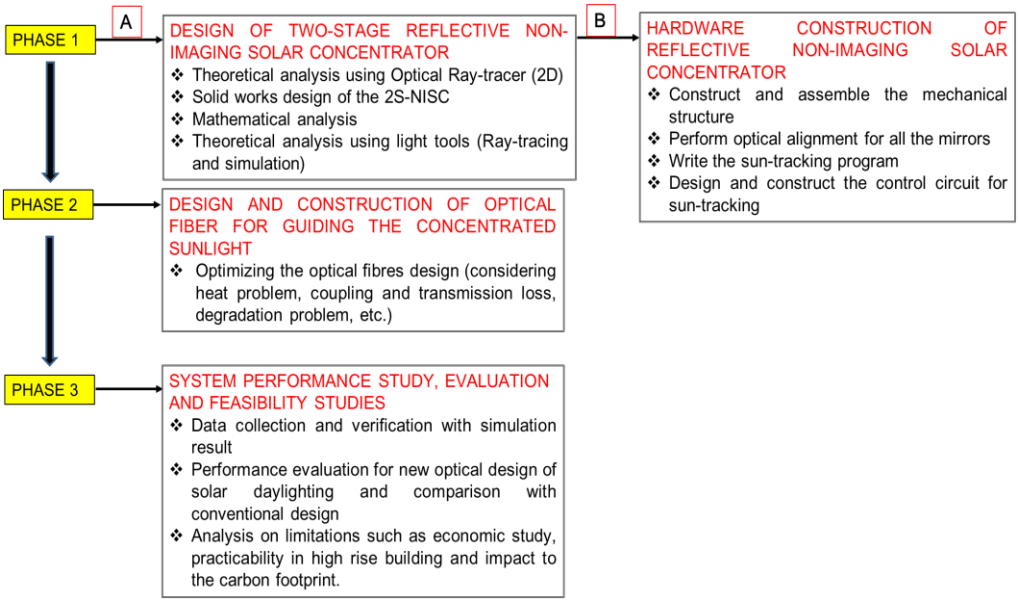

Figure 3.1: Flow chart of the research methodology for the two-stage reflective NISC daylighting system

3.1 Background theory of the two-stage reflective non-imaging solar concentrator (NISC)

The proposed two-stage reflective non-imaging solar concentrator was designed based on the concept of the Cassegrain reflector that is widely deployed in reflecting telescopes. The Cassegrain reflector is a two-stage reflector with a combination of a primary concave mirror and a secondary convex mirror (Ma *et al*., 2014). The incident ray is reflected by the primary concave mirror to the secondary convex mirror. The secondary convex mirror then reflects and focuses the rays on the target. Concave and convex mirrors have been found to be quite expensive in the application of solar energy. Therefore, many flat facet mirrors are proposed as primary and secondary reflectors instead of curved mirrors while the target is a bundle of plastic optical fibers (POF).

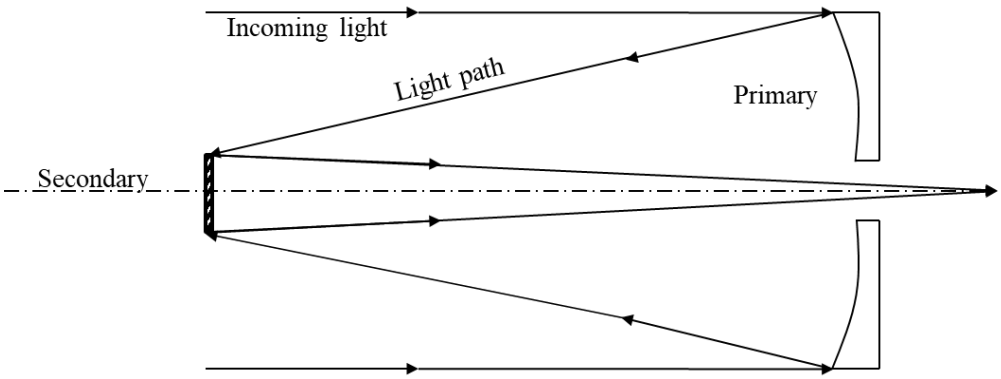

Figure 3.2: Optical arrangement of the Cassegrain reflector (ASGH Mirror Workshop, 2012)

To verify the optical design of the two-stage reflection of the non-imaging solar concentrator, 2-D ray tracing was performed using a Java-based 2-D ray tracing software called Optical Ray-tracer. 2-D ray-tracing analysis enables quick understanding of how the incident sunrays can be focused by the primary reflector to the secondary reflector and subsequently to the optical fibers. The dimension of each flat facet mirror in the primary reflector was set as 5 cm × 5 cm × 0.2 cm (thickness), while the dimension of each flat facet mirror in the secondary reflector was unknown. This 2-D ray-tracing analysis helped in determining the required dimension of each flat facet mirror in the secondary reflector (Obianuju and Chong, 2017).

Each mirror assembly set in the primary reflector consists of four flat facet mirrors arranged in a group with a gap spacing of 0.5 cm between two adjacent facet mirrors. The facet mirrors in each mirror assembly set are tilted to reflect the sunrays to their respective secondary facet mirror where the perpendicular distance between primary and secondary reflectors is 70 cm. The secondary facet mirror is tilted to reflect the sunrays towards the optical fibers at the target. Since Optical Ray Tracer software performs ray-tracing in 2-D only, two facet mirrors in each assembly set for both left and right sides are simulated as shown in Figure 3.3. From the simulation result, the estimated size of each secondary facet mirror to embrace all the reflected rays from the primary mirror assembly set was found as 8 cm × 8 cm × 0.2 cm (thickness).

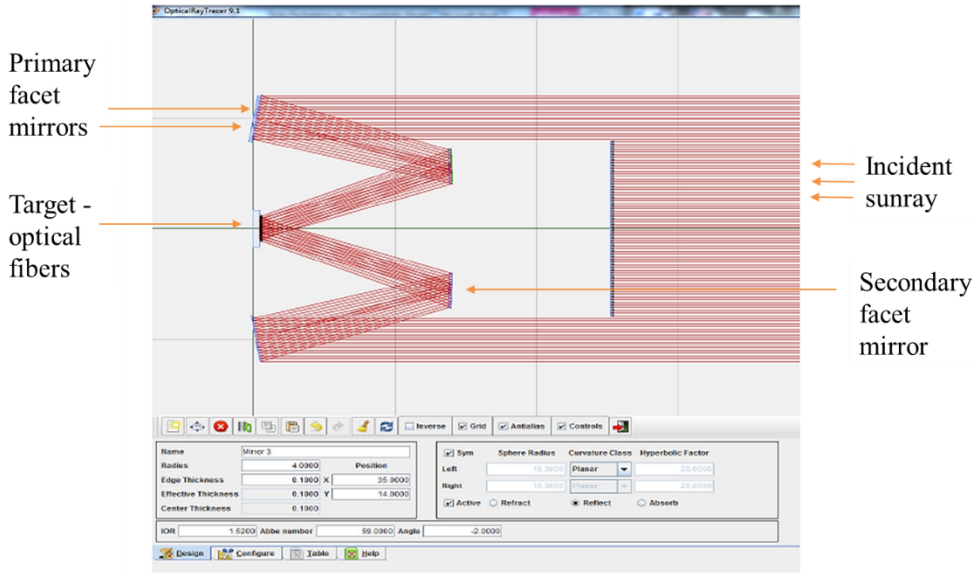

Figure 3.3: 2-D ray-tracing analysis to determine the size of each secondary facet mirror based on the Cassegrain reflector design

3.2 3D design of the two-stage reflective NISC using SolidWorks.

Based on the background theory, the design of the two-stage reflective NISC was modeled in 3-D as shown in Figure 3.4 with a 3-D CAD software called SolidWorks. The design of the two-stage reflective NISC comprises a primary and secondary reflector. The primary reflector consists of twenty mirror assembly sets with four flat facet mirrors per mirror assembly set. The primary flat facet mirrors within each mirror assembly set were drawn 0.5 cm apart while two mirror assembly sets were drawn 2 cm apart from each other. The secondary reflector consists of twenty secondary flat facet mirrors drawn 0.8 cm adjacent to each other. Each facet mirror assembly is made up of six components as illustrated in Figure 3.4 (a): (1) flat mirror, (2) three bolts (M4 × 60 mm), (3) PVC plate acting as the mirror frame, (4) washers, (5) compression spring and (6) nuts. The dimension of the target area located at

the center of the primary reflector was set as 5 cm × 5 cm which is equivalent to the size of one primary mirror.

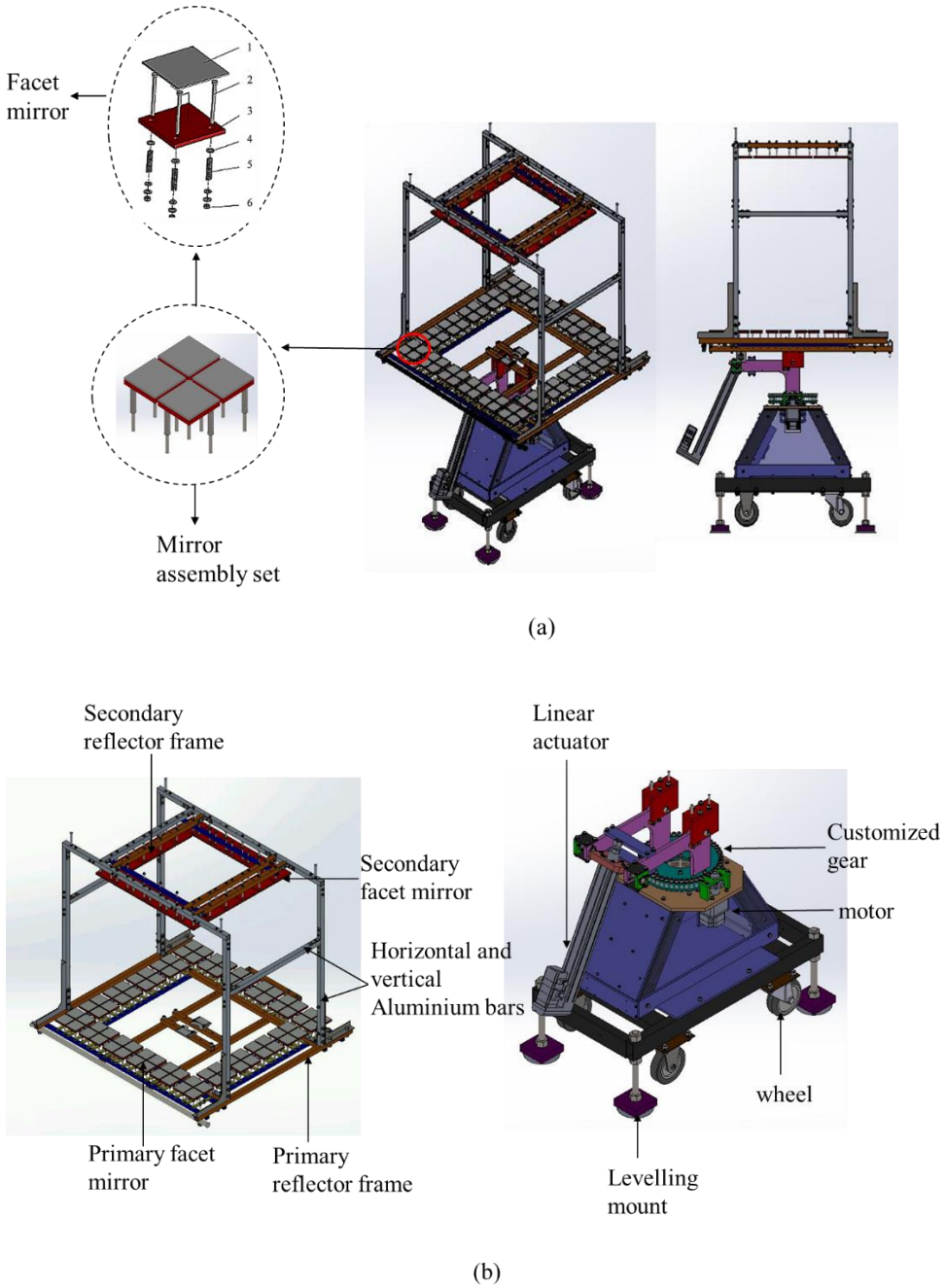

Figure 3.4: (a) 3-D drawing of the two-stage reflective NISC in isometric view and side view (b) Labelled 3-D drawing of the two parts of the two-stage reflective NISC

A schematic diagram to illustrate the operating principle of the proposed daylighting system from the sunlight receiving stage to the indoor illumination stage is shown in Figure 3.5 below. The control system tracks the sun so that the first stage primary reflector receives incident sunlight and reflects it to the second stage secondary reflector which then reflects the light to the target/receiver area. At the target area, a hot-mirror filter filters out ultra-violet and infra-red rays and permits visible light to pass through to the plastic optical fibers which transmit the light to distributing lens fixed inside the room for indoor illumination.

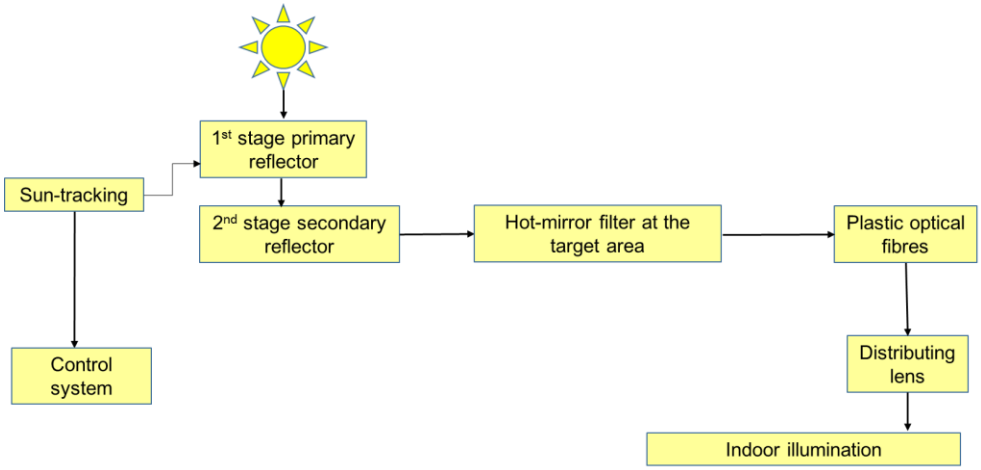

Figure 3.5: A schematic diagram to show the operating principle of the proposed daylighting system

The design specification of the two-stage reflective NISC is listed in Table 3.1.

Table 3.1: Design specification of the two-stage reflective non-imaging solar concentrator (NISC)

Parameter	Specifications
Number of mirror assembly set in the primary reflector	20
Number of primary facet mirrors in each mirror assembly set	4
Number of secondary facet mirrors in the secondary reflector	20
Primary facet mirror dimension	5 cm (L) × 5 cm (W) × 0.2 cm (T)
Secondary facet mirror dimension	8 cm (L) × 8 cm (W) × 0.2 cm (T)
Mirror assembly set dimension	10.5 cm (L) × 10.5 cm (W)
Gap between primary facet mirrors in the mirror assembly set	0.5 cm
Gap between two adjacent mirror assembly sets	2 cm
Gap between two adjacent secondary facet mirrors	0.8 cm
Target area at the center of the primary reflector	5 cm (L) × 5 cm (W)
Primary reflector frame dimension	73 cm (L) × 73 cm (W)
Secondary reflector frame dimension	52 cm (L) × 52 cm (W)
Reflective area of the primary reflector	0.2 m^2
Reflective area of the secondary reflector	0.13 m^2
Perpendicular distance between the primary and secondary reflectors (L)	70 cm
Half rim angle of the two-stage reflective NISC	24º
Total height of the two-stage reflective NISC	153 cm

In the two-stage reflective NISC design, one set of primary mirrors will reflect its incident sunlight to its respective secondary mirror. As illustrated in Figure 3.6, all the primary mirror assembly sets and their counterpart secondary facet mirrors are labeled with same numbers to show that each specific mirror assembly set will superpose all their solar rays to the target located at the center of the primary reflector via its corresponding secondary facet mirror.

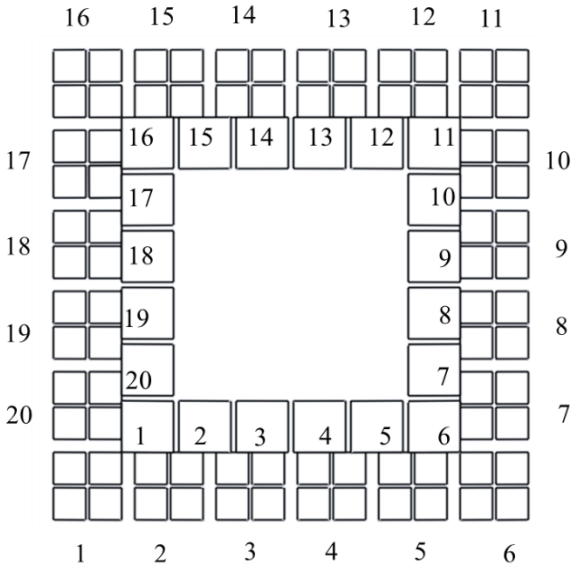

Figure 3.6: Top view of primary and secondary facet mirror arrangements showing all mirror assembly sets and their counterpart secondary facet mirrors numerically labeled respectively

3.3 Mathematical formulas for calculating the tilting angles of the primary and secondary mirrors

After the 3D-design was completed, mathematical analysis using trigonometry was carried out to find the reflective points of the primary and secondary facet mirrors and their respective tilting angles to superpose the incident solar rays to the target area. Since all the facet mirrors are flat mirrors, each facet mirror is tilted in two orientation angles (along the *x* and *y*-axis) for optimum reflection of the received sunlight onto the target area. The respective tilting angles are: γ & σ for each primary facet mirror and ρ & ϕ for each secondary facet mirror. σ is the tilted angle of the primary facet mirror along the *x*-axis and γ is the tilted angle of the primary facet mirror along the *y*-axis. ϕ is the tilted angle of the secondary facet mirror along the *x*-axis and ρ is the tilted angle of the secondary facet mirror along the *y*-axis. For a geometric representation, the Cartesian coordinate system is used to identify the position of all the facet mirrors within the two-stage reflective NISC with the origin **O** (0, 0, 0) located at the center of the primary reflector as illustrated in Figure 3.7. In the Cartesian coordinate system, the **X**-axis lies along the column of the mirrors, the **Y**-axis lies along the row of the mirrors, and the **Z**-axis points towards the center of the secondary reflector.

Point **A** (x_1, y_1, z_1) is defined as the central point of the primary mirror assembly set. Point **B** (x_2, y_2, z_2) is defined as the central point of the secondary facet mirror corresponding to the aforementioned mirror assembly set. From both points **A** and **B**, point **C**(x_3, y_3, z_3) is defined in the coordinate system

based on two criteria: (1) the points **A**, **B**, and **C** are collinear; (2) the distance of **ABC** must be equal to the distance of **ABO**.

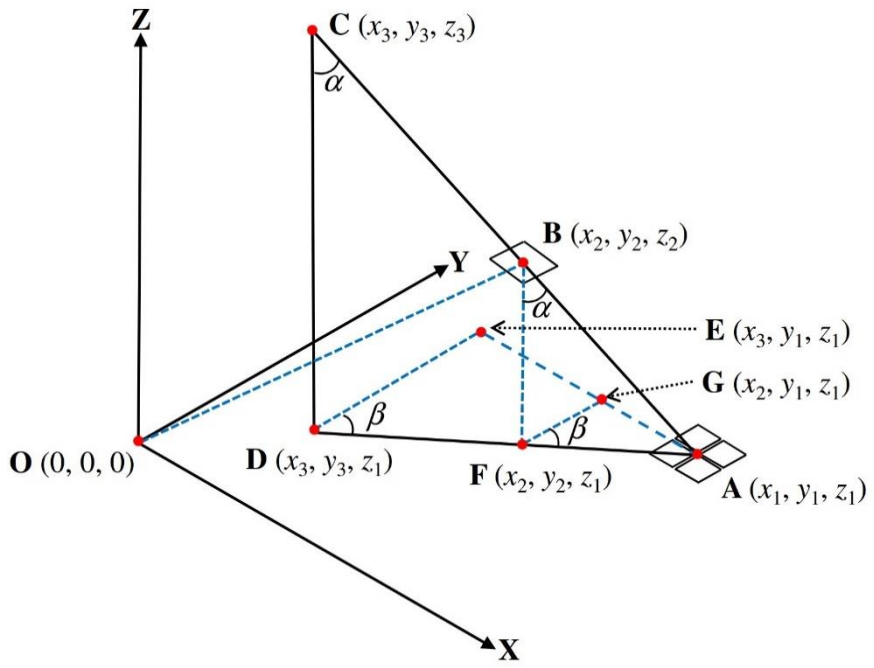

Figure 3.7: Cartesian coordinate system defined in the plane of the primary reflector with its origin **O** defined at the center of the primary reflector

Coordinate **A** (x_1, y_1, z_1) and coordinate **B** (x_2, y_2, z_2) are known; thus, coordinate **C** (x_3, y_3, z_3) was determined as the following based on Figure 3.7:

To compute z_3,

$$\cos\alpha = \frac{L_{FB}}{L_{AB}} = \frac{L_{DC}}{L_{AC}} \Rightarrow L_{DC} = \frac{L_{AC}L_{FB}}{L_{AB}} = z_3 - z_1 \Rightarrow z_3 = \frac{L_{AC}L_{FB}}{L_{AB}} + z_1$$

$$\therefore z_3 = z_2 + \frac{(z_2 - z_1)\left(\sqrt{x_2^2 + y_2^2 + z_2^2}\right)}{\sqrt{(x_2 - x_1)^2 + (y_2 - y_1)^2 + (z_2 - z_1)^2}} \qquad (3.1)$$

To compute y_3,

$$\cos\beta = \frac{L_{GF}}{L_{AF}} = \frac{L_{ED}}{L_{AD}} \Rightarrow L_{ED} = \frac{L_{AD}L_{GF}}{L_{AF}} = y_3 - y_1 \Rightarrow y_3 = \frac{L_{AD}L_{GF}}{L_{AF}} + y_1$$

$$\therefore y_3 = \frac{(z_3 - z_1)(y_2 - y_1)}{(z_2 - z_1)} + y_1 \tag{3.2}$$

To compute x_3,

$$\tan\beta = \frac{L_{AG}}{L_{GF}} = \frac{L_{AE}}{L_{ED}} \Rightarrow L_{AE} = \frac{L_{AG}L_{ED}}{L_{GF}} = x_3 - x_1 \Rightarrow x_3 = \frac{L_{AG}L_{ED}}{L_{GF}} + x_1$$

$$\therefore x_3 = \frac{(y_3 - y_1)(x_2 - x_1)}{(y_2 - y_1)} + x_1 \tag{3.3}$$

Where $\alpha = \angle ACD = \angle ABF$ and $\beta = \angle ADE = \angle AFG$

After determining the coordinate **C**, the tilted angles for the primary and the secondary facet mirrors were calculated. From Figure 3.8, vectors and parameters for the primary facet mirror with its central point at coordinate **M** (*x*, *y*, *z*) are defined as follows: $\hat{I}$ (0, 0, 1) is the unit vector of the incident sunray; $\hat{N}$ is the unit vector normal to the primary facet mirror; $\hat{R}$ is the unit vector of the reflected sunray from point **M** to the point **C**; θ_1 is the incident angle of the sunray relative to the primary facet mirror.

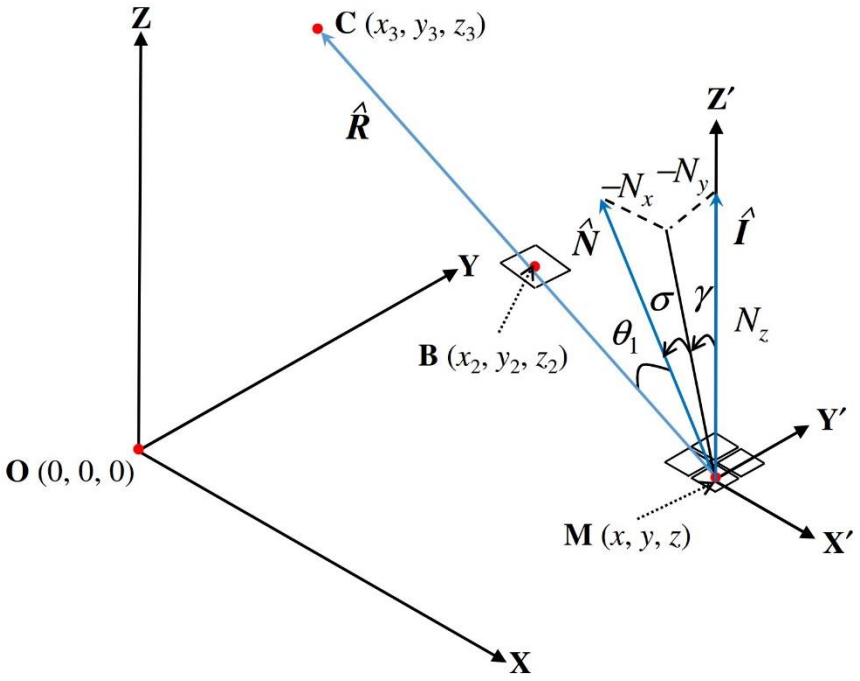

Figure 3.8: Cartesian coordinate system showing the coordinate **M**, incident angle θ_1, the two tilted angles γ and σ for the primary facet mirror, where **O** is the origin of the coordinate system, the target point and also the center of the primary reflector

The formulas for calculating the two tilted angles of each primary facet mirror is as follows:

$$\gamma = \tan^{-1}\left(\frac{-N_y}{N_z}\right) \tag{3.4}$$

$$\sigma = \sin^{-1}\left(-N_x\right) \tag{3.5}$$

From Snell-Descartes law, the unit vector normal to the primary facet mirror, $\hat{N}$ (Hetcht, 2002; Chong *et al*., 2009) is obtained as:

$$\hat{N} = \frac{\hat{I} + \hat{R}}{\sqrt{2(1 + \hat{I} \cdot \hat{R})}} \tag{3.6}$$

Provided that $\hat{I} = \hat{k}$ (3.7)

and $\hat{R} = \dfrac{(x_3 - x)\hat{i} + (y_3 - y)\hat{j} + (z_3 - z)\hat{k}}{\sqrt{(x_3 - x)^2 + (y_3 - y)^2 + (z_3 - z)^2}}$ (3.8)

From Figure 3.9, vectors and parameters for the secondary facet mirror with its central point at coordinate **B** (x_2, y_2, z_2) are defined as follows: $\hat{I}'$ is the unit vector of the incident ray on the secondary facet mirror from point **A**; $\hat{N}'$ is the unit vector normal to the secondary facet mirror; $\hat{R}'$ is the unit vector of the reflected ray from the secondary facet mirror at point **B** to the target at point **O**; θ_2 is the incident angle of the incident sunray relative to the secondary facet mirror and **O** is the origin of the coordinate system and the target point, which is also the center of the primary reflector.

The two tilted angles of each secondary facet mirror can be calculated using the formulas:

$$\rho = \tan^{-1}\left(\frac{N'_y}{N'_z}\right) \tag{3.9}$$

$$\phi = \sin^{-1}(-N'_x) \tag{3.10}$$

Similar to Equation (3.6), the following formulas can be derived from Snell-Descartes law (Hetcht, 2002; Chong *et al*., 2009):

$$\hat{N}' = \frac{\hat{I}' + \hat{R}'}{\sqrt{2(1 + \hat{I}' \cdot \hat{R}')}} \tag{3.11}$$

Given that $\hat{I}' = \dfrac{(x_1 - x_2)\hat{i} + (y_1 - y_2)\hat{j} + (z_1 - z_2)\hat{k}}{\sqrt{(x_1 - x_2)^2 + (y_1 - y_2)^2 + (z_1 - z_2)^2}}$ (3.12)

and $\hat{R}' = \dfrac{-x_2\hat{i} - y_2\hat{j} - z_2\hat{k}}{\sqrt{x_2^{\,2} + y_2^{\,2} + z_2^{\,2}}}$ (3.13)

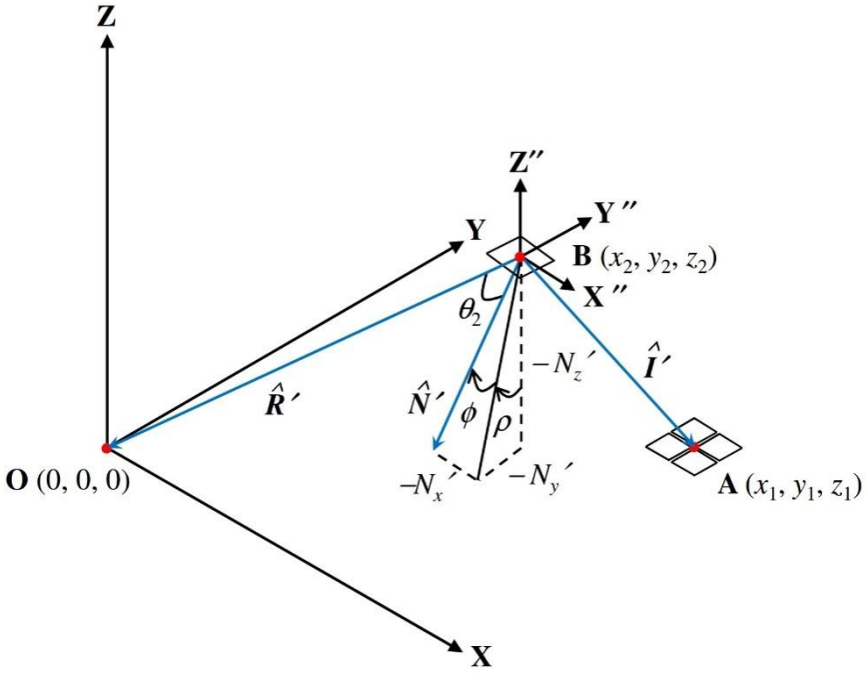

Figure 3.9: Cartesian coordinate system representing the incident angle θ_2, the two tilted angles ρ and ϕ for the secondary facet mirror

Using the derived formulas, the tilting angles were calculated for one quadrant of the reflector consisting of five primary mirror assembly sets and five secondary mirrors. The tilting angles are the same for the other quadrants with different tilting orientations (either positive or negative) based on the mirror location. Figure 3.10 illustrates the quadrant labeled from set one to five corresponding to the set numbers in Table 3.2 and Table 3.3.

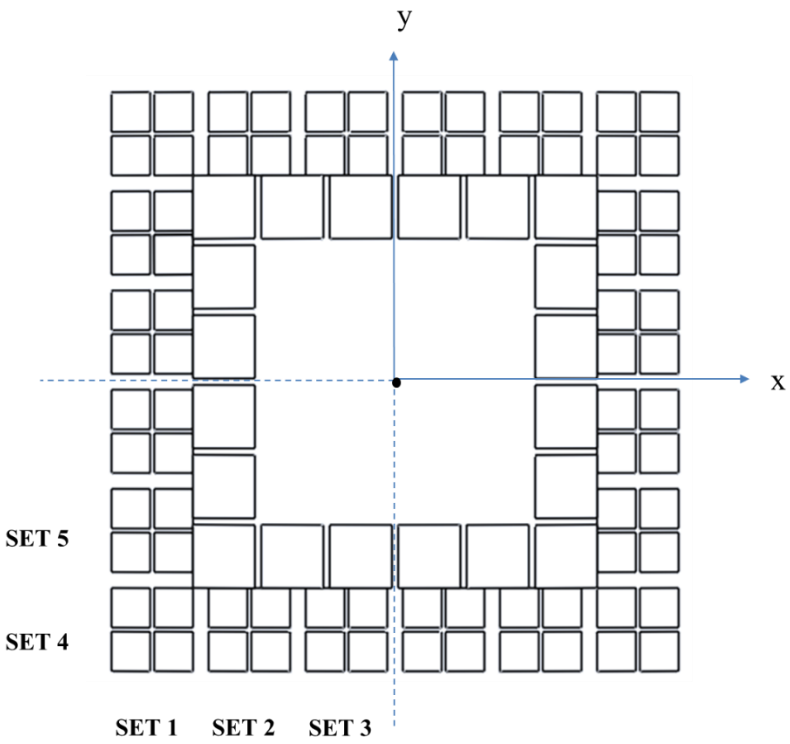

Figure 3.10: Primary and secondary mirror arrangement showing set one to five with respect to Table 3.2

To verify that the calculated tilting angles are correct, the primary and secondary reflectors alone were drawn in SolidWorks software; where the new target coordinates (Point **C** – referring to Figure 3.8) were derived. Figure 3.11 illustrates this. The new target coordinates in Table 3.2 were derived from SolidWorks; which corresponded to the target coordinates derived by calculation.

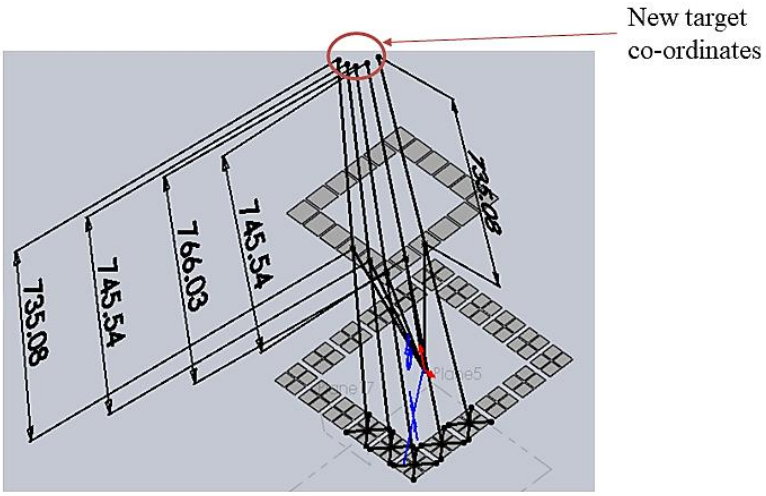

Figure 3.11: SolidWorks drawing of the primary and secondary reflectors showing the new target coordinates for one quadrant

Table 3.2: Table showing the coordinates of one quadrant of the primary and secondary mirrors and their new target coordinates

	Primary coordinates (cm)			Centre point of each set (cm)			Secondary coordinates (cm)			New target coordinates (cm)		
	x	y	z	x	y	z	x	y	z	x	y	z
SET 1	-34.00	-28.50	0.00	-31.25	-31.25	0.20	-22.00	-22.00	70.20	-12.03	-12.03	145.68
	-28.50	-28.50	0.00									
	-34.00	-34.00	0.00									
	-28.50	-34.00	0.00									
SET 2	-21.50	-28.50	0.00	-18.75	-31.25	0.20	-13.20	-22.00	70.20	-7.34	-12.24	144.07
	-16.00	-28.50	0.00									
	-21.50	-34.00	0.00									
	-16.00	-34.00	0.00									
SET 3	-9.00	-28.50	0.00	-6.25	-31.25	0.20	-4.40	-22.00	70.20	-2.47	-12.35	143.24
	-3.50	-28.50	0.00									
	-9.00	-34.00	0.00									
	-3.50	-34.00	0.00									
SET 4	-28.50	-16.00	0.00	-31.25	-18.75	0.20	-22.00	-13.20	70.20	-12.24	-7.34	144.07
	-28.50	-21.50	0.00									
	-34.00	-16.00	0.00									
	-34.00	-21.50	0.00									
SET 5	-28.50	-3.50	0.00	-31.25	-6.25	0.20	-22.00	-4.40	70.20	-12.35	-2.47	143.24
	-28.50	-9.00	0.00									
	-34.00	-3.50	0.00									
	-34.00	-9.00	0.00									

'Primary coordinates' in Table 3.2 above refers to the coordinates of each primary mirror in the first quadrant shown in Figure 3.10. 'Center point of each set' refers to the coordinates of the center point of one assembly set; 'secondary co-ordinates' refers to the coordinates of each secondary mirror in

the first quadrant and ‘new target coordinates’ refers to the coordinates of the new target point for the five sets of mirrors.

Table 3.3: Table showing tilting angle calculation values for the primary and secondary mirrors

SET	**Primary mirror tilting angles**		**Secondary mirror tilting angles**	
	X-axis (σ°)	**Y-axis (γ°)**	**X-axis (ϕ°)**	**Y-axis (ρ°)**
SET 1	-3.21	-4.27	4.72	-4.70
	-3.21	-3.21		
	-4.26	-4.25		
	-4.27	-3.20		
SET 2	-3.21	-2.79	4.85	-2.91
	-3.22	-1.71		
	-4.28	-2.78		
	-4.29	-1.71		
SET 3	-3.21	-1.30	4.93	-0.98
	-3.22	-0.20		
	-4.29	-1.29		
	-4.30	-0.20		
SET 4	-1.73	-3.24	2.92	-4.85
	-2.82	-3.23		
	-1.72	-4.32		
	-2.81	-4.31		
SET 5	-0.21	-3.22	0.99	-4.93
	-1.30	-3.21		
	-0.20	-4.30		
	-1.30	-4.29		

In Table 3.3, the second and third columns show the tilting angles (σ and γ) of the primary mirrors in the first quadrant; and ϕ and ρ in the last two columns are the tilting angles of the secondary mirrors in the first quadrant.

3.4 Theoretical analysis on the reflectors, using LightTools software

After calculating the tilting angles, the primary flat facet mirrors and secondary flat facet mirrors were tilted according to the angles in Table 3.3 and then imported into an optical simulation tool called LightTools software for 3-D ray-tracing and analysis. 3-D ray tracing, solar flux distribution and

spillage loss analysis on the receiver were performed from which the concentration ratio, optimum receiver size and the illumination capability of the two-stage reflective NISC were found.

Figure 3.12 shows the tilted mirrors, where *L* is the distance between the primary reflector and the secondary reflector which is 70 cm. The ray-tracing process covered the entire primary reflector of the two-stage reflective NISC in the simulation. Figure 3.13 illustrates the schematic diagram of the two-stage NISC to show how the sunrays are focused onto the input aperture of optical fibers in 3-D view. Results showed that all the incident rays were focused on the target area, implying that the tilting angles were calculated correctly. About 20 million rays were traced in other to achieve a reasonably good resolution in the solar flux distribution plot. The solar flux distribution analysis was done for the entire target area of 50 cm × 50 cm.

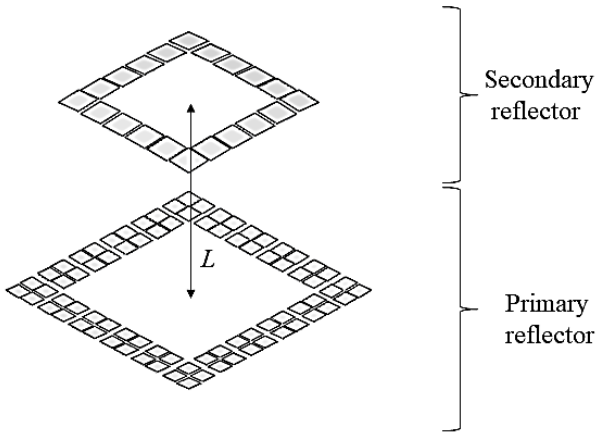

Figure 3.12: 3-D view of the tilted primary and secondary mirrors of the two-stage reflective NISC

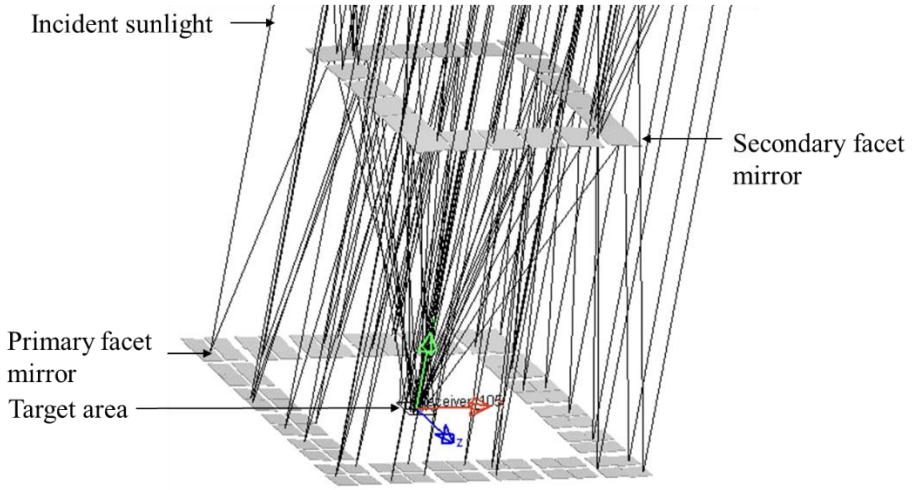

Figure 3.13: 3-D view of the two-stage reflective NISC showing how the sunrays are focused on the target area

It was assumed that all the facet mirrors have 100% reflectance and the solar irradiance of incident sunlight on the primary facet mirror is 1000 W/m^2 (equivalent to 1 sun). Also, to imitate sunrays with the solar disc half angle of 4.65 mrad, a light source with a dimension somewhat bigger than the dimension of the two-stage reflective NISC prototype is generated. The central region of the secondary reflector is an open empty area; hence there are direct incident sunrays on the receiver plus reflected sun rays from the reflectors. The result obtained from this simulation will be compared with the experimental results in another section.

From the outcome of the simulated solar flux distribution, the uniformly illuminated region of the receiver covers an area of 38 mm × 38 mm with an average solar concentration ratio (C_{avg}) of 76 suns. The uniformly illuminated region refers to the area in the central region of the solar flux distribution at the receiver, where solar concentration ratio is nearly constant as the entire solar

images of the flat facet mirrors are perfectly overlapped. The average solar concentration ratio contributed by the reflector is 75 suns, and the average solar concentration ratio contributed by direct sunlight without going through any reflection is 1 sun. It is observed that the average solar concentration ratio of the target area is less than 80 suns which is the number of the primary facet mirrors. This is because the solar flux distribution contributed by the reflector is unavoidably spread to a larger area primarily due to both the cosine loss and solar disc effect (Chong *et al*., 2009). Cosine effect is a phenomenon where the effective receiving area of the two-stage reflective NISC reduces based on the cosine of the incidence angle. This happens when a mirror or set of mirrors are reflecting off-axis which directly reduces the concentration ratio (number of suns) at the receiver area of the concentrator. The generated loss is called cosine loss. Cosine loss varies as a function of the position of the sun and it occurs because mirrors cannot be constantly aligned normal to the incident solar rays. Solar disc effect occurs when there is solar radiation within a few degrees of the solar disc caused by atmospheric scattering. Therefore, the rays of sun that strike the mirror surface are considered as cone rays.

Viewing from the top, the uniformly illuminated region is an even area with steeply decreasing edges to form a total focused image size of 65 mm × 65 mm. Figure 3.14 (a) illustrates the simulated result of the focused image formed at the receiver area without pointing error. The percentage of energy within the uniformly illuminated receiver area is 57.3%. The percentage of energy increased to 74.6% when C_{avg} is more than 60 suns, and the percentage of energy is as high as 88.7% when C_{avg} is more than 38 suns. To analyze the

optimal dimension for the target area, the spillage loss versus receiver dimension was plotted as seen in Figure 3.14(b), from which the target area dimension of 50 mm × 50 mm (exact size of one primary facet mirror) was carefully chosen due to low spillage loss of 11.6 %. The average solar concentration ratio at the target area of 50 mm × 50 mm is 68 suns. Simulation results have shown that the two-stage reflective NISC produces good uniformity of solar flux distribution at the receiver area (the red colored area in Figure 3.14(a)) and is therefore highly recommended for use in active daylighting. The result of the theoretical analysis is presented in Table 3.4 for easy reference.

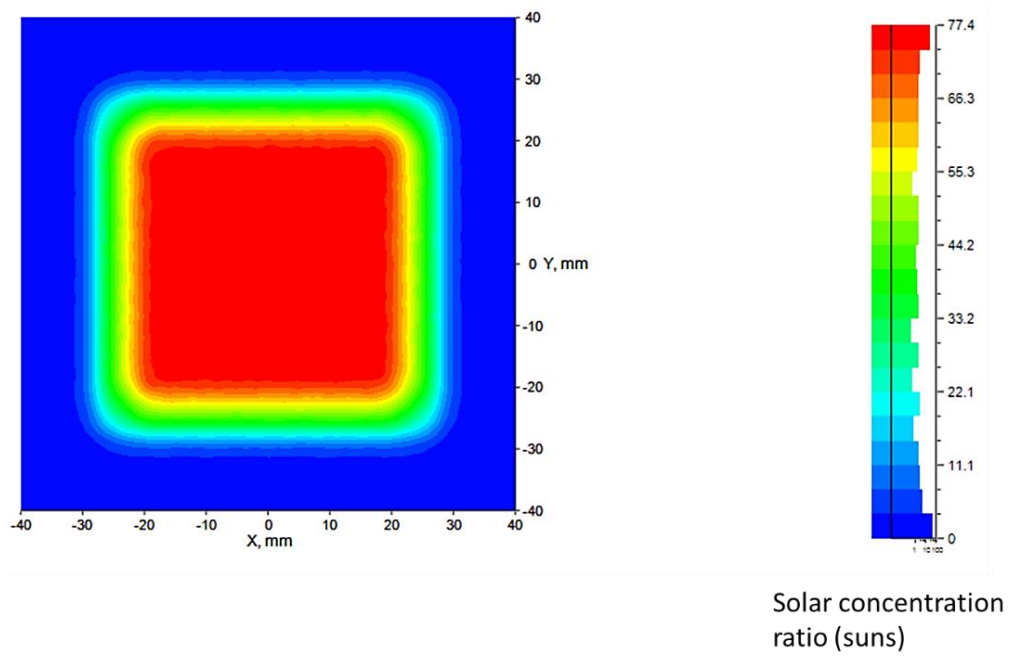

(a)

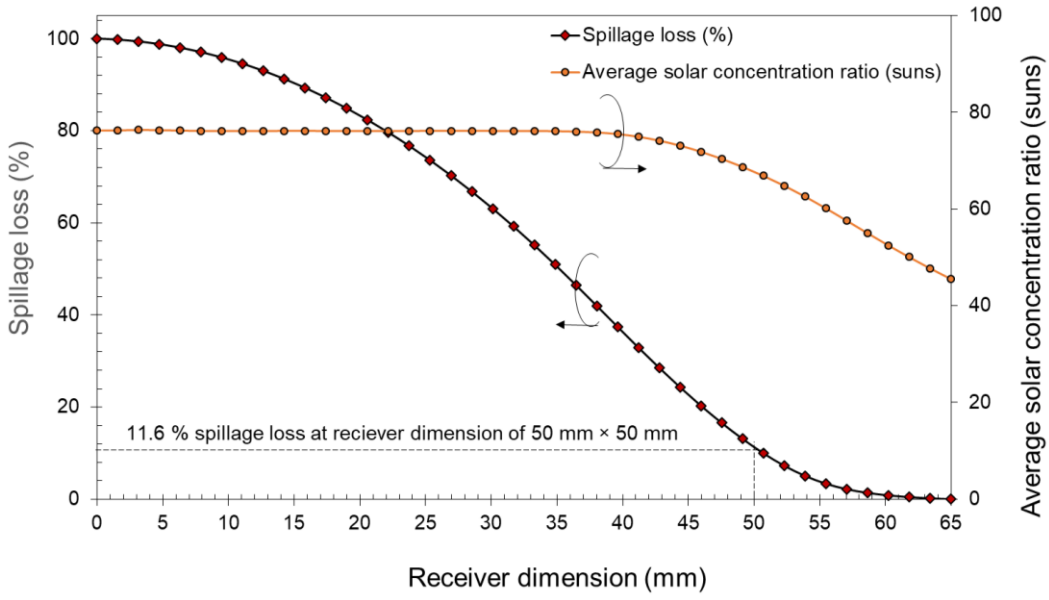

(b)

Figure 3.14: (a) 2-D plot of the simulation result showing solar flux distribution at the receiver area of the two-stage reflective non-imaging solar concentrator (NISC) prototype (b) Graph of spillage loss and solar concentration ratio vs. receiver dimension

Table 3.4: Result of the theoretical analysis on the receiver area of the two-stage reflective NISC

Parameter	Value
Central region of the receiver (uniformly illuminated area)	(38 × 38) mm
Average solar concentration ratio in the central region of the receiver	76 suns
Total focused image size	(65 × 65) mm
Selected focused image size based on spillage loss	(50 × 50) mm
Average solar concentration ratio at the target area of (50 × 50) mm	68 suns
Percentage of energy within the uniform illumination area	57.3 %
Percentage of energy for C_{avg} of more than 60 suns	74.6 %
Percentage of energy for C_{avg} of more than 38 suns.	88.7 %
Spillage loss at (50 × 50) mm receiver area	11.6 %

3.5 Hardware construction of the two-stage reflective non-imaging solar concentrator (NISC) prototype.

Different parts of the two-stage reflective NISC prototype were built at different laboratories (mechanical, electrical, etc.) of Universiti Tunku Abdul Rahman, Malaysia. All parts were assembled and the two-stage reflective NISC was placed at the leveled roof-top of the University located at a longitude of

101.79º and latitude of 3.04º. This section explains the manufacturing process of the concentrator.

The two-stage reflective NISC was manufactured in two parts: a mechanical frame with the primary and secondary reflectors and the base structure with the sun-tracking mechanism as displayed in Figure 3.4(b). Aluminum was selected as the material for the mechanical frame because of its properties such as low density, corrosion resistance, easy machining, and recyclability. 20 mm (L) × 20 mm (W) × 2 mm (T) aluminum hollow square bars were used to build the mechanical frame. The primary reflector has an outer dimension of (730 × 730) mm. It was built by placing four sets of two aluminum hollow bars with an interval distance of 85 mm as a platform for the primary mirrors to be fixed and were screwed at four corners to form a square frame. PVC plate was cut into rectangular shapes with a dimension of 125 mm (L) × 10 mm (W) × 5 mm (T) and was fixed to the two aluminum hollow bars on which the primary facet mirrors were fixed using bolts and nuts. Likewise, the mechanical frame of the secondary reflector was built using four sets of two aluminum hollow bars placed 6 cm apart and screwed at four corners to form a square frame as a platform for the secondary facet mirrors to be fixed. Four aluminum hollow bars were used to hold the primary reflector frame and the secondary reflector frame 700 mm away from each other.

Eighty flat facet mirrors of the dimension of 50 mm (L) × 50 mm (W) × 3 mm (T) were each fixed on the primary reflector frame to form a total of twenty mirror assembly sets as illustrated in Figure 3.4(a). The gap or spacing between

two primary facet mirrors within each mirror assembly set is 5 mm while the spacing between two adjacent mirror assembly set is 20 mm. Likewise, twenty secondary mirrors with a dimension of 80 mm (L) × 80 mm (W) × 3 mm (T) were each fixed on the secondary reflector frame with a spacing of 8 mm. Each facet mirror consists of six parts as shown in Figure 3.4 (a): (1) flat mirror, (2) three bolts (M4 ×60 mm), (3) PVC plate (mirror frame), (4) washers (5) compression spring (6) nuts. The preparation of the facet mirrors in the laboratory is shown in Figure 3.15.

(a.) Preparation of the facet mirror frame

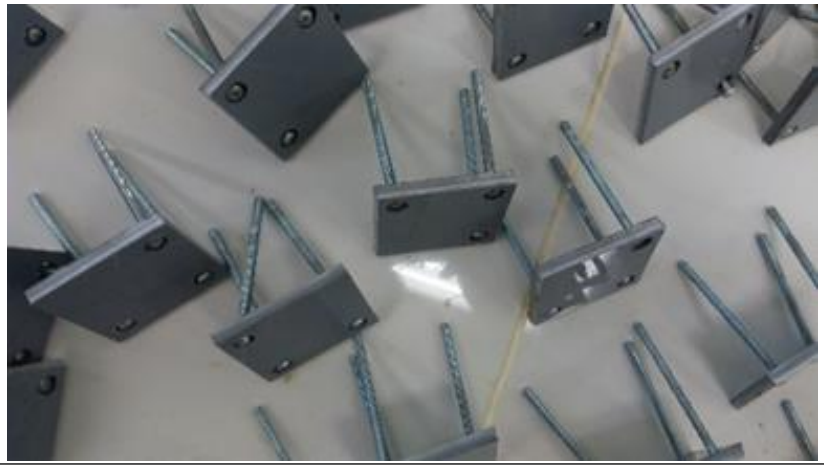

(b.) Three bolts fixed on each mirror frame

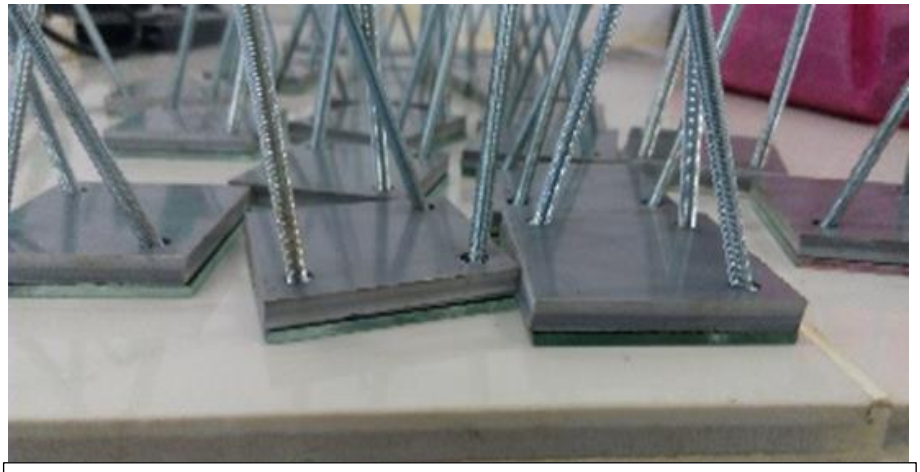

(c.) Flat facet mirrors glued to each mirror frame

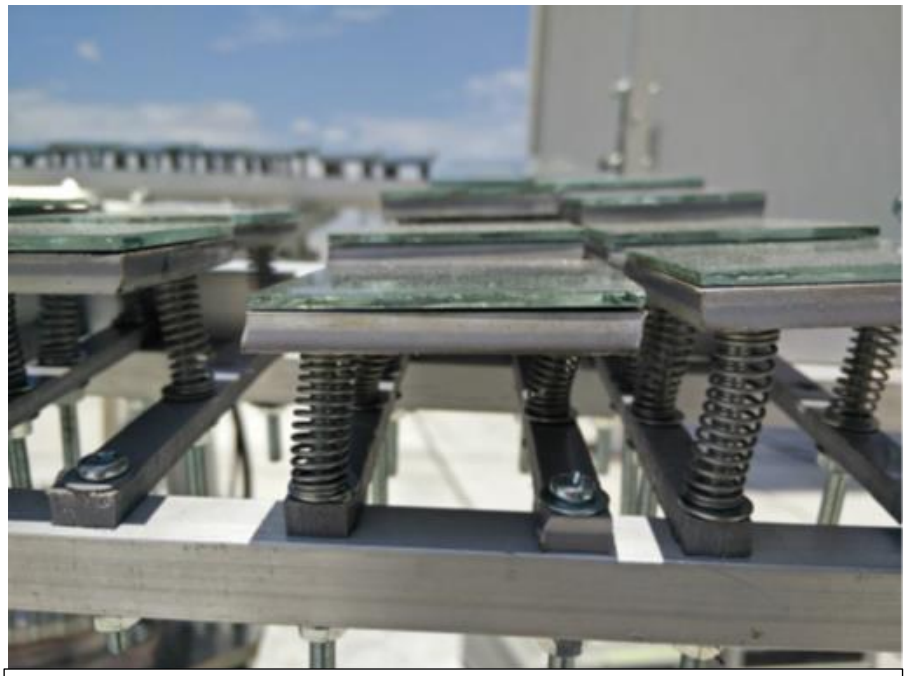

(d.) Complete facet mirror with compression springs fixed on the reflector frame

Figure 3.15: Preparation of the flat facet mirrors

To make the mirror frame, PVC plates were cut into eighty 50 mm × 50 mm square shapes and twenty 80 mm × 80 mm square shapes to match the size of the primary and secondary mirrors. Three blind holes with the same diameter as the bolt head were drilled half way through the thickness of the cut PVC plates at its four edges. A thorough hole was drilled through the other

remaining half, with the same diameter as the body of the bolt. Three bolts were then fixed on each mirror frame as illustrated in Figure 3.15. Epoxy paste was used to stick each facet mirror to the top of the PVC plate to make the mirror position stable after alignment. After which compression springs were slid through the body of the bolts. The bolt-spring assembly formed three contact points for each facet mirror; where one of them acted as the pivot point and the remaining two were adjustable. This made provision for each facet mirror to be tilted freely by manually turning the nuts of the two adjustable bolt-spring sets to focus the solar image to the target area.

To support the entire weight of the mechanical frame, the base structure was made of mild steel bars and plates. The open area of the base structure consisted of a door built with 2 mm thick PVC plates to house all electronic parts of the two-stage NISC prototype such as the Arduino, breadboard, wires, motor etc. The mechanical frame was securely attached to the base structure via custom-made connectors screwed on the upper part of the base structure. For easy mobility of the two-stage NISC, four wheels were fixed underneath the base structure alongside four adjustable leveling mounts for stability on the rooftop during operation.

The two-stage reflective NISC was designed to have dual-axis motion. The sun-tracking system consisting of the elevation (0˚- 50˚) and azimuth (0˚-360˚) driving mechanisms was installed on the base structure. A linear actuator fixed to the mechanical frame via a shaft to perform elevation motion from 0° to 50° served as the elevation driving mechanism. Finite Element Analysis

(FEA) was carried out to find the minimum force needed for moving the mechanical frame with the reflectors in an upward and downward motion; after which the ideal linear actuator was selected together with its best location in the base structure. The azimuth driving mechanism of the two-stage reflective NISC consists of a stepper motor, primary sprocket gear, and a custom-made secondary gear. The primary sprocket gear has eleven teeth. The custom-made secondary gear is made up of fifty screws on two rotating circular center hollow plates. Thus, the primary to secondary gear ratio is 11:50. The stepper motor was connected to the primary sprocket gear, and the primary sprocket gear was engaged with the custom-made secondary gear for the transmission of azimuth movement to the mechanical frame in 360°. Hence, the rotation of the secondary gear rotates the concentrator. The stepper motor used is PK264A2-SG50 model from Oriental motor with a resolution of 0.036˚ per step. Figure 3.16 illustrates the position of the primary and secondary gears in the prototype concentrator.

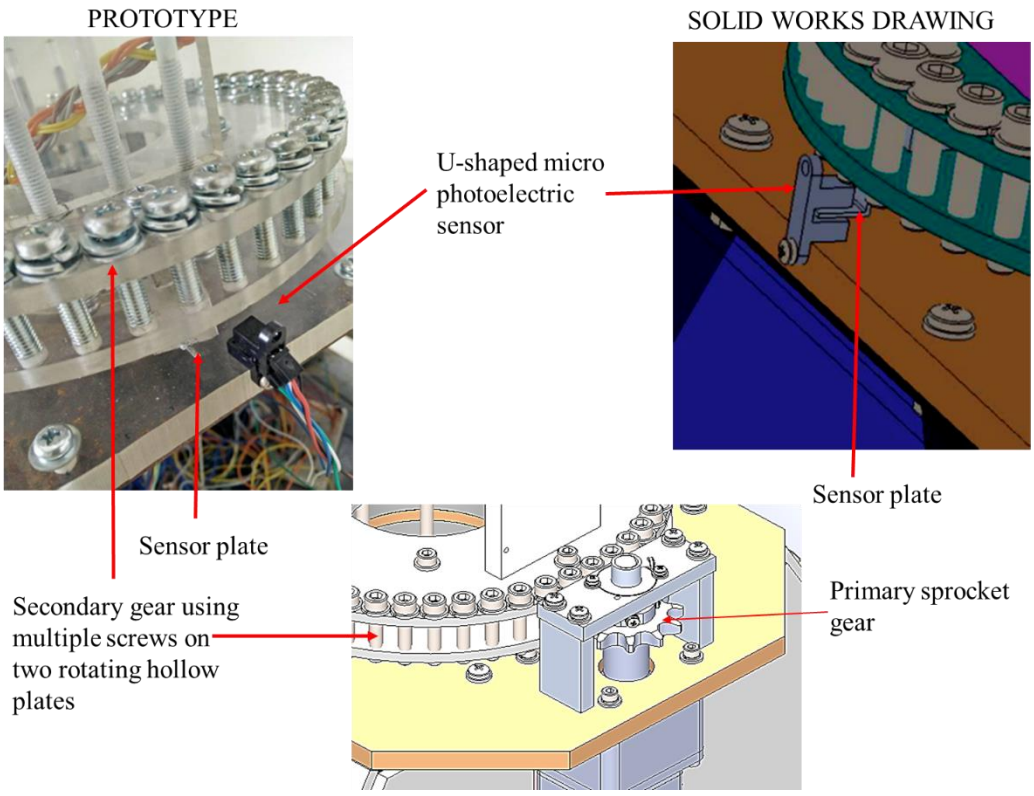

Figure 3.16: Illustration of the primary and secondary gears with the sensor and sensor plate, in both the SolidWorks drawing and the prototype

A backlash error was observed when the direction changed from clockwise to anti-clockwise and vice versa due to the gap between the primary and secondary gear teeth. To compensate this error, pulsing control of the stepper motor was used together with a U-shaped micro photoelectric sensor to increase the resolution of the rotation and to detect whether the system is rotating or not when the direction changes. U-shaped micro photoelectric sensor is a type of sensor that detects objects that pass through it. When an object passes through the U-shaped gap, the transmitter will be blocked from the receiver causing the output signal to change. Below the secondary gear, a plate was attached for blocking the sensor transmitter and receiver when it enters the sensor gap. The plate also served as an initial reference position for the solar concentrator,

implying that the sensor should always point towards the North. When there is no object between the gaps, the sensor output is high and vice versa.

The latest version of the Arduino MEGA 2560 served as a mini-computer to host the sun-tracking program for operating the system by calculating the solar angles, pulse generation, interrupts, etc. The solar-tracking system was designed as a structural closed-loop control system. Two 9-bit encoders with a resolution of 512 counts per revolution (equivalent to 0.70° per count) are used to send responses of the rotational angles about azimuth and elevation axes. With respect to the local clock time, time zone, date, latitude, and longitude of the site location; the sun-tracking algorithm computes the azimuth and elevation angles and then sends control pulse and interrupt signals to the driving mechanism in recurrent loops. The current locations of the two-stage reflective NISC are then compared with the calculated elevation and azimuth angles to get a differential value in position. The program will command the appropriate stepper motor to move the two-stage reflective NISC to the most recent calculated position if the positional difference in degrees is greater than the 0.70° resolution of the optical encoder. Figure 3.17 (a) shows the overall circuit design and Figure 3.17 (b) shows a flow chart of the tracking logic of the two-stage reflective NISC.

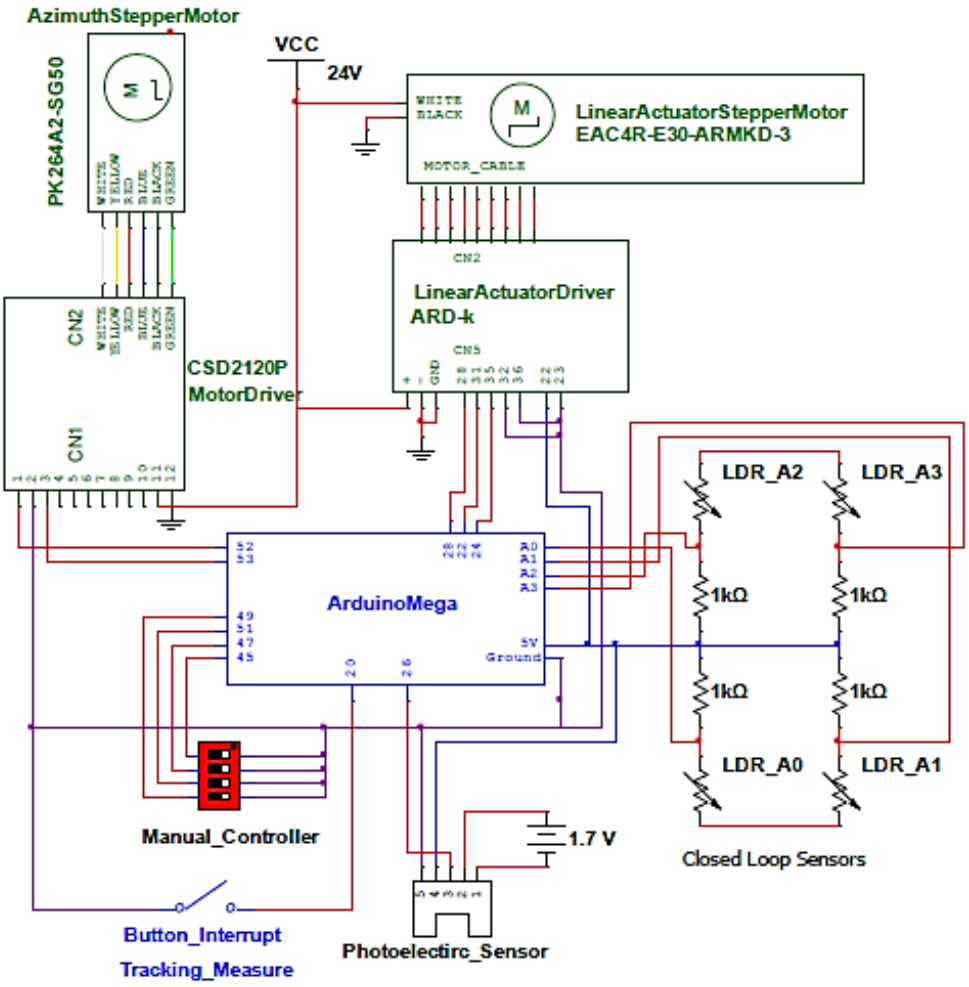
AzimuthStepperMotor
PK264A2-SG50
VCC
24V
LinearActuatorStepperMotor
EAC4R-E30-ARMKD-3
MOTOR_CABLE
LinearActuatorDriver
ARD-k
CSD2120P
MotorDriver
CN1
CN2
CN5
ArduinoMega
LDR_A2
LDR_A3
LDR_A0
LDR_A1
1kΩ
1kΩ
1kΩ
1kΩ
Closed Loop Sensors
Manual_Controller
1.7 V
Button_Interrupt
Tracking_Measure
Photoelectirc_Sensor

(A)

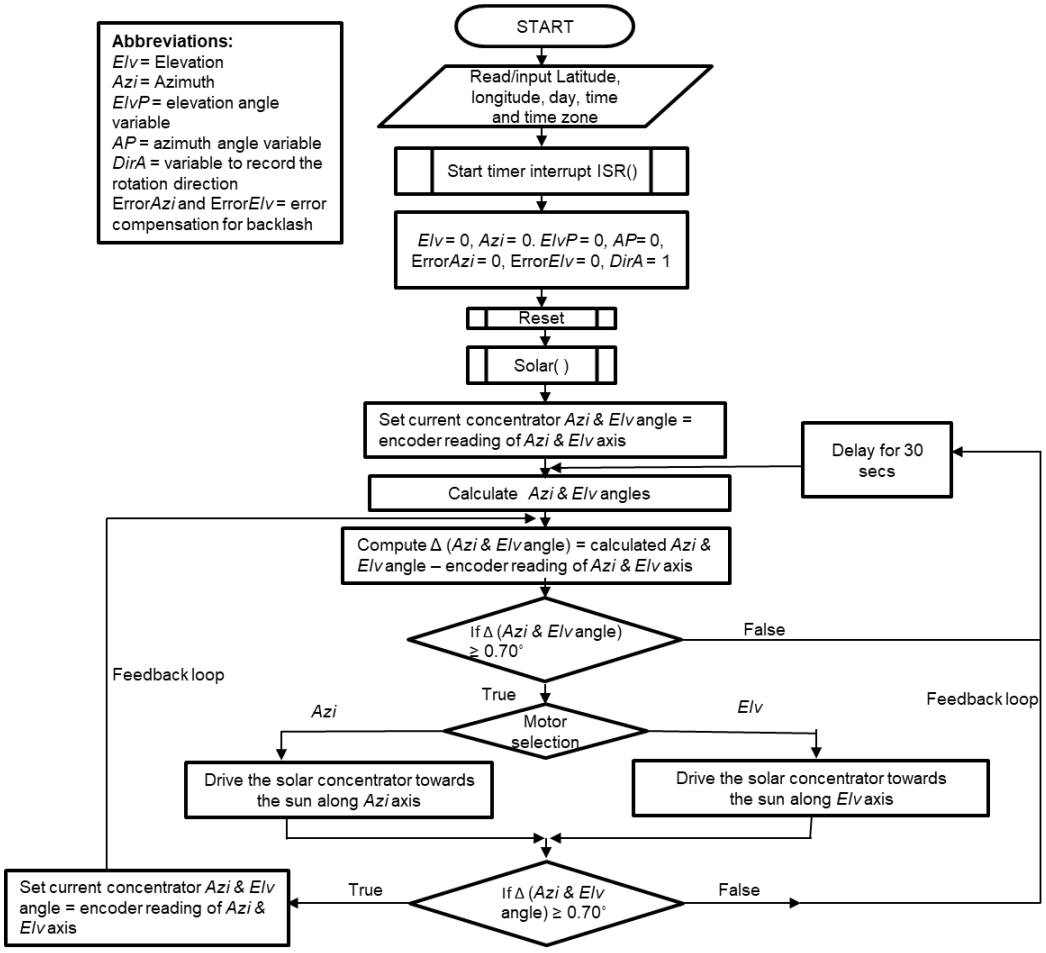

(B)

Figure 3.17 (a) Schematic diagram of the overall circuit design showing the two stepper motors, motor driver, Arduino Mega 2560, closed loop sensors, button interrupt and manual controller (b) Flow chart of the tracking logic of the two-stage reflective NISC.

The weight of the mechanical frame including reflectors is about 16 kg and the weight of the entire two-stage reflective NISC prototype including the driving mechanisms is about 42.2 kg. The specification of the two-stage reflective NISC prototype is shown in Table 3.1. Figure 3.18 illustrates the completely manufactured prototype in the laboratory and the working prototype on the roof–top.

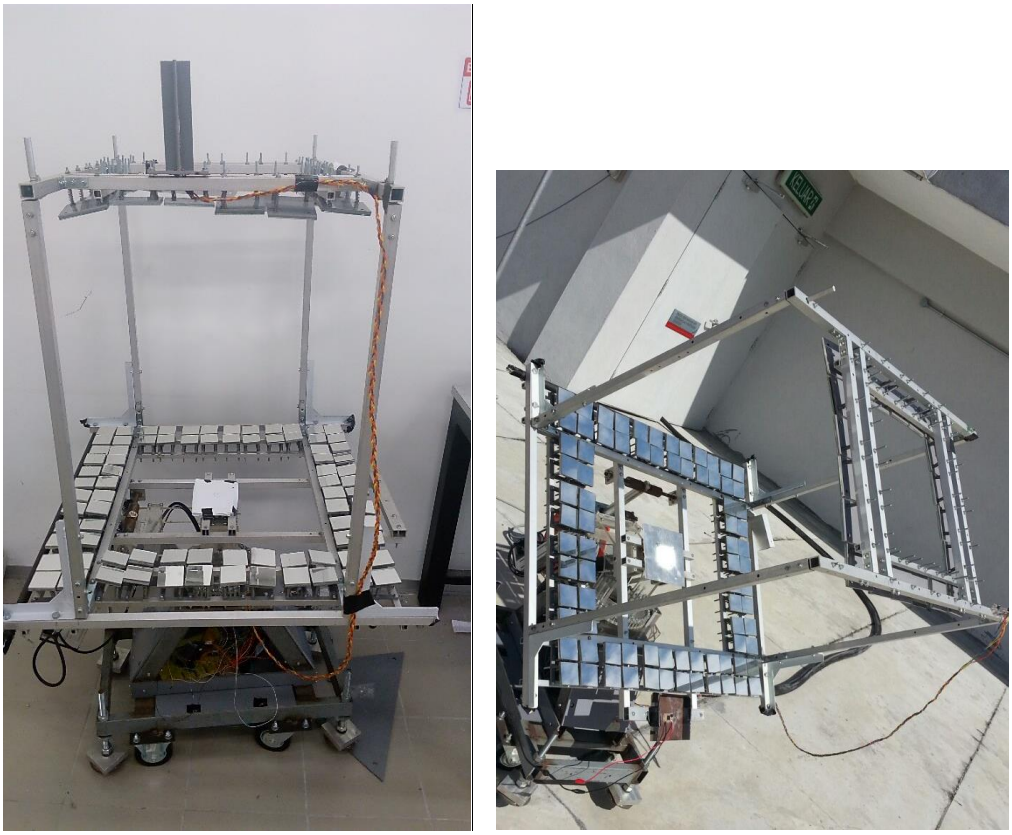

Figure 3.18: Completely manufactured prototype of the two-stage reflective NISC in the laboratory (left) and on the roof-top (right)

3.6 Optical alignment of all mirrors of the two-stage reflective NISC

After the prototype of the two-stage reflective NISC was completely built and placed on the rooftop of the University building, all the mirrors were tilted to face the sun perpendicularly so that maximum incident sunlight can be received. To align the mirrors, some steps were taken:

a.) All the mirrors were properly cleaned with cotton wool that was soaked in ethanol to remove dust particles and fingerprint stains.

b.) The primary mirrors were first aligned, followed by the secondary mirrors. To align the primary mirrors, the secondary reflector was removed and replaced with four height adjustable aluminum hollow bars with a receiver on top which is a thick sheet of plastic paper with the same dimension as the original secondary reflector. On the thick sheet of plastic paper, the new locations for the secondary mirrors were drawn out as a reference for the reflected sunlight from the primary mirror sets. After the set up was done and the sun was out with clear skies, the sun-tracking mechanism of the concentrator tracked the sun while each primary mirror set was manually adjusted such that their incident sunrays were reflected to their respective secondary mirror's new location on the plastic paper according to the new target coordinates in Table 3.3. Figure 3.19 and Figure 3.20 depicts the set-up for the primary mirror alignment. This was done one mirror after another for all primary mirror assembly sets; while adjusting the height of the secondary reflector accordingly and covering the other primary mirrors to prevent them from receiving incident rays.

Figure 3.19: Primary reflector alignment set-up showing the adjustable aluminum hollow bars

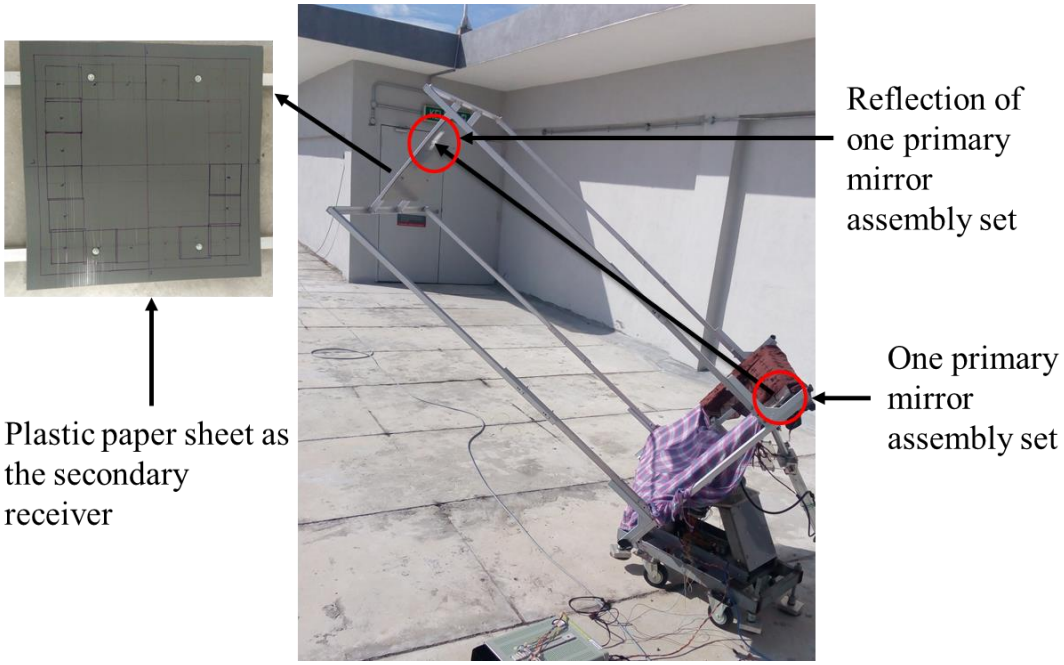

Figure 3.20: Primary mirror alignment under the sun illustrating the reflection on the plastic paper sheet

To confirm that the automatic sun-tracking position is correct, a 5 mm diameter thorough hole was drilled on top a rectangular aluminum hollow metal bar of about 100 mm length. A dent was then made directly perpendicular to the drilled hole inside the hollow bar. The rectangular aluminum hollow metal bar was tightly secured at the side of the concentrator using a G-clamp as illustrated in Figure 3.21. When the concentrator is directly facing the sun, the reflection of the sun is seen directly on top the dent through the 5 mm hole. This implies that the sun-tracking position is correct. In a situation whereby the reflection of the sun is not directly on the dent, the sun-tracking position is wrong and needs to be checked.

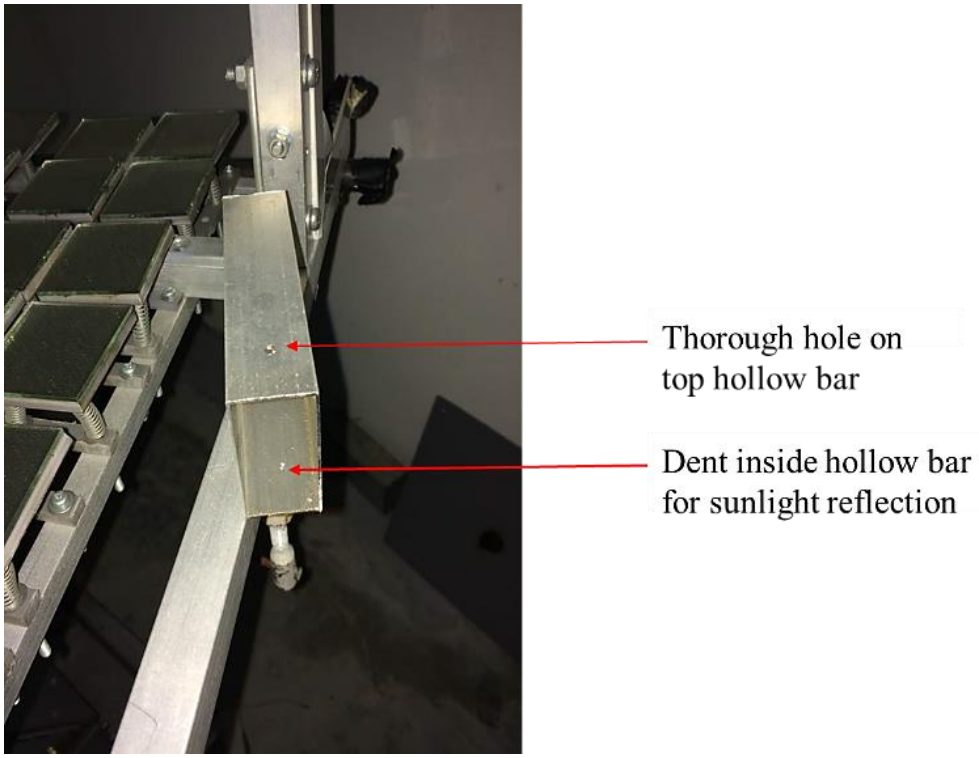

Figure 3.21: Hollow rectangular metal bar placed on the side of the concentrator to confirm correct sun-tracking position

c.) After all the primary mirrors were properly aligned, the four height adjustable aluminum hollow bars with its receiver were removed and replaced with the original secondary reflector. The incident rays from the primary mirrors were seen perfectly reflecting on their respective secondary mirror. The secondary mirrors were then individually tilted to reflect their rays to the target area of 50 mm × 50 mm one after the other while covering other secondary mirrors. The final outcome of all the reflected rays on the receiver is shown in Figure 3.22.

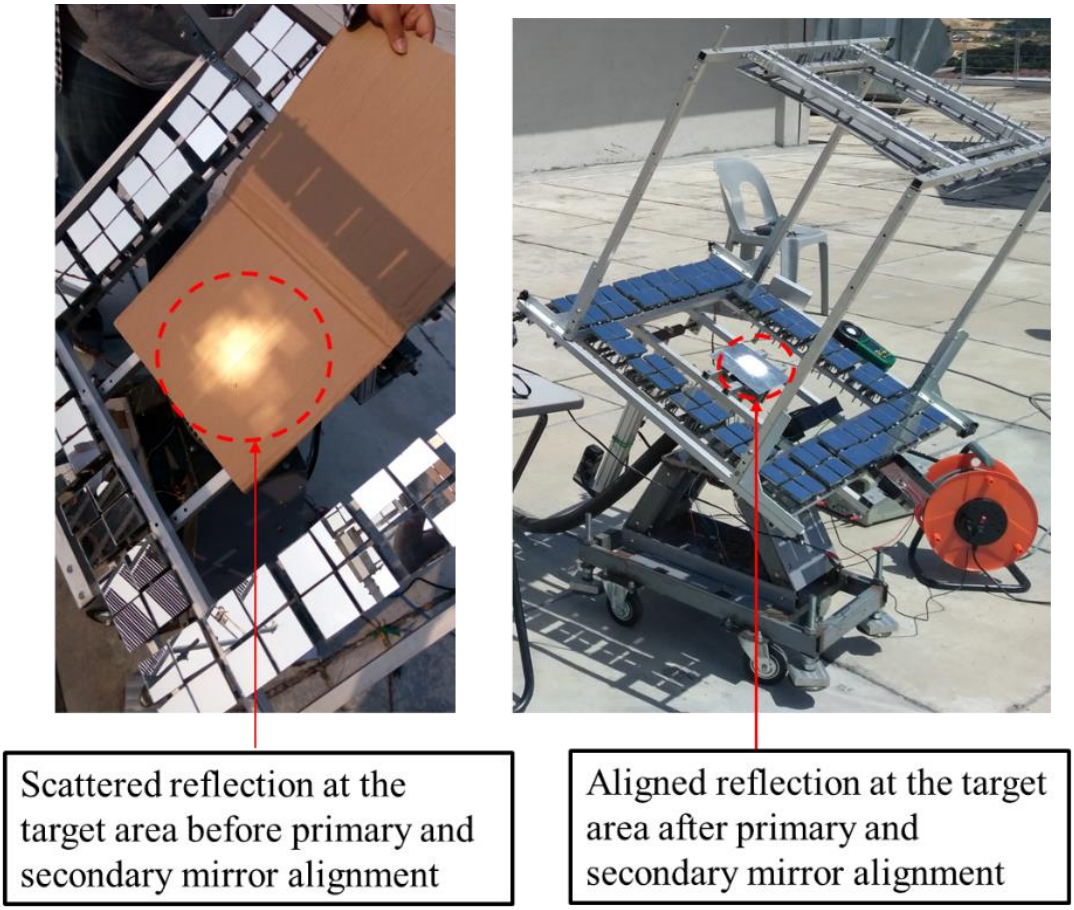

Figure 3.22: Illustration of the receiver area of the two-stage reflective NISC before and after mirror alignment

d.) I installed an application called “clinometer + bubble level” on my handphone and used it to confirm that the tilted angles of the primary and secondary mirrors correspond to the calculated tilting angles in Table 3.3. The process involved opening the application on my hand phone and calibrating it first by placing it on a very flat surface where the angle of tilt is zero. After that, the hand phone is then placed gently on each mirror for the application to measure the angle of tilt.

3.7 Optical fibers for light transmission – Selection, preparation and fiber analysis

For transmission of visible light from the receiver area to the building, model CK-120 high-performance plastic optical fibers (POFs) made by Mitsubishi Rayon Co. LTD were carefully selected. They are cost effective, flexible, have a high acceptance angle and a large core diameter that can transmit more light by means of total internal reflection. Each plastic fiber is made up of a polymethylmethacrylate (PMMA) core with a diameter of 2.945 mm and a fluorinated Polymer cladding with a diameter of 3 mm. Refer to Appendix A for technical specifications of the selected POF as provided by the manufacturer. The entrance aperture of the optical fibers was fixed at the target area which is located at the center of the primary reflector to perpendicularly face the sun. The half acceptance angle of the PMMA is 30º, making the total acceptance angle equal to 60º. The half acceptance angle as illustrated in Figure 3.23, is the maximum angle relative to the central axis of the optical fiber at which light rays can enter and be transmitted through the optical fibers. The maximum emitting angle of the light rays at the exit of the optical fiber should be equal to the half acceptance angle.

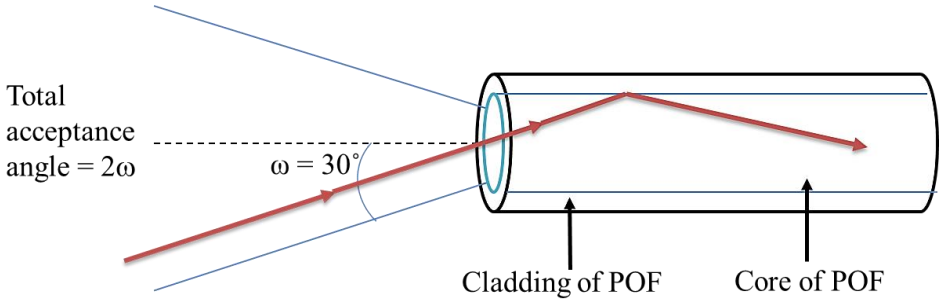

Figure 3.23: Illustration of the acceptance angle of the plastic optical fiber

After the POF has been exposed under concentrated sunlight with high temperature and UV for a long period, it would tend to melt and degrade due to its polymer properties. To prevent melting and degrading of the POF, a dielectric hot mirror filter is placed before the entrance aperture of the optical fibers to reflect or filter away an average of 70 % of ultraviolet rays (below 380 nm and above 710 nm) and an average of 98 % of infrared rays (750 nm to 1150 nm). The hot mirror has a maximum operating temperature of 400 ˚C and high transmissibility of 98 % for visible light (400 nm to 690 nm).

The optical fibers were protected from scratches, dust and dirt by neatly inserting them into black long foam embraced by an insulated pipe.

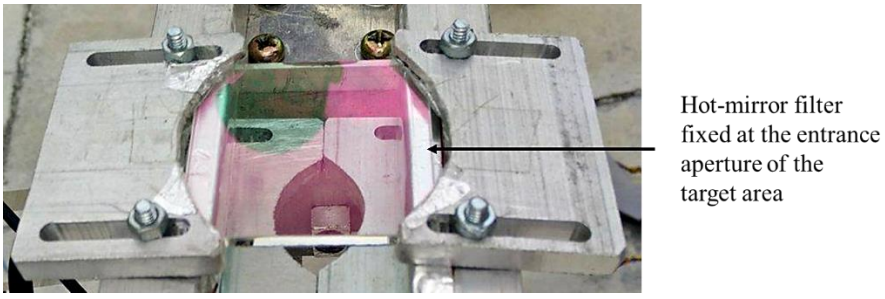

Figure 3.24: High-performance hot-mirror fixed at the receiver area of the prototype for testing

Table 3.5: Design specification and calculations for the two-stage reflective non-imaging solar concentrator (NISC) daylighting system

Parameters	Value	Parameters	Value
Area of each primary facet mirror (cm^2)	25	Average value of direct beam luminous efficacy (lm/W) as provided by Lim and Ahmad (2013) based on Malaysian climate. It is the ratio of daylight illuminance to solar irradiance)	104
Number of primary facet mirrors	80	Total transmission loss via fiber, L_{fiber} (%)	45.7
Total area of all primary facet mirrors, $A_{Reflector}$ (m^2)	0.2	Direct normal irradiance (DNI), I (W/m^2)	1000
Target area (m^2) (0.05 m × 0.05 m)	0.0025	Percentage of visible light in solar spectrum, %*VL* (%)	47
Transmissibility of visible light for hot mirror	0.98	Percentage of infrared light in solar spectrum (%)	46
Core reflective index of POF	1.49	Percentage of ultraviolet light in solar spectrum (%)	7
Numerical aperture of POF	0.50	Uniform illumination area of concentrated flux, $A_{uniform}$ (mm^2) = (38 mm × 38 mm)	1444
Maximum operating temperature of POF (°C)	70	Average solar concentration ratio within target area of 50 mm × 50 mm (suns)	68
Minimum operating temperature of POF (°C)	–55	Input solar power within target area of 50 mm × 50 mm (W) = (68 × 1000 × 0.0025)	170
Length of POF (m)	10	Visible light power as 47% of full solar spectrum (W) = 170 W × 0.47	79.9
Half acceptance angle of POF (°)	30	Input light power after the hot mirror filter (W) = 79.9 W × 0.98	78.30
Transmission loss of POF (dB/km)	≤ 200	Illuminance at the entrance aperture of the POF (lm) = luminous efficacy × input light power =104 lm/W × 78.30 W	8143.2

The target area in which the POFs are located in the prototype of the solar concentrator is (50 × 50) mm^2. Figure 3.25 illustrates that this area can accommodate three hundred and fourteen optical fibers arranged such that seven fibers are in one bundle in other to optimize the target area for indoor illumination. From Table 3.5, the prototype two-stage reflective NISC is estimated to deliver 8143.2 lm of daylight to the optical fibers at the target area.

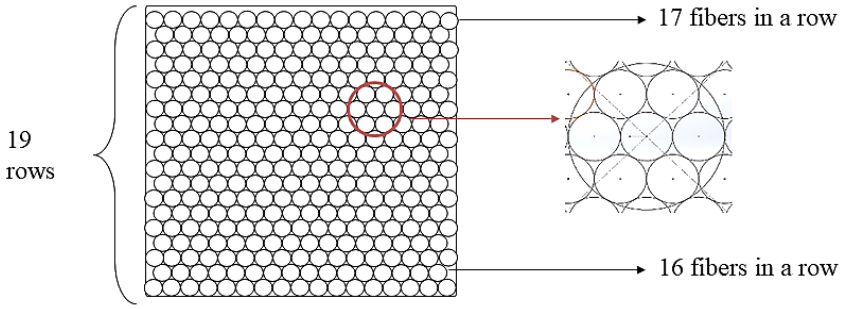

Figure 3.25: Optical fibers arrangement in the 50 mm × 50 mm target area

Since the input light power of the two-stage reflective NISC is known as 8143.2 lm, the average lumen that can be transmitted by one optical fiber can be calculated. The radius of the core of the selected POF is 1.4725 mm. Therefore, the cross-sectional area of each optical fiber is $\pi \times (1.4725\ mm)^2 = 6.81\ mm^2$ and one fiber can transmit an average of $(6.81\ mm^2 \times 8143.2\ lm)/2500\ mm^2 = 22.18$ lm. The proposed length of POF for experimental purposes is 10 m. Thus, an experiment for finding the attenuation/transmission and coupling loss called the cut-back method was performed on the 10 m long fiber. The cut-back method as illustrated in Figure 3.26 involved clamping the entrance aperture of the optical fiber using a retort stand to perpendicularly face an uninterrupted white light source. At the exit aperture of the fiber, a CPV cell was used to measure

both the short-circuit current and open-circuit voltage in order to obtain the power. The exit aperture of the fiber was firmly fixed to the flat CPV cell such that there was no gap in-between them to prevent any loss of output light. After measuring the power, 2 cm length of the optical fiber was cut off from the exit aperture using a fiber optic cutter. The surface of the new exit aperture was then polished using different grades of sandpaper, from coarse to fine (400, 800, 1200, 1500 and 2000) placed on a grinder-polisher. This was done to smoothen the surface of the fiber and make it even for the next measurement. It was also used to find out the outcome of using different grades of sandpaper to polish the surface of the optical fiber. While polishing with the grinder, its speed was adjusted between 250 rpm to 400 rpm and the water was turned on to ease the process. This cut-back method was carried out ten times and readings were taken ten times from which the attenuation was calculated as 0.36 dB/m which is slightly higher than the attenuation in the data sheet (0.2 dB/m). From this attenuation experiment, the transmission loss of 45.7 % was obtained. Thus, at the exit aperture of the 10 m length POF, the average lumen after the transmission loss should be (22.18 lm × 54.3 %) = 12.04 lm.

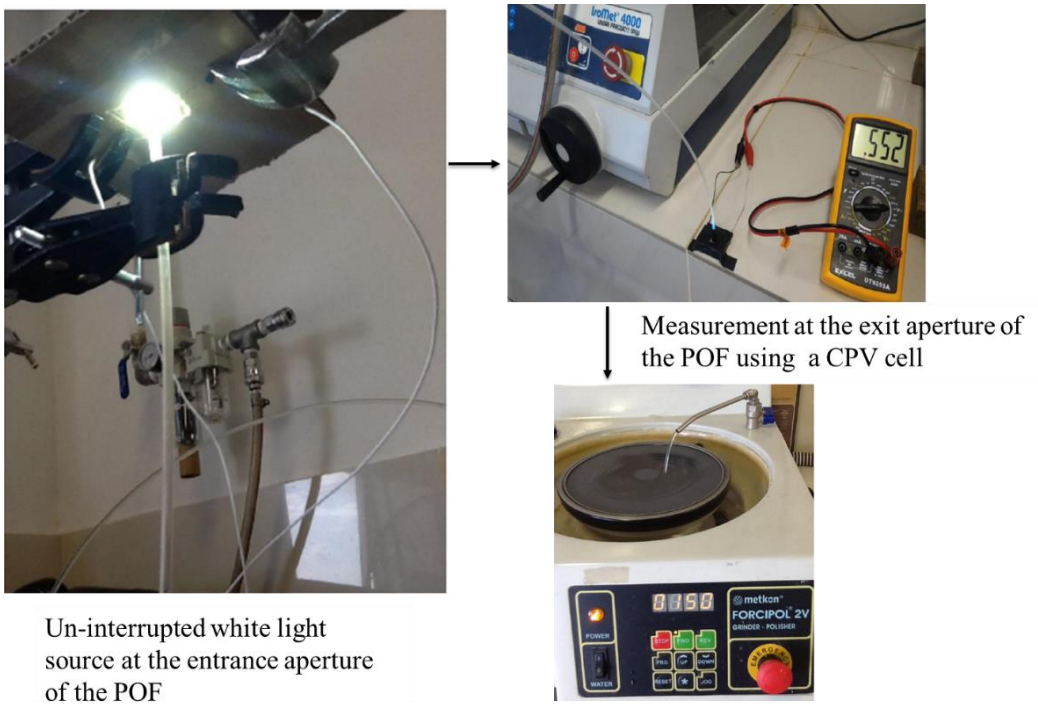

Figure 3.26: Cut-back method to find the attenuation loss of the POF

The CIBSE code (1994) for interior lighting stated the standard illuminance for visibility of a room as 500 lx; and for this study, a 6.3 m^2 room is termed a standard office area. In a standard office area of 6.3 m^2, daylighting via optical fiber requires (500 lx × 6.3 m^2) = 3150 lm to achieve 500 lx. Therefore the total number of optical fibers required is 3150/12.04 ≈ 262 fibers. The target area shown in Figure 3.25 can supply an average luminous flux of 12.04 lm × 314 = 3780.6 lm (or 600 lx for an office area of 6.3 m^2). Theoretically, an illuminance value higher than the required illuminance for a standard office area can be accomplished with the prototype two-stage reflective NISC. Thus, the average illuminance of the prototype with 600 lx for a room area of 6.3 m^2 can be used to illuminate a larger office area of (600 lx × 6.3 m^2) / 500 lx = 7.56 m^2.

For real world implementation of the prototype design, when the indoor illuminance from the two-stage reflective NISC is less than the required level, light-emitting diodes (LEDs) with model no. LUW W5AM-KYLX-4E8G will be used as complementary artificial light as it has a low power consumption and a long lifespan. The selected LED model is a high power LED with a white light source at a color temperature of 5700 K, which is in the similar range of daylight (5000 K - 6000 K). Each LED can produce 104 lm/W with the forward voltage (V_f) of 3.2 V, current of 350 mA and electrical input power of 1.12 W. For the LEDs to fully illuminate an office area of 7.56 m^2, 3780 lm is needed to achieve 500 lx and hence a total of 32.5 LEDs ≈ 33 LEDs with rated electrical power of 36.35 W is required. It implies that the illuminance produced by the two-stage reflective NISC is equivalent to 33 LEDs with electrical power of 1.12 W each. Referring to Table 3.5, the solar input power received at the target area of the two-stage reflective NISC is 170 W. Hence, the equivalent power conversion efficiency is (36.35 W/170W) × 100 % = 21.4 %.

CHAPTER 4

RESULTS AND DISCUSSION

4.1 Experimental set-up for measuring the solar concentration ratio of the two-stage reflective NISC prototype

On-site data collection to measure the solar concentration ratio (suns) was carried out for the prototype two-stage reflective NISC. Instruments involved in the experimental set-up and employed for the data collection included: a digital light meter that was firmly secured to the mechanical frame with its light sensor facing the sun – for measuring the illuminance of the sun; multimeter 1 – for measuring the short-circuit current of CPV cell 1 that is positioned under concentrated sunlight at the central region ($I_{sc\text{-}1}$) of the receiver area; multimeter 2 - for measuring the short-circuit current of CPV cell 2 that is positioned on the mechanical frame of the concentrator under one sun ($I_{sc\text{-}2}$); pyranometer – for measuring the global solar irradiance (GSI); and pyrheliometer – for measuring the direct normal irradiance (DNI). All instruments were calibrated before use and aligned to face the sun perpendicularly to ensure accurate readings were taken. Direct normal irradiance (DNI) is the direct component of solar power reaching the earth surface per square meter. Global solar irradiance (GSI) is a measure of the amount of total incoming direct and diffuse solar energy on a horizontal plane on the earth's surface.

The experimental setup for measuring the solar concentration ratio of the two-stage reflective NISC prototype is revealed in Figure 4.1.

The following equation was used to calculate the short-circuit current of CPV cell 2, contributed by only DNI ($I_{sc\text{-}2}^{DNI}$) under one sun:

$$I_{sc-2}^{DNI} = I_{sc-2} \times \frac{DNI}{GSI} \tag{4.1}$$

where $I_{sc\text{-}2}$ is the measured short-circuit current of CPV cell 2 in mA when exposed to GSI under one sun, DNI is the direct normal irradiance in W/m^2 measured by the pyrheliometer and GSI is the global solar irradiance in W/m^2 measured by the pyranometer.

After finding $I_{sc\text{-}2}^{DNI}$ and $I_{sc\text{-}1}$, the measured solar concentration ratio of the two-stage reflective NISC prototype ($C_{measured}$) can be calculated using equations (4.2) and (4.3).

$$C_{measured} = \frac{I_{sc-1}}{I_{sc-2}^{DNI}} \tag{4.2}$$

$$C_{measured} = \frac{I_{sc-1}}{I_{sc-2}} \times \frac{GSI}{DNI} \tag{4.3}$$

where $I_{sc\text{-}1}$ is the measured short-circuit current (A) of CPV cell 1 when exposed to the concentrated sunlight at the central region of the receiver.

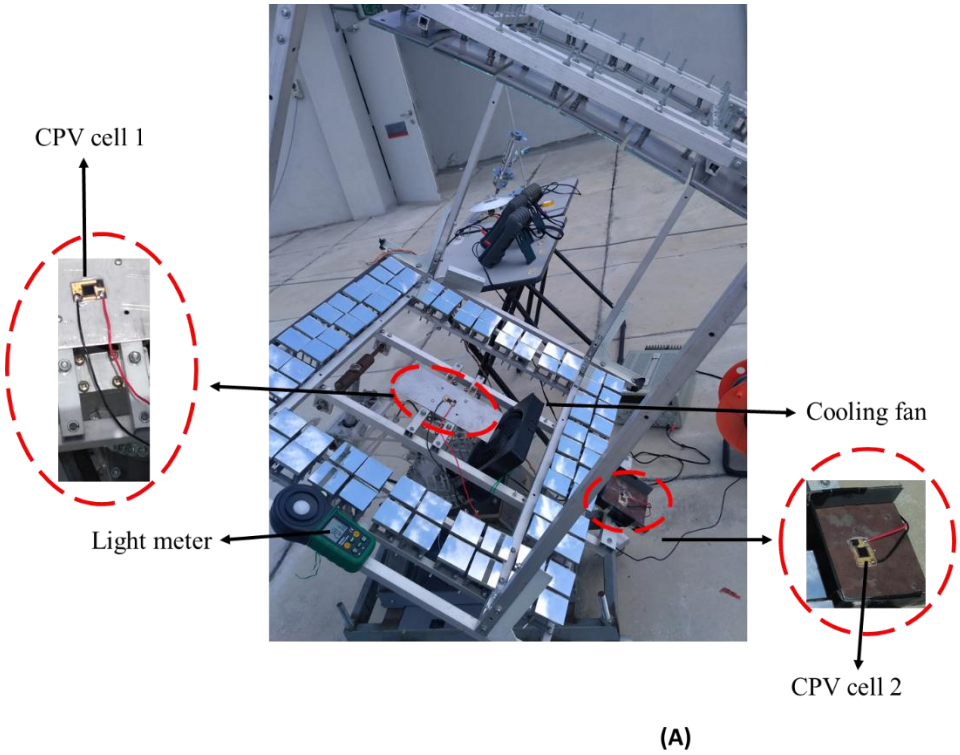

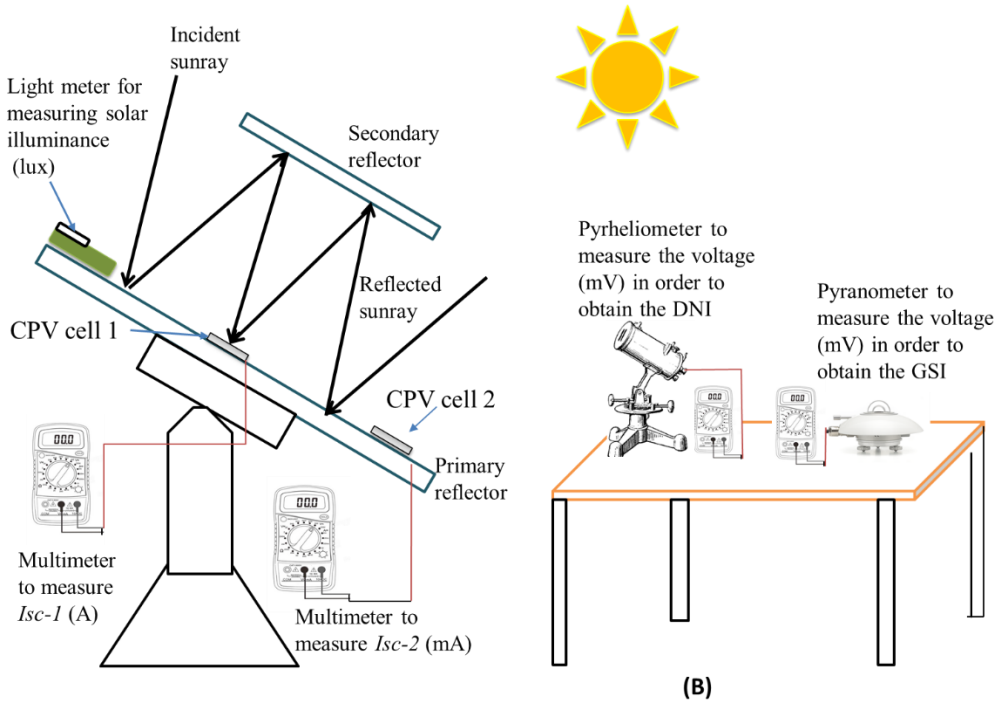

Figure 4.1 (a) Picture of the experimental setup to measure the solar concentration ratio of the two-stage reflective non-imaging solar concentrator (NISC) (b) A schematic diagram illustrating all the measurements taken during the experiment

4.2 Experimental set-up for measuring the indoor illuminance produced by the two-stage reflective NISC prototype.

The experimental setup to measure the indoor illuminance produced by the two-stage reflective NISC prototype inside the test room was similar to that of experiment 1. The only difference is that CPV cell 1 was replaced with the entrance aperture of the optical fibers aligned perpendicularly relative to the concentrated sunlight. Fourteen pieces of 3 mm diameter and 10 m long POF's were used to guide the concentrated sunlight from the prototype to the test room. The optical fibers were initially prepared in the laboratory by cutting each to a length of 10 m. To achieve an even and smooth surface for coupling the concentrated light from air to fiber, surface polishing was done using different grades of sandpaper from the most coarse to the finest grade ranging from 600 to 1500. The fibers were then grouped into two bundles; each bundle consisted of seven POFs arranged in a hexagonal manner. The two bundles of optical fibers were fixed firmly at the region of uniform illumination (38 mm × 38 mm) on the receiver, with the entrance aperture oriented perpendicularly relative to the incident sunlight as illustrated in Figure 4.2. The exit aperture of the fiber was connected to the test room, and a blackboard was positioned 2 m away from the exit aperture of the POFs. A MASTECH MS6612 digital light meter (with a spectral range of 320 nm to 730 nm) was used inside the test room and moved around the blackboard to measure the indoor illuminance based on the light emitted by the POFs at different times when the weather was sunny with clear skies.

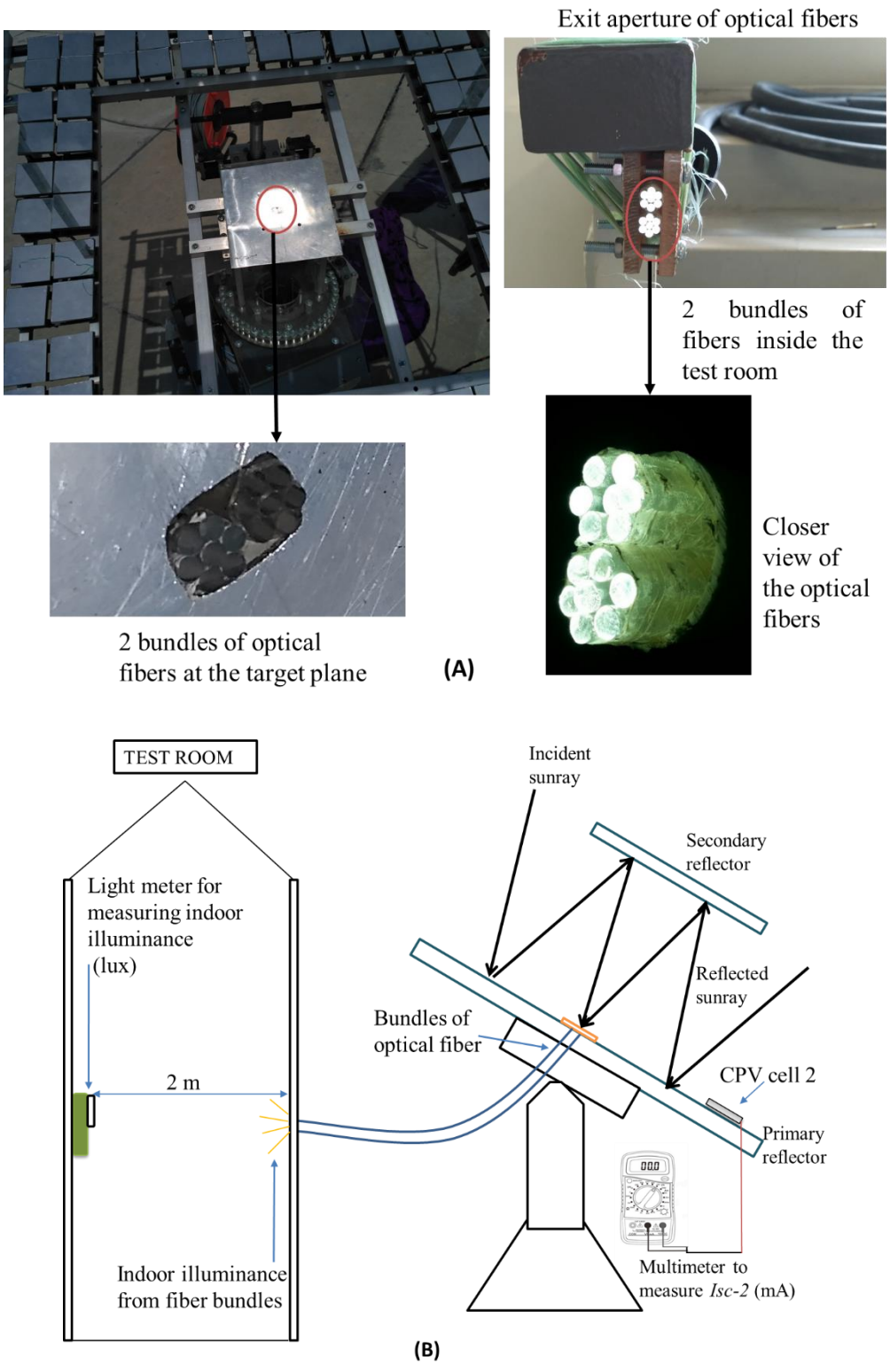

Figure 4.2 (a) Picture of the experimental setup to measure the indoor illuminance produced by the two-stage non-imaging solar concentrator (b) A schematic diagram illustrating the measurements taken during the experiment.

4.3 Experiments, results and discussion

4.3.1 Experiment 1 - to measure the solar concentration ratio of the two-stage reflective NISC prototype.

Readings were taken between August 2016 and March 2017 when the weather was sunny with clear skies and when the weather was sunny with some cloudy skies. The data collection process involved exposing the CPV cell 1 to concentrated sunlight and measuring its short-circuit current. At the same time, CPV cell 2 was used to measure the short-circuit current of 1 sun. DNI and GSI were measured concurrently.

Tables 4.1, 4.2 and 4.3 show data collection for three different days. The data in Table 4.1 were recorded on a very sunny day with no clouds (clear skies), while the data in Tables 4.2 and 4.3 were taken on a sunny day with some clouds in the sky at particular local clock times (h) and with clear skies at other local clock times (h). The measured solar concentration ratio for all the data reflects these conditions. For graphical representation, the best set of data (Table 4.1) which was taken on a very good sunny day with clear skies (14^{th} December 2016) from local clock time 11:15 h to 14:33 h is used. Figure 4.4 presents a graph to show the relationship between the measured values of average solar concentration ratio (suns) and the short-circuit currents of CPV cell 1 under concentrated sunlight with respect to the local clock time on 14^{th} December 2016. The simulated average solar concentration ratio is constant (76 suns). Figure 4.3 illustrates the relationship between measured DNI and

GSI for the 14th December, 2016 which are more or less directly proportional to each other most of the time. This was similar for all the collected data.

Table 4.1: Data collection on 14th December 2016 for GSI, DNI, short-circuit currents of CPV cell 1 and 2 and solar concentration ratio of the two-stage reflective non-imaging solar concentrator (NISC) prototype

Local Time (h)	GSI (W/m^2)	DNI (W/m^2)	DNI/GSI ratio	I_{sc-2} (mA)	I_{sc-1}(A)	Measured solar concentration ratio, $C_{measured}$ (suns)	Uncertainty of measured solar concentration ratio, $\Delta C_{measured}$ (suns)
11:15	1022	912	0.89	13.99	0.86	68.8	±1.4
11:16	1022	912	0.89	13.98	0.86	68.9	±1.4
11:18	1034	900	0.87	14.10	0.84	68.4	±1.4
11:37	1107	888	0.80	15.19	0.78	64.0	±1.3
11:38	1144	900	0.79	15.67	0.87	70.5	±1.4
11:46	1192	888	0.74	16.30	0.84	69.2	±1.4
11:47	1192	900	0.76	16.25	0.86	70.1	±1.4
12:10	1204	888	0.74	16.35	0.76	63.1	±1.3
12:12	1180	888	0.75	15.73	0.80	67.6	±1.4
12:14	1229	925	0.75	16.33	0.88	71.6	±1.5
12:22	1156	925	0.80	16.00	0.83	64.8	±1.3
12:26	1204	925	0.77	16.33	0.79	63.0	±1.3
12:27	1192	912	0.77	16.04	0.79	64.4	±1.3
13:24	1119	863	0.77	14.88	0.73	63.4	±1.3
13:26	1119	851	0.76	14.51	0.81	73.6	±1.5
13:29	1119	863	0.77	15.20	0.77	65.6	±1.3
13:33	1095	838	0.77	15.13	0.77	66.5	±1.4
13:36	1046	826	0.79	14.56	0.74	64.3	±1.3
13:37	1034	826	0.80	14.50	0.77	66.4	±1.4
13:40	998	789	0.79	13.88	0.75	68.4	±1.4
13:42	985	764	0.78	13.62	0.67	62.9	±1.3
13:51	1058	838	0.79	14.88	0.78	66.3	±1.4
13:52	1046	814	0.78	14.66	0.74	64.5	±1.3
14:32	985	715	0.73	14.06	0.68	66.7	±1.4
14:33	985	727	0.74	14.12	0.65	62.1	±1.3

Table 4.2: Data collection on 19th December 2016 for GSI, DNI, short-circuit currents of CPV cell 1 and 2 and solar concentration ratio of the two-stage reflective non-imaging solar concentrator (NISC) prototype

Local Time (h)	GSI (W/m^2)	DNI (W/m^2)	DNI/GSI ratio	I_{sc-2} (mA)	I_{sc-1}(A)	Measured solar concentration ratio, $C_{measured}$ (suns)	Uncertainty of measured solar concentration ratio, $\Delta C_{measured}$ (suns)
10:06	963	629	0.65	13.37	0.52	59.5	±1.2
10:12	976	629	0.64	13.65	0.51	57.5	±1.2
12:34	1146	752	0.66	15.50	0.74	72.9	±1.5
12:38	1134	740	0.65	15.30	0.75	75.5	±1.5
12:44	1073	703	0.65	14.80	0.67	68.6	±1.4
13:04	1134	752	0.66	15.60	0.68	65.6	±1.3
13:11	1049	678	0.65	14.45	0.62	66.4	±1.4
13:14	1049	691	0.66	14.40	0.64	67.9	±1.4
13:20	1037	629	0.61	14.22	0.57	66.5	±1.4
13:25	963	493	0.51	13.28	0.44	64.1	±1.3
13:37	634	222	0.35	8.72	0.17	54.1	±1.1

Table 4.3: Data collection on 22th December 2016 for GSI, DNI, short-circuit currents of CPV cell 1 and 2 and solar concentration ratio of the two-stage reflective non-imaging solar concentrator (NISC) prototype

Local Time (h)	GSI (W/m^2)	DNI (W/m^2)	DNI/GSI ratio	I_{sc-2} (mA)	I_{sc-1}(A)	Measured solar concentration ratio, $C_{measured}$ (suns)	Uncertainty of measured solar concentration ratio, $\Delta C_{measured}$ (suns)
10:20	951	777	0.82	13.50	0.64	58.1	±1.2
10:27	951	777	0.82	13.50	0.67	60.8	±1.2
10:31	963	764	0.79	13.50	0.69	64.4	±1.3
10:34	963	777	0.81	13.60	0.71	64.7	±1.3
10:38	963	789	0.82	13.60	0.70	62.8	±1.3
10:48	988	777	0.79	13.90	0.71	65.0	±1.3
10:55	1049	801	0.76	14.70	0.66	58.8	±1.2
11:05	963	752	0.78	13.85	0.64	59.2	±1.2
11:09	1000	814	0.81	14.15	0.73	63.4	±1.3
11:13	1049	851	0.81	14.55	0.81	68.6	±1.4
11:17	1037	838	0.81	14.45	0.82	70.2	±1.4
11.23	1049	838	0.80	14.80	0.84	71.0	±1.4
11:30	1049	801	0.76	14.85	0.71	62.6	±1.3

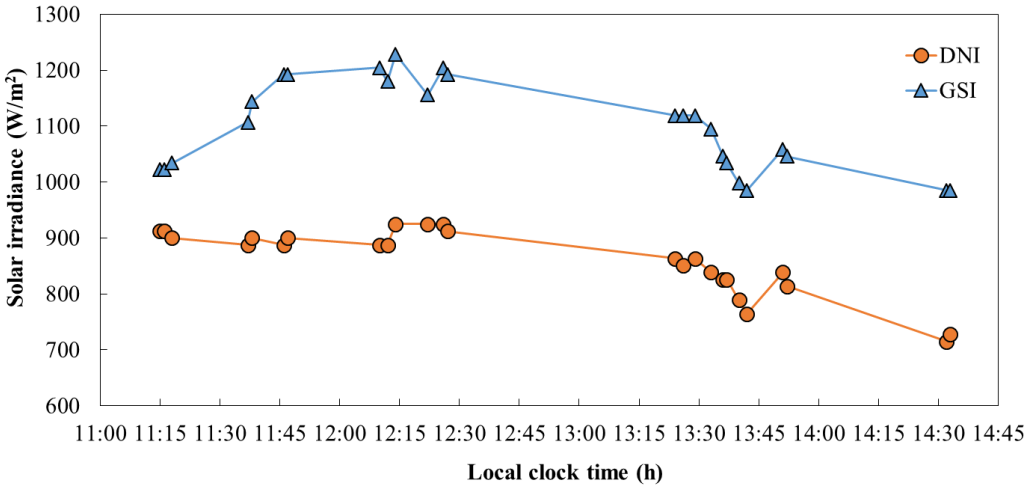

Figure 4.3: Graph to show the relationship between DNI and GSI for the 14th December, 2016.

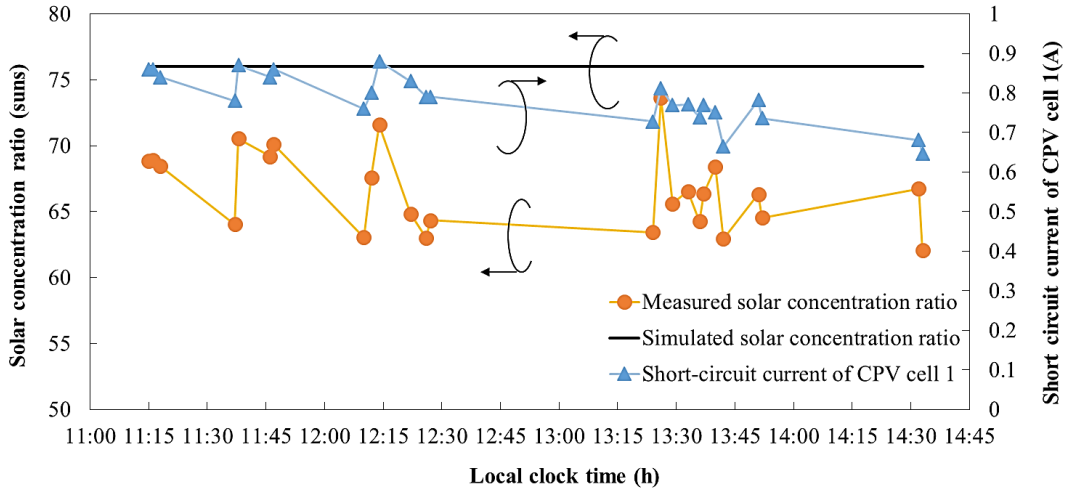

Figure 4.4: Graph to show the relationship between short-circuit current of CPV cell 1 and solar concentration ratio (measured and simulated results) versus local clock time on 14th December 2016

(Note: The arrows in the graph indicate the vertical axes of the line graphs plotted.)

4.3.2 Result and discussion of experiment 1

In Figure 4.4, the measured solar concentration ratio of the two-stage reflective NISC prototype varied between 62 suns and 74 suns throughout the period of measurement. This is selected as the best result obtained as the data was taken when the sun was at its peak. In Table 4.2, the measured solar concentration ratio varied between 54 suns and 76 suns throughout the period of measurement; and in Table 4.3, the measured solar concentration ratio varied between 58 suns and 71 suns throughout the period of measurement. The reason for this variation is the random error which occurred during measurement of short-circuit currents from CPV cell 1 and 2. Several factors such as the sun-tracking accuracy, temperature variation of the CPV cell, and measurement error of the multimeter (±1.2 % for current and ±0.8 % for voltage as obtained from

the user manual for GW INSTEK GDM-394/396 multimeter seen in Appendix B) can cause the random error to occur. The short-circuit current of CPV cell 1 was measured and used to calculate the concentration ratio at the uniformly illuminated receiver area of the concentrator. During the experiment, the temperature of the CPV cell increased after being exposed to the concentrated sunlight for a few seconds. A cooling fan was attached closely to CPV cell 1 to fasten the cooling process before focusing the concentrated sunlight on the CPV cell to take new readings. It was observed that the measured short-circuit current increased when the temperature of the CPV cell increased; it dropped as the CPV cell 1 was cooled down. This is due to the fact that for multiple junction CPV cells, the temperature co-efficient is approximately 0.001 mA/˚C for 1 sun at temperature ranging from 25 ˚C to 80 ˚C. Hence, for the two-stage reflective NISC that has a maximum solar concentration ratio of 76 suns as obtained from the numerical simulation, the temperature co-efficient is 0.076 mA/ ˚C. It can be concluded that the short-circuit current of the CPV cell varied with respect to the change in temperature.

From Table 4.1, the average measured solar concentration ratio is 66.6 suns with a calculated standard deviation of 3.0 suns and the simulated average solar concentration ratio is 76 suns. Thus, the reflectivity of the facet mirror can be calculated as $\sqrt{\frac{66.6-1}{76-1}} = 0.935 = 93.5\ \%$. One sun is subtracted in the formula because the reflectivity of the facet mirrors is not affected by the direct sunlight coming in from the central region of the secondary reflector. The calculated reflectivity falls in the range of the reflectivity of the mirror as specified by the manufacturer (90 % - 94 %). Also, from the data in Tables 4.2

and 4.3, the calculated reflectivity fell in the range of the manufacturer's specification which are 93 % and 92 % respectively.

The uncertainty of the measured solar concentration ratio ($\Delta C_{measured}$) is dependent on the measurement error of the short-circuit current of CPV cell 1 ($\Delta I_{sc\text{-}1}$), measurement error of the short-circuit current of CPV cell 2 ($\Delta I_{sc\text{-}2}$), the measurement error of DNI voltage (ΔV_{DNI}) and the measurement error of GSI voltage (ΔV_{GSI}) as shown in the following expression:

$$\left(\frac{\Delta C_{measured}}{C_{measured}}\right)^2 = \left(\frac{\Delta I_{sc-1}}{I_{sc-1}}\right)^2 + \left(\frac{\Delta I_{sc-2}{}^{DNI}}{I_{sc-2}{}^{DNI}}\right)^2 + \left(\frac{\Delta V_{DNI}}{V_{DNI}}\right)^2 + \left(\frac{\Delta V_{GSI}}{V_{GSI}}\right)^2 \tag{4.4}$$

$$\Delta C_{measured} = \sqrt{\left[\left(\frac{\Delta I_{sc-1}}{I_{sc-1}}\right)^2 + \left(\frac{\Delta I_{sc-2}{}^{DNI}}{I_{sc-2}{}^{DNI}}\right)^2 + \left(\frac{\Delta V_{DNI}}{V_{DNI}}\right)^2 + \left(\frac{\Delta V_{GSI}}{V_{GSI}}\right)^2\right]} C_{measured} \tag{4.5}$$

where $\Delta I_{sc\text{-}1}$ and $\Delta I_{sc\text{-}2}$ are ± 1.2%; ΔV_{DNI} and ΔV_{GSI} are ± 0.8%. Given that DNI = V_{DNI}/8.11 and GSI = V_{GSI}/8.22, both values of 8.11 and 8.22 are constants as provided in the specifications of the pyrometer and the pyrheliometer respectively. Equation 4.5 was used in calculating the uncertainty values for the data presented in Tables 4.1, 4.2 and 4.3.

4.3.3 Experiment 2 - to measure the indoor illuminance produced by the two-stage reflective NISC

At different times of the day when the DNI was steady, the indoor illuminance was measured at a distance of 2 m away from the exit aperture of the optical fibers inside the test room. The background illuminance value of

the test room was first measured and then subtracted from the measured indoor illuminance values from the optical fibers. Simultaneously, the DNI, GSI and short-circuit currents for CPV cell 2 were recorded. This experiment was conducted a number of times for a duration of three months; but in this thesis, data collection for four days: 22nd December, 2016 from 11:38 h to 13:14 h, 29th December, 2016 from 14:38 h to 15:11 h, 30th December, 2016 from 13:56 h to 15:11 h and 16th February, 2017 from 14:05 h to 14:31 h are presented in Tables 4.4, 4.5, 4.6 and 4.7. The data presented in Tables 4.4 and 4.5 were collected on a sunny day but with a low DNI and some clouds in the sky. This is why the illuminance values measured in the test room throughout the experiments performed on 22nd December, 2016 and on 29th December, 2016 were lower than expected with an average deviation of 29% and 16% respectively between experimental and theoretical illuminance results. The data presented in Tables 4.6 and 4.7 were collected on a sunny day with clear skies. The illuminance values measured in the test room throughout the experiments performed on 30th December, 2016 and on 16th February, 2017 were higher with an average deviation of 11% and 8% respectively between experimental and theoretical illuminance results.

For graphical representation, the set of data with higher illuminances (Tables 4.6 and 4.7) are plotted. Figure 4.5 is a graph to show the relationship between the values of DNI and GSI for the 30th December, 2016 and 16th February, 2017 which are mostly directly proportional to each other. Figure 4.6 is a graph of comparison between theoretical and experimental results for

the indoor illuminance of the prototype versus local clock time (h) on 30th December, 2016 and 16th February, 2017.

Table 4.4: Experimental results for indoor illuminance measured on 22nd December, 2016 in comparison with the theoretical results.

Local Time (h)	GSI (W/m^2)	DNI (W/m^2)	Indoor Illuminance (lx)		Deviation between experimental and theoretical results (%)	Uncertainty of experimental result for indoor illuminance (lx)
			Experimental result	Theoretical result		
11:38	985.40	715	38.7	74.5	48.0	±2.3
11:40	1034.06	740	38.7	77.0	49.8	±2.3
11:42	1009.73	740	43.4	77.0	43.7	±2.6
11:43	1021.90	740	45.5	77.0	41.0	±2.7
11:45	1058.39	789	57.8	82.2	29.7	±3.5
11:47	1082.73	777	56.8	80.9	29.7	±3.4
11:48	1058.39	789	54.4	82.2	33.8	±3.3
11:49	1046.23	777	56.7	80.9	29.8	±3.4
11:53	1058.39	789	58.3	82.2	29.0	±3.5
11:59	997.57	703	51.2	73.2	30.1	±3.1
12:00	985.40	678	56.5	70.6	19.9	±3.4
12:03	1034.06	727	57.7	75.7	23.8	±3.5
12:06	1058.39	764	53.7	79.6	32.5	±3.2
12:09	985.40	691	55.9	71.9	22.3	±3.4
12:14	973.24	678	56.9	70.6	19.4	±3.4
12:16	900.24	604	47.9	62.9	23.8	±2.9
12:17	912.41	617	45.0	64.2	29.9	±2.7
12:21	936.74	703	46.3	73.2	36.7	±2.8
12:27	912.41	604	48.6	62.9	22.7	±2.9
12:31	888.08	580	45.4	60.3	24.7	±2.7
12:35	936.74	617	46.9	64.2	26.9	±2.8
12:40	924.57	604	45.4	62.9	27.9	±2.7
12:44	912.41	567	39.4	59.1	33.3	±2.4
12:48	1021.90	666	55.9	69.3	19.4	±3.4
12:53	1034.06	641	50.6	66.8	24.2	±3.0
13:08	936.74	518	42.0	53.9	22.0	±2.5
13:12	924.57	481	37.1	50.1	26.0	±2.2
13:14	863.75	419	34.3	43.6	21.3	±2.1

Table 4.5: Experimental results for indoor illuminance measured on 29th December, 2016 in comparison with the theoretical results

Local Time (h)	GSI (W/m^2)	DNI (W/m^2)	Indoor Illuminance (lx)		Deviation between experimental and theoretical results (%)	Uncertainty of experimental result for indoor illuminance (lx)
			Experimental result	Theoretical result		
14:38	1204.38	912	77.7	95.0	18.2	±4.7
14:59	1180.05	912	78.4	95.0	17.5	±4.7
14:53	1240.88	912	79.6	95.0	16.2	±4.8
14:55	1277.37	900	77.4	93.7	17.4	±4.6
15:00	1265.21	912	79.2	95.0	16.6	±4.8
15:02	1228.71	912	81.3	95.0	14.4	±4.9
15:04	1204.38	888	84.0	92.4	9.1	±5.0
15:06	1204.38	900	82.5	93.7	12.0	±4.9
15:11	1313.87	900	71.4	93.7	23.8	±4.3

Table 4.6: Experimental results for indoor illuminance measured on 30th December, 2016 in comparison with the theoretical results.

Local Time (h)	GSI (W/m^2)	DNI (W/m^2)	Indoor Illuminance (lx)		Deviation between experimental and theoretical results (%)	Uncertainty of experimental result for indoor illuminance (lx)
			Experimental result	Theoretical result		
13:56	850.80	851	92.0	88.6	- 4.0	±5.5
14:00	863.13	863	92.7	89.9	-3.0	±5.6
14:06	801.48	802	80.8	83.4	3.2	±4.8
14:50	912.45	913	78.4	95.0	17.5	±4.7
14:53	912.45	913	79.6	95.0	16.2	±4.8
14:55	912.45	913	77.4	95.0	18.5	±4.6
15:00	900.12	900	79.2	93.7	15.5	±4.8
15:02	912.45	913	81.3	95.0	14.4	±4.9
15:04	912.45	913	84.0	95.0	11.6	±5.0
15:06	887.79	888	82.5	92.4	10.7	±4.9
15:11	900.12	900	71.4	93.7	23.8	±4.3

Table 4.7: Experimental results for indoor illuminance measured on 16th February, 2017 in comparison with the theoretical results

Local Time (h)	GSI (W/m^2)	DNI (W/m^2)	Indoor Illuminance (lx)		Deviation between experimental and theoretical results (%)	Uncertainty of experimental result for indoor illuminance (lx)
			Experimental result	Theoretical result		
14:05	1094.89	900	84.0	93.7	10.4	±5.0
14:06	1094.89	900	72.1	93.7	23.0	±4.3
14:07	1082.73	888	76.9	92.4	16.8	±4.6
14:09	1082.73	888	85.8	92.4	7.2	±5.1
14:11	1070.56	888	91.3	92.4	1.2	±5.5
14:12	1082.73	888	88.9	92.4	3.8	±5.3
14:15	1107.06	888	85.0	92.4	8.1	±5.1
14:16	1131.38	888	81.8	92.4	11.5	±4.9
14:27	1058.39	888	82.2	92.4	11.0	±4.9
14:29	1058.39	888	94.0	92.4	-1.7	±5.6
14:31	1070.56	888	92.7	92.4	-0.3	±5.6

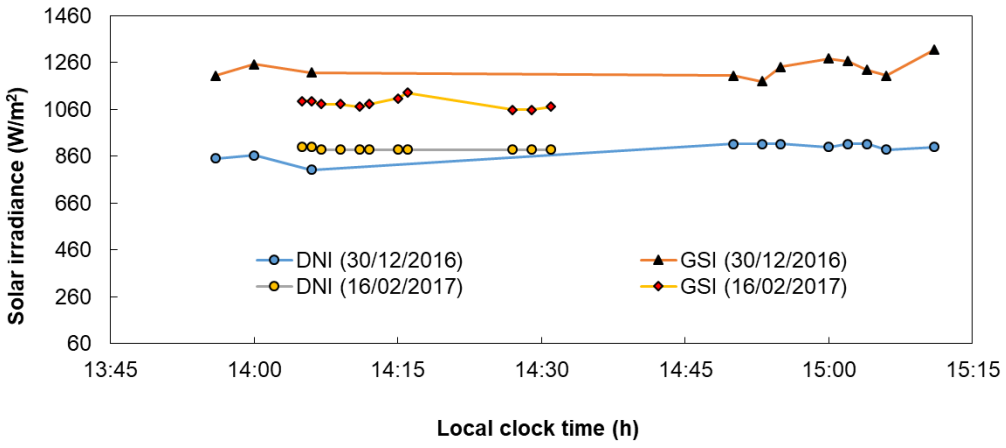

Figure 4.5: Graph to show the relationship between DNI and GSI for the 30th December, 2016 and 16th of February, 2017.

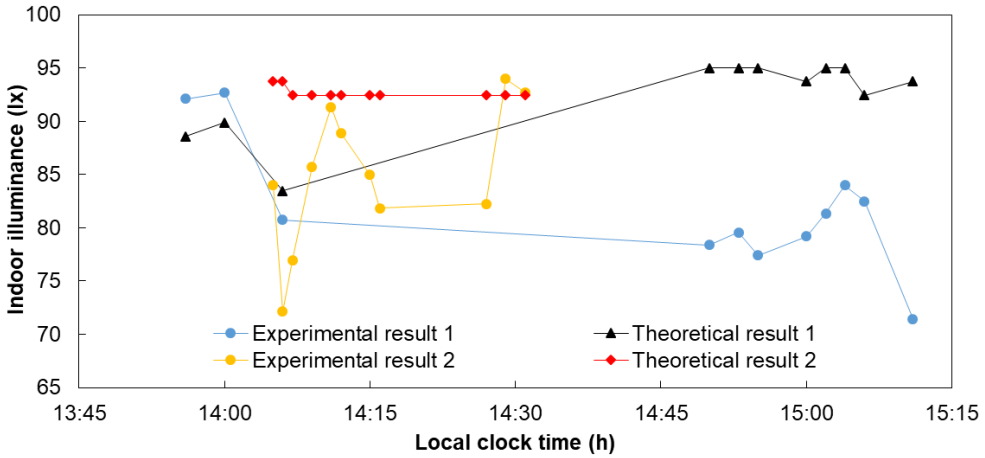

Figure 4.6: Graph to show a comparison between theoretical and experimental results for the indoor illuminance of the active daylighting system versus local clock time on 30th December 2016 and 16th February 2017.

4.3.4 Results and discussion of experiment 2

In Table 4.4, the deviation between experimental and theoretical results decreased abruptly from 41% at 11:43 h to 29.7% at 11:45 h and then increased to 33.8% at 11:48 h on 22nd December, 2016. In Table 4.5, the deviation between experimental and theoretical results decreased sharply from 14.4% at 15:02 h to 9.1% at 15:04 h and then increased suddenly to 12% at 15:06 h and further increased again to 23.8% at 15:11 h on 29th December 2016. In Table 4.6, the deviation between experimental and theoretical results increased sharply from 3.2% at 14:06 h to 17.5 % at 14:50 h and then reduced to 10.7% at 15:06 h and increased sharply again to 23.8% at 15:11 h on 30th December 2016. In Table 4.7, the deviation also increased suddenly from 10.4% at 14:05 h to 23.0% at 14:06 h; but dropped significantly from 16.8% at 14:07 h to 7.2% at 14:09 h on 16th February 2017. Due to these drops in the illuminance

with respect to the weather change, LEDs would be used for compensation as explained in section 3.7. These occurrences indicated that the deviation could be caused by both random and systematic errors. Random error is mainly caused by the measurement error of the light meter with the uncertainty value of ± 6% as obtained from the instruction manual for MASTECH Digital Light Meter MS6612. Therefore, the uncertainty of the measured indoor illuminance can be determined as measured indoor illuminance × 6 %. On the other hand, the pointing error of the sun-tracking system is the major cause of the systematic error. The accuracy of the sun-tracking system depends on the resolution of a 9-bit absolute encoder. When the absolute encoder senses that the sun position has deviated by 0.70° away from the perfect sun-tracking condition, it sends signals to the control system to activate the driving system to track the sun. When there is an increase in pointing error, focused sunlight would still be received by the optical fibers at the target area, but the illuminance output would be affected significantly due to light transmission loss, because the incident angle would have increased relative to the optical fiber (Song *et al*., 2014). Regardless of a higher tolerance of the two-stage reflective NISC prototype towards pointing error in comparison to a conventional solar concentrator, the increase in the incident angle can still cause some focused sunlight to not get into the optical fibers. To save the cost of the prototype design, a lower resolution of absolute encoder is deliberately used to provide a feedback signal of the sun position with the pointing error of up to 0.70°. Result of the spillage loss analysis for sun-tracking errors ranging from 0˚-1˚ presented in Table 4.8 has shown that the transmission loss is still within the acceptable range. This is because at tracking error of 0.8˚, the

average solar concentration ratio at both the uniformly illuminated area (38 mm × 38 mm) and the receiver area (50 mm × 50 mm) are more than half of the average solar concentration ratio at perfect sun-tracking condition with 0˚ error. This is also similar for the percentage of energy within the uniformly illuminated area and within the receiver area as shown in Table 4.8. Therefore, for pointing error of 0.70 ˚, a better result is achievable and a reasonable level of daylighting can still be produced. This proves why the two-stage reflective non-imaging solar concentrator daylighting system is less-sensitive to pointing error of its sun-tracking system.

Table 4.8: Spillage loss analysis for sun-tracking errors of 0˚, 0.2˚, 0.4˚, 0.6˚, 0.8˚ and 1˚ for the two-stage NISC with L = 70 cm.

Tracking error	**0˚**	**0.2˚**	**0.4˚**	**0.6˚**	**0.8˚**	**1˚**
Average solar concentration ratio in the uniformly illuminated area (38 mm × 38 mm)	76 suns	73 suns	66 suns	55 suns	43 suns	33 suns
Average solar concentration ratio at the receiver area of (50 × 50) mm	68 suns	64 suns	57 suns	48 suns	40 suns	32 suns
Percentage of energy within the uniformly illuminated area (38 mm × 38 mm)	57.4 %	56.3 %	52.5 %	46.4 %	40.2 %	34.4%
Percentage of energy within the receiver area of (50 × 50) mm	87.2 %	83.9 %	76.7 %	69.6 %	63.2 %	56.9 %
Spillage loss at (50 mm × 50 mm) receiver area	11.8 %	14.4%	19.4 %	23.1 %	26.3 %	29.8 %

To analyze the performance of the two-stage reflective NISC active daylighting system, experimental and theoretical results of indoor illuminance are compared as shown in Figure 4.6. The formula used to calculate the theoretical result of the indoor illuminance ($Illum_{theo}$) produced by the prototype is:

$$\mathrm{Illum}_{\mathrm{theo}} = ((C_{avg} - 1)R_{\mathrm{facet}}^{2} + 1) \times \mathbf{I} \times \%VL \times (1 - L_{\mathrm{fiber}}) \times T_{\mathrm{hot\,mirror}} \times E_{\mathrm{L}} \times \frac{A_{\mathrm{fiber}}}{\mathrm{A}_{\mathrm{illum}}} \times N_{\mathrm{fiber}} \quad (4.6)$$

The full meaning of the abbreviated parameters in equation 4.6 are shown in Table 4.9.

Table 4.9: Full meaning of the abbreviated parameters used in equation 4.6.

C_{avg}	Average solar concentration ratio (76 suns in the uniform illumination area)
I	Direct normal irradiance (W/m^2)
A_{fiber}	The cross-sectional area of the core of the plastic optical fiber ($\pi \times 1.4725^2$) mm^2
$\%VL$	The percentage of visible light in the solar spectrum (47%)
$T_{\mathrm{hot\ mirror}}$	The transmissivity of hot mirror to visible light (98%)
L_{fiber}	The total transmission loss for a 10 m long plastic optical fiber (45.7%)
N_{fiber}	The number of plastic optical fibers (14 fibers)
E_{L}	The average value of direct beam luminous efficacy (104 lm/W)
A_{illum}	The indoor illumination area (1.586 m^2)
R_{facet}	The reflectivity of primary/secondary facet mirrors (93.5 %).

The detailed theoretical calculation of the indoor illuminance from the POF, using data from Table 4.7 measured at 14:05 h and maximum mirror reflectivity of 94 % as stated by the manufacturer is illustrated below:

$$\text{Illum}_{\text{theo}} = ((76-1)(0.94^2)+1)\times(\mathbf{900}\times\mathbf{10^6}\ \text{W/mm}^2)\times 0.47\times(1-0.457)\times 0.98\times 104\text{lm/W}\times \frac{(\pi\times 1.4725^2)\text{mm}^2}{1.586\ \text{m}^2}\times 14 \quad (4.7)$$

$$\text{Illum}_{\text{theo}} = 94.7\text{lm/m}^2 = 94.7\text{lux} \quad (4.8)$$

At 14:05 h on 16th February 2017, the maximum indoor illuminance that can be obtained inside the 1.586 m^2 test room from the fourteen 10 m long optical fibers connected to the two-stage NISC when the mirror reflectivity is maximum is 94.7 lux. With a mirror reflectivity of 93.5 %, the theoretical indoor illuminance was calculated as 93.7 lux ≈ 94 lux.

Since the indoor illuminance was measured 2 m away from the exit aperture of the POFs, the indoor illumination area (A_{illum}) in equation (4.6) was determined by perceiving that the light meter is placed at a distance of 2 m away from the exit aperture of the fibers in the test room. From Figure 4.7, the indoor illumination area was computed since the half rim angle (ω) of the solar concentrator is known. The half-rim angle (ω) of the prototype two-stage reflective NISC active daylighting system was calculated as $\tan^{-1}\frac{31.1}{70} = 24°$, which is also equivalent to the maximum incident angle of sunrays relative to the entrance aperture of the POF. Thus, the maximum exit angle of sunrays is also 24º and the indoor illumination area at a distance of 2 m from the exit aperture of POF can be attained as ($c \times c$) m^2, where $c = \frac{2\tan 24}{\cos 45} = 1.2593$ m. Hence, the indoor illumination area = (1.2593 ×1.2593) = 1.586 m^2.

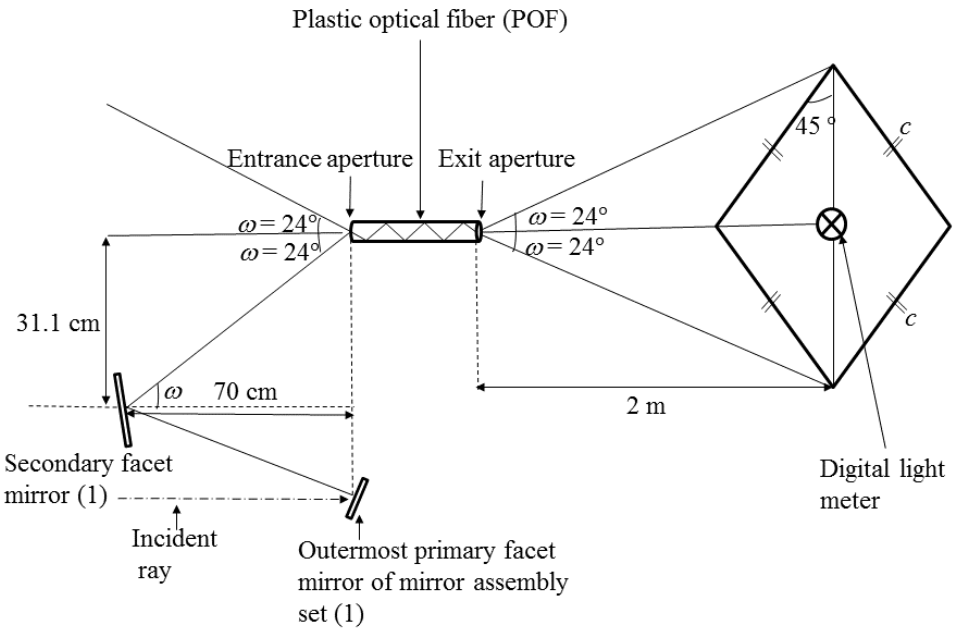

Figure 4.7: Schematic diagram illustrating how the half rim angle and indoor illumination area were calculated

CHAPTER 5

COST ANALYSIS AND COST COMPARISON

5.1 Cost analysis of two-stage reflective non-imaging solar concentrator (NISC).

The prototype two-stage reflective NISC with a total collective area of 0.20 m^2 is not a final commercial product. This means that the hardware design and cost of manufacturing are not fully optimized. For this reason, the optimized collective area of the two-stage reflective NISC is proposed as 4 m^2 for economic analysis to be carried out in order to levelize the cost of the sun-tracking system and the mechanical structure. This implies that the total reflective area of the primary reflector is 4 m^2 and total reflective area of the secondary reflector is 2.56 m^2. Based on previous experience, 4 m^2 collective area is the most practicable size for a roof-top solar concentrator after considering several factors of practical implementation wherein the height of the solar concentrator is about 2 m and the total weight of the flat mirrors with 3 mm thickness and mechanical support structure is about 51 kg (Chong *et al*., 2017). The total cost of the flat facet mirrors with a total reflective area of 6.56 m^2, is only USD 131.20 based on the standard quoted price for a 3 mm thick solar grade flat mirror at the price of USD 20/m^2. Whereas, in two daylighting systems designed by Ullah and Shin (2014), the costs of parabolic trough and linear Fresnel lens are USD 400/m^2 and USD 200/m^2 respectively. The cost of the commercially available automatic sun-tracking module is USD 700 (Vu *et*

al., 2016). The estimated breakdown cost of the two-stage reflective NISC with a total collective area of 4 m^2 is listed in Table 5.1, with a total cost of USD 1231.20.

Table 5.1: Estimated breakdown cost for constructing an optical fiber based two-stage reflective non-imaging solar concentrator (NISC) with a collective area of 4 m^2.

	USD
Mechanical support structure	200.00
Flat facet mirrors	131.20
Adjustable frames with screws	100.00
Automatic sun-tracking module	700.00
Base structure and miscellaneous	100.00
Total cost	1231.20

From the prototype design, the total collective area of 0.2 m^2 can produce an equivalent electrical power of 36.35 W. Proportionally, the total collective area of 4 m^2 can provide indoor illuminance equivalent to the electrical power of (4 × 36.35) / 0.2 = 727 W, which is equivalent to USD 1.69/W (= USD 1231.20 / 727 W).

To evaluate the economic viability of the two-stage reflective NISC, the payback period of the active daylighting system can be determined using the following formulas (Goswami *et al*., 1999):

$$n_{\text{pay}} = -\frac{\ln[1 - S_{\text{total}} i' / P_{\text{ann}}]}{\ln(1 + i')} \tag{5.1}$$

$$\text{in which } i' = \left(\frac{1+i}{1+j}\right) - 1 \tag{5.2}$$

where i is the interest rate or discounted rate, j is the fuel inflation rate, S_{total} is the total capital cost of the active daylighting system, P_{ann} is the annual energy cost saving (USD/year). Considering a discounted form of calculation with the interest rate of 4 % if a loan is taken to build the active daylighting system with a capacity equivalent to generating 727 W of electricity for illuminating a building and the fuel inflation rate is 2 %. Assuming the annual average of daily direct normal irradiation is 6 kWh/m^2, the annual electrical energy saving by the active daylighting system to illuminate the building can be calculated as 0.727 kW × 6 h/day × 365 days = 1592.13 kWh. At the electricity rate of USD 0.13 per kWh, 1592.13 kWh is equivalent to the annual consumption of USD 207 in the electricity bill. The estimated total cost of constructing the 4 m^2 prototype is USD 1231.20. Using annual saving from the electricity bill to pay for the loan in installments, the total payback period can be calculated from Equation (5.1) as 6.4 years, which is quite realistic as the daylighting system can last for at least 15 years. On the other hand, for undiscounted form inclusive of the fuel inflation rate at 2 %, the total payback period is calculated as 5.6 years This confirms that the active daylighting system using two-stage reflective NISC has a cost-effective potential if it can be produced commercially with an upgraded mechanical design and light transmission system as compared to other existing fiber optics daylighting systems. The price of the plastic optical fiber varies with its length and 10 m length was only used for the experiment to

measure indoor illuminance. Studies have revealed that the shorter the length of the optical fiber, the more the transmittance and the lesser the losses. So, for real-world implementation of the optical fiber based two-stage reflective NISC daylighting system, a range of 2 m to 6 m optical fiber length would be recommended to transmit daylight from the solar concentrator on the rooftop to the interior parts of a building (Ullah and Shin, 2014).

To assess the reliability of the new daylighting system design, the prototype has been operated and tested on the rooftop for one year. The system performance has shown its robustness and stability. The solar grade flat facet mirrors particularly designed for outdoor operations are long-lasting and the mirror reflectivity can be retained well after one year of operation. The adjustable frame, screws and compression springs used to hold the mirrors in their aligned positions are firm and maintain their fixed positions after one year. The mechanical driving devices such as the stepper motor, sprocket gear, custom-made gear for azimuth motion and the linear actuator for elevation motion are very durable and reliable. The control system for sun-tracking has been performing as programmed and there has been no cases of failure.

5.2 Cost comparison of the new active daylighting system with other optical fiber based existing daylighting systems

Table 5.2 presents a cost comparison of the novel fiber optics two-stage reflective NISC active daylighting system with some selected existing fiber

optics daylighting systems in terms of the cost of the collector, the cost of sun-tracking module and the prorated total system cost for 4 m^2 collector.

Table 5.2: Comparison between the proposed active daylighting system using two-stage reflective non-imaging solar concentrator (NISC) and other existing daylighting systems

	Active fiber optics daylighting systems	Collector specification	Cost			
			Collector	Sun-tracking module	Total system cost based on collector specification	Prorated total system cost at 4m^2 collective area
1	Novel two-stage reflective NISC	Total reflective area of the primary reflector = 4 m^2 Total reflective area of the secondary reflector = 2.56 m^2. Half rim angle of concentrator = 24º	For 4 m^2 collector, flat facet mirrors cost USD 131.20	USD 700	USD 1231.20	USD 1231.20
2	Parabolic trough + parabolic reflector + trough CPC (Ullah and Shin, 2014)	Input aperture area of parabolic trough = 1000 mm (H) × 570 mm (W) Focal length of parabolic trough = 450 mm Input aperture area of secondary parabolic reflector = 15 mm × 570 mm Focal length of parabolic reflector = 456.7 mm Input aperture area of Trough CPC = 15 mm ×570 mm	Parabolic trough costs USD 400/m^2	USD 400	> USD 800/m^2	> USD 3200
3	Linear Fresnel lens + Collimating lens (plano-concave lens) + Trough CPC (Ullah and Shin, 2014)	Input aperture area of Fresnel lens = 1000 mm (W) × 570 mm (L) Focal length of Fresnel lens = 775 mm Input aperture area of plano-concave lens = 15 mm × 570 mm	Linear Fresnel lens cost USD 200/m^2.	USD 400	> USD 600/m^2	> USD 2400

		Focal length of plano-concave lens = 23.27 mm Input aperture area of Trough CPC = 15 mm × 570 mm				
4	Hybrid parabolic two-stage daylighting system (Sapia, 2013)	Diameter of parabolic collector = 2.6 m Total collective area = 4.48 m^2 Parabolic collector efficiency = 95 % Diameter of secondary collector = 1.03 m	2.6 m diameter parabolic primary concentrator costs 250 euros (or USD 267.5 at the rate of 1 euro = 1.07 USD). Secondary optical element costs 380 euros (or USD 406.6 at the rate of 1 euro = 1.07 USD).	USD 749 euros (or USD 801.43 at the rate of 1 euro = 1.07 USD).	6538 euros (or USD 6995.66 at the rate of 1 euro = 1.07 USD).	USD 6246.13
5	Modified optical fiber daylighting system with sunlight transportation in free space (Vu *et al*., 2016)	Diameter of Fresnel lens = 340 mm Focal length of Fresnel lens = 350 mm Collimator specification: Diameter of parabolic mirror = 50 mm with focal length of 4 mm; diameter of convex lens = 15 mm with focal length of 11 mm, thickness of concentrating module = 350 mm Distance between Fresnel lens and receiver = 3 mm	5 × 5 arrays of Fresnel lens cost (USD 40/lens) = USD 720 18 collimators cost = USD 540 Total cost of 36 mirrors = USD 72 18 extended hot mirrors cost = USD 990 Mechanical brackets cost = USD 1000 18 POFs with 1 m length cost = USD 70.20 18 distributers cost = USD 180	USD 700	USD 4272	USD 7527
6	Optical fiber based daylighting system using modified compound parabolic concentrator (M-CPC) (Vu and Shin, 2016)	Concentrator size = 540 mm (L) × 270 mm (W) × 212.34 mm (H). For a concentrator ratio of 100 suns: Length of primary CPC = 200 mm Length of secondary (collimated) CPC = 2.47 mm Total M-CPC length = 202.47 mm	200 M-CPCs cost USD 1000	USD 400	Total cost with a collective area of 0.063 m^2 = USD 2050	USD 130,158.7

	Input angle of M-CPC = 3˚
	Output angle = 31˚
	Focal diameter = 1.05 mm

Note: Refer to the Literature review of this thesis (section 2) and Chong *et al*., (2017) for more details on the active fiber optics daylighting systems listed in Table 5.2.

From the last column showing the "prorated total system cost at 4 m^2 collective area" in Table 5.2, the two-stage reflective NISC daylighting system can be identified as the most cost-effective system among all the active daylighting systems with the lowest total system cost of USD 1231.20 at a collective area of 4 m^2. For practical implementation, the active daylighting system using two-stage reflective NISC would be installed on the rooftop. For daylight transmission of the concentrated sunlight to different rooms in the building, plastic optical fibers would be used. The total space area of the building needed to be illuminated determines the total collective area of the two-stage reflective NISC. Hybrid lighting system is recommended such that the exit apertures of the plastic optical fibers and the LEDs are situated in an alternating arrangement to form a 2-D array and then enclosed with diffusers to provide uniform indoor illumination. The illumination level of the LEDs would be adjusted to compensate the fall of daylight from the required illuminance standard while maintaining constant illuminance at all times. An electrical lighting control system with a photosensor would be used to maintain the standard illuminance level of the interior through a closed loop feedback system. An attenuator would also be connected to the control system so that the light level from the optical fibers can be adjusted. The recommended length of plastic

optical fiber for good transmittance is about 6 m in which a 3 m long fiber gives a transmittance of 87 % and an 8 m long fiber gives a transmittance of 72 % (Ullah and Shin, 2014). To optimize the transmission loss in the fibers, the two-stage reflective NISC should be placed on the rooftop of a building with a maximum height of not more than two storeys so that the plastic optical fibers with a maximum length of 6 m can reach every corner of the interior space of the building. Nevertheless, a much longer fiber length is probable if low loss fused silica optical fiber can be manufactured at an affordable price.

CHAPTER 6

CONCLUSION AND FUTURE WORK

6.1 Conclusion

An active optical fiber-based daylighting system using two-stage reflective NISC has been successfully designed, constructed and evaluated. The advantages of this system include:

- simple optical design,
- low rim angle of 24 ˚ which is important for effective collimation of daylight towards the desired area having optical fibers with a half acceptance angle of 30 ˚,
- cost effective design compared to some existing designs
- less sensitive to pointing error of its sun-tracking system as proven in section 4.3.4 compared to a parabolic dish or Fresnel lens.
- capable of concentrating sunlight uniformly to the receiver area, which is highly required for solar daylighting systems.

The prototype two-stage reflective NISC daylighting system with a total collective area of 0.2 m^2 can provide an average illuminance of 500 lx (3780 lm) to a 7.56 m^2 room area via 314 plastic optical fibers when direct normal irradiance is 1000 W/m^2. This indoor illuminance is equivalent to 33

LEDs with rated electrical power of 36.35 W. The power conversion efficiency of the prototype is 21.4 % based on the input solar power of 170 W at the target area. On-site experimental data was used to validate the results obtained from the numerical analysis and both results displayed a satisfactory agreement. From the numerical simulation, the average solar concentration ratio at the uniformly illuminated area of the prototype was obtained as 76 suns. Also, from the experiment performed on the 14th December 2017, the average measured solar concentration ratio was obtained as 66.6 suns with a standard deviation of 3.0 suns. From this result, the reflectivity of the facet mirror was calculated as 93.5 %, which is reasonable as it falls in the reflectivity range specified by the mirror manufacturer. A deviation was observed between the experimental and theoretical results of indoor illuminance caused by both systematic error (due to pointing error of the sun-tracking system) and random error (due to measurement error of the light meter). However, the spillage loss analysis result (Table 4.8) presented in section 4.3.4 has revealed that the transmission loss produced by low tracking accuracy is still within the acceptable range.

Cost analysis and cost comparison on the two-stage reflective NISC has been done for an optimized collective area of 4 m^2. The total estimated cost of the system is USD 1231.20 which was justified as the most cost-effective amongst other selected existing fiber optics daylighting system compared with. Assuming a loan was taken at the interest rate of 4 % and fuel inflation rate of 2 % to build 4 m^2 two-stage reflective NISC, the annual savings of USD 207 from the electricity bill can be used to pay back the loan in 6.4 years. This is

realistic because the active daylighting system is projected to have a lifespan of about 15 years. In conclusion, this novel two-stage reflective non-imaging solar concentrator has a great potential for commercial application towards energy saving, while curbing the identified problems in some existing fiber optics daylighting systems.

6.2 Future works

The current study focused on designing, constructing and analyzing a two-stage reflective NISC. Experimental analysis on the uniformity of sunlight on the receiver was considered but the analysis on the uniformity of the indoor illuminance was not considered due to the limitations of measurement facilities. To improve the illuminance of the daylighting system, this analysis should be conducted in the future.

During data collection for the solar concentration ratio of the two-stage reflective NISC, a CPV cell was placed at the central region of the receiver area to measure the short-circuit current. Sometimes, the CPV cell became very hot due to high solar concentration and at that point in time, no readings could be taken as they may not be accurate. A cooling fan was then fixed close to the CPV cell as illustrated in Figure 4.1. This helped to reduce the temperature of the CPV cell but only for a short period of time. Therefore, a better cooling solution for the CPV cell should be considered when carrying out such experiments in the future to get more accurate data. Also, multimeters and light meters with better accuracy should be used for future experiments.

Numerical analysis and experiments using other shapes and sizes of plastic optical fibers and other daylight transmission techniques should be performed on the two-stage reflective NISC to further optimize its design.

REFERENCES

Al-Mofleh, A,. Taib, S., Mujeebu, M. and Salah, W., 2009. Analysis of sectoral energy conservation in Malaysia. *Energy*, 34, pp.733–739.

Alrubaih, M.S., Zain, M.F.M., Alghoul, M.A., Ibrahim, N.L.N., Shameri, M.A. and Elayeb, O., 2013. Research and development on aspects of daylighting fundamentals. *Renewable and Sustainable Energy Reviews*, 21, pp. 494 – 505. doi: 10.1016/j.rser.2012.12.057.

ASGH Mirror Workshop, 2012. *The Cassegrain Project* [Online]. Available at: http://mirrorworkshop.mtbparker.com/cassegrainStory.html [Accessed 10 March 2016].

Berardi, U., 2015. The development of a monolithic aerogel glazed window for an energy retrofitting project. *Applied Energy*, 154, pp. 603 – 615.

(CIBSE) Code for interior lighting, 1994. Chartered Institution of Building Service Engineers, London, UK.

Chong, K.K., Siaw, F.L., Wong, C.W. and Wong, G.S., 2009. Design and construction of non-imaging planar concentrator for concentrator photovoltaic system. *Renewable Energy*, 34, pp. 1364 – 1370.

Chong, K.K., Wong, C.W., Siaw, F.L, and Yew, T.K., 2010. Solar flux distribution analysis of non-imaging planar concentrator for the application in concentrator photovoltaic system. *Photovoltaic Specialists Conference*, 20 - 25 June 2010 Honolulu, USA. Honolulu: IEEE, pp. 3013 – 3018.

Chong, K.K., Chay, K.G. and Chin, KH., 2012. Study of a solar water heater using stationary V-trough collector. *Renewable Energy*, 39, pp. 207 - 215.

Chong, K.K., Wong, C.W., Yew, T.K. and Tan, M.H., 2013. Solar concentrator assembly. U*S patent, application no: 13/901,519 (pending)*, filed on 23 May 2013.

Chong, K.K., Onubogu, N.O., Yew, T.K., Wong, C. and Tan, W., 2017. Design and construction of active daylighting system using two-stage non-imaging solar concentrator. *Applied Energy* – 2017 (In Press). https://doi.org/10.1016/j.apenergy.2017.05.188

Chong, K.K., Wong, C.W., Yew, T.K. and Tan, M.H., 2014. Dense-array concentrator photovoltaic system utilizing non-imaging dish concentrator and

array of crossed compound parabolic concentrators. *US Patent, Application no: 14/462,891 (pending),* filed on 19 August 2014.

Chow, S.K.H., Li, D.H.W., Lee, E.W.M. and Lam, J.C., 2013. Analysis and prediction of daylighting and energy performance in atrium spaces using daylight-linked lighting controls. *Applied Energy*, 112, pp. 1016 – 1024.

EIA (U.S. Energy Information Administration), 2017. *Independent statistics and analysis: How much electricity is used for lighting in the United States* [online]. Available at: https://www.eia.gov/tools/faqs/faq.php?id=99&t=3 [Accessed 2 May 2017].

Elmualim, A.A, Smith, S., Riffat, S.B. and Shao, L., 1999. Evaluation of dichroic material for enhancing light pipe/ natural ventilation and daylighting in an integrated system. *Applied Energy*, 62, pp. 253 - 266.

Energy Rating, 2016. [Online]. Available at: http:///www.energyrating.gov.au/products/lighting [Accessed 7 July, 2017].

Feuermann, D., Gordon, J.M. and Huleihil, M., 2002. Solar fiber-optic mini-dish concentrators: First experimental results and field experience. *Solar Energy*, 72, pp. 459 – 472.

Galasiu, A.D., Atif, M.R. and MacDonald, R.A., 2004. Impact of window blinds on daylight-linked dimming and automatic on/off lighting controls. *Solar Energy*, 76, pp. 523 - 544.

Ghisi, E. and Tinker, J.A., 2006. Evaluating the potential for energy savings on lighting by integrating fiber optics in buildings. *Building and Environment*, 41(12), pp. 1611 - 1621.

Gilmore, V.E., 1988. *Sun flower over Tokyo*. In Popular Science; Winter Park, FL, USA: Bonnier Corporation.

Golden DRAGON plus Datasheet Version 1.1, LUW W5AM.*OSRAM Opto Semiconductors GmbH* 2015.

Goswami, D.Y., Kreith, F. and Kreider, J.F., 1999. *Principles of solar energy engineering*. 2nd ed. Philadelphia, PA: Taylor & Francis.

Hetcht, E., 2002. *Optics*. 4th ed. San Francisco: Addison Wesley.

https://suntomoon.files.wordpress.com/2012/01/img_1626.jpg [Accessed 25 June 2016].

Huang, T., Hocheng, H., Chou, T. and Yang, W., 2013. Bring free light to buildings: overview of daylighting system. In: Mendez-Vilas A, editor.

Materials and Processes for energy: communicating current research and technological developments. Spain: Formatex Research Centre, pp. 639 – 648.

Instruction manual for MASTECH Digital Light Meter MS6612.

International Energy Agency (IEA), 2011. *25 Energy Policy Recommendations,* France.

Jenkins, D. and Newborough, M., 2007. An approach for estimating the carbon emissions associated with office lighting with a daylight contribution. *Applied Energy*, 84, pp. 602 – 622.

Kim, W., Jeon, Y. and Kim, Y., 2016. Simulation-based optimization of an integrated daylighting and HVAC system using the design of experiments method. *Applied Energy*, 162, pp. 666 – 674.

Kubba, S., 2012. *Handbook of Green Building Design, and Construction, LEED, BREEAM, and Globes*. United Kingdom: Elsevier (Butterworth-Heinemann).

Lim, Y. and Ahmad, M.H., 2013. Daylighting as a sustainable approach for high-rise office in tropics. *International Journal of Real Estate Studies*, 8(1) pp. 31 – 42.

Lingfors, D. and Volotinen, T., 2013. Illumination performance and energy saving of a solar fiber optic lighting system. *Optics Express*, 21(S4), pp. 642 - 655. doi: 10.1364/OE.21.00A642.

Ma, X., et al., 2014. An optimum structure design for Cassegrain optical system. *Optik*, 125(3), pp. 1423 – 1426.

Martirano, L.A., 2011. Smart lighting control to save energy. *In Proceedings of the 2011 IEEE 6th International Conference on Intelligent Data Acquisition and Advanced Computing Systems (IDAACS)*, 15 – 17 September 2011 Prague, Czech Republic, pp. 132–138.

Muhammad-Sukki, F., Ramirez-Iniguez, R., McMeekin S.G., Stewart B.G. and Clive B., 2010. Solar concentrators. *International Journal of Applied Sciences (IJAS)*, 1(1).

Muhs, J., 2000. Design and analysis of hybrid solar Lighting and full-spectrum solar energy systems, *SOLAR 2000 Conference*, 16 - 21 July 2000, Madison, Wisconsin: Paper no. 33., pp. 0 – 9.

Obianuju, O.N and Chong, K.K., 2017. High acceptance angle optical fiber based daylighting system using two-stage reflective non-imaging dish concentrator. *Energy Procedia*, 105, pp. 498 – 504.

Omer, A.M., 2008. Green energies and the environment, *Renewable and Sustainable Energy Reviews*, 12(7), pp. 1789 – 1821. doi: 10.1016/j.rser.2006.05.009.

Pohl, W. and Anselm, C., 2001. *Report of EC-funded Joule-Craft Research Project: Development of an economic and energy saving heliostat technology for room illumination, Publishable final report*, Contract No. JOR3-CT98-7042, Aldrans, Austria: Bartenbach LichtLabor GmbH.

Sapia, C., 2013. Daylighting in buildings: Developments of sunlight addressing by optical fiber. *Solar Energy*, 89, pp. 113 – 121. doi: 10.1016/j.solener.2012.12.003.

Schlegel, G.O. et al., 2004. Analysis of a full spectrum hybrid lighting system. *Solar Energy*, 76(4), pp. 359 – 368. doi: 10.1016/j.solener.2003.11.005.

Sharp, F., Lindsey. D., Dols, J. and Coker, J., 2014. The use and environmental impact of daylighting. *Journal of Cleaner Production*, 85, pp. 462 - 471.

Shen, X. et al., 2009. Analysis of a hybrid cost-effective solar lighting system. *SPIE 7423: Proceedings of Nonimaging Optics: Efficient Design for illumination and Solar Concentration VI*, doi:10.1117/12.826547.

Shulman, S. *et al.,* 2012. *Cooler Smarter: Practical Steps for Low-Carbon*

Living: Expert Advice From the Union of Concerned Scientists, United States: Island Press.

Siaw, F.L., Chong, K.K. and Wong, C.W., 2014. A comprehensive study of dense-array concentrator photovoltaic system using non-imaging planar concentrator. *Renewable Energy*, 62, pp. 542– 555.

Song, J., Zhu, Y., Jin, Z. and Yang, Y., 2014. Daylighting system via fibers based on two-stage sun-tracking model. *Solar Energy*, 108, pp. 331 – 339. doi: 10.1016/j.solener.2014.07.021.

Tan, M.H., Chong, K.K. and Wong, C.W., 2014. Optical characterization of non-imaging dish concentrator for the application of dense-array concentrator photovoltaic system. *Applied Optics*, 53, pp. 475 – 486.

Tan, M.H and Chong K.K., 2016. Influence of self-weight on electrical power conversion of dense-array concentrator photovoltaic system. *Renewable Energy*, 87, pp. 445 - 457. doi:10.1016/j.renene.2015.10.022.

TERI, 2014. The Energy and Resources Institute. *Regional report on the transition to efficient lighting in South Asia*. New Delhi.

Ullah, I. and Shin, S., 2012. Development of optical fiber-based daylighting system with uniform illumination. *Journal of Optical Society of Korea*, 16, pp. 247 – 255. doi:10.3807/JOSK.2012.16.3.247.

Ullah, I. and Shin, S., 2013a. Uniformly illuminated efficient daylighting system. *Smart Grid and Renewable Energy*, 4(2), pp. 161 – 166. doi: 10.4236/sgre.2013.42020.

Ullah, I. and Shin, S., 2013b. Concept of solar tower for daylighting in multi-floor buildings, *Journal of Green Science and Technology*, 1, pp. 1 – 6. doi:10.1166/jgst.2013.1016.

Ullah, I. and Shin, S., 2014. Highly concentrated optical fiber-based daylighting systems for multi-floor office buildings. *Energy and Buildings*, 72, pp. 246 – 261. doi: 10.1016/j.enbuild.2013.12.031.

Ullah, I. and Whang, A.J., 2015. Development of optical fiber-based daylighting system and its comparison. *Energies*, *8*, pp. 7185 - 7201; doi:10.3390/en8077185.

User manual for GW INSTEK GDM-394/396.

U.S. Green Building Council, 1995, *Green Building Rating Systems - Draft Recommendations for a U.S. Rating System*. Bethesda, Md.

Vu, N.H. and Shin, S., 2016. Cost-effective optical fiber daylighting system using modified compound parabolic concentrators. *Solar Energy*, 136, pp. 145–152. doi: 10.1016/j.solener.2016.06.064.

Vu, N-H., Pham, T-T. and Shin, S., 2016. Modified optical fiber daylighting system with sunlight transportation in free space. *Optics Express*, 24 (26), doi: 10.1364/OE.24.0A1528.

Yew, T.K., Chong, K.K. and Lim, B.H., 2015. Performance study of crossed compound parabolic concentrator as secondary optics in non-imaging dish concentrator for the application of dense-array concentrator photovoltaic system. *Solar Energy*, 120, pp. 296 – 309.

Yu, J., Liu, Y., Xiong, C. and Huang, J.C., 2015. Study on daylighting and energy conservation design of transparent envelope for office building in hot summer andcold winter zone. *Procedia Engineering*, 121, pp. 1642 – 1649. doi: 10.1016/j.proeng.2015.09.108.

Zafrullah, J., 2013. *Tracking solar concentrators*. London: Springer, Heidelberg.

Zain-Ahmed, A., Sopian, K., Othman, M., Sayigh, A. and Surendran, P., 2002. Daylighting as a passive solar design strategy in tropical buildings: a case study of Malaysia. *Energy Conversion Management*, 43, pp. 1725 - 1736.

PUBLICATIONS

Based on findings from this research, two papers have been published – one in Energy Procedia (conference paper) and another in Applied Energy Journal (Journal paper). Other papers are still in preparation for submission to other Journals. The full published papers are seen at the appendix (E and F).

[1] Obianuju, O.N and Chong, K.K., 2017. High acceptance angle optical fiber based daylighting system using two-stage reflective non-imaging dish concentrator. *Energy Procedia*, 105, pp. 498 – 504.

[2] Chong, K.K., Onubogu, N.O., Yew, T.K., Wong, C. and Tan, W., 2017. Design and construction of active daylighting system using two-stage non-imaging solar concentrator. *Applied Energy* – 2017 (In Press). https://doi.org/10.1016/j.apenergy.2017.05.188

*Note: Data and some figures in the above papers have been repeated in this thesis as the publications are from the same research described in this thesis and both papers are written by the author of this thesis.

APPENDIX A

ESKA PLASTIC OPTICAL FIBER: CK120

ESKA™ Plastic Optical Fiber: CK120

Manufactured by Mitsubishi Rayon Co., Ltd.

Marketed and sold by Mitsubishi International Corporation

January 2010

Structure		
Core Material	Polymethyl Methacrylate Resin (PMMA)	
Cladding Material	Fluorinated Polymer	
Core Refractive Index	1.49	
Refractive Index Profile	Step Index	
Numerical Aperture	0.5	
	Unit	Typical
Core Diameter	µm	2,945
Overall Diameter	µm	3,000
Approximate Weight (g/m)	8.6	

Packaging	
Spool Length (m)	150
Net weight on spool (kg)	1.3
Coil Weight (kg)	-
Carton Size (mm)	405 X 410 X 75
Carton Weight (kg)	1.6
Master Carton	10 coils

Performance		Criteria for Acceptance and/or [Test Conditions]	Unit	Values
Storage and Operation Temperature		No deterioration in optical properties [in a dry atmosphere] *	°C	-55 ~ 70
Operating Temperature in a Moist Atmosphere		No deterioration in optical properties [under 95% RH] **	°C	Max.60
Optical Properties	Transmission Loss [650nm Collimated Light]	[Standard Condition] [10m-1m cutback]	dB/km	Max.200
Mechanical Character-istics	Minimum Bend Radius	Loss increment =< 0.5dB [quarter bend]	mm	Min.100
	Tensile Strength	Tensile force at yield point [JIS C 6861]	N	Min.550

Notes: Performance tested in conditions under 25°C unless otherwise indicated
* Attenuation increase shall be <10% after 1,000 hours
** Attenuation increase shall be <10% after 1,000 hours, except when due to absorbed water

CK120-C Cut Bristles

Straight, one-meter long fibers with no memory curve, manufactured in the U.S. using ESKA™

Diameter(µm)	Length (mm)	Number bristles per pack
500	1,000	300 +0/-3%

Applications: Lighting

CK grade fibers are typically used for lighting environments and illuminating applications.

Product Testing

The CK-Series of fibers is a tested and qualified, but has unspecified tolerances and typical values. The information contained in this document should, therefore, only be used as a guide.

The information contained herein is presented as a guide to product selection. It is subject to change without notice, and should not be regarded as a representation, warranty or guarantee with regard to the quality, characteristics or use of this product

Mitsubishi International Corporation 655 Third Avenue New York, NY 10017

Please visit http://www.fiberopticpof.com/ to locate a sales representative near you.

APPENDIX B

ORIENTAL MOTOR

Orientalmotor

HM-40093-3

OPERATING MANUAL

Closed loop stepping motor and driver package

αSTEP AR Series CE

DC power input Pulse input type Driver

Thank you for purchasing an Oriental Motor product.
This Operating Manual describes product handling procedures and safety precautions.
• Please read it thoroughly to ensure safe operation.
• Always keep the manual where it is readily available.

Operating Manuals for the AR Series

Manual name	Motor function	Driver function	Installing the motor	Installing the driver	Connection	Operation	Troubleshooting
AR Series Motor OPERATING MANUAL (Supplied with motor)	○	–	○	–	–	–	–
AR Series DC power input Pulse input type Driver OPERATING MANUAL (this document)	–	○	–	○	○	–	–
AR Series DC power input Pulse input type USER MANUAL	○	○	○	○	○	○	○

The "USER MANUAL" does not come with the product. For details, contact your nearest Oriental Motor sales office or download from Oriental Motor website download page.

Introduction

■Before use

Only qualified personnel should work with the product.
Use the product correctly after thoroughly reading the section "Safety precautions."
The product described in this manual has been designed and manufactured for use in general industrial equipment. Do not use for any other purpose. Oriental Motor Co., Ltd. is not responsible for any damage caused through failure to observe this warning.

■Hazardous substances

The products do not contain the substances exceeding the restriction values of RoHS Directive (2011/65/EU).

■Checking the product

Verify that the items listed below are included. Report any missing or damaged items to the branch or sales office from which you purchased the product.

- Driver.....1 unit
- CN1 connector (3 pins).....1 pc.
- CN5 connector (36 pins).....1 pc.
- OPERATING MANUAL Driver (this document).....1 copy

Names of parts

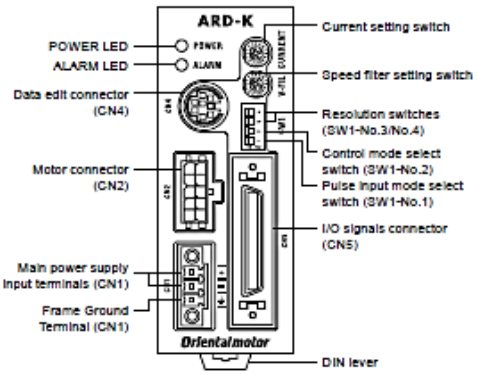

Installation

■Location for installation

The driver has been designed and manufactured to be installed within another device. Install them in a well-ventilated location that provides easy access for inspection. The location must also satisfy the following conditions:

- Inside an enclosure that is installed indoors (provide vent holes)
- Operating ambient temperature 0 to +50 °C [+32 to +122 °F] (non-freezing)
- Operating ambient humidity 85% or less (non-condensing)
- Area that is free of explosive atmosphere or toxic gas (such as sulfuric gas) or liquid
- Area not exposed to direct sun
- Area free of excessive amount of dust, iron particles or the like
- Area not subject to splashing water (rain, water droplets), oil (oil droplets) or other liquids
- Area free of excessive salt
- Area not subject to continuous vibration or excessive shocks
- Area free of excessive electromagnetic noise (from welders, power machinery, etc.)
- Area free of radioactive materials, magnetic fields or vacuum
- 1000 m (3300 ft.) or lower above sea level

■Installation method

Mount the driver to a 35 mm (1.38 in.) width DIN rail.

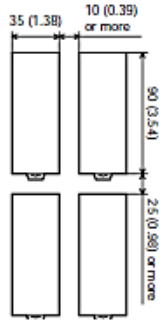

[Unit: mm (in.)]

■Note

- Install the driver in an enclosure whose pollution degree is 2 or better environment, or whose degree of protection is IP54 minimum.
- Do not install any equipment that generates a large amount of heat or noise near the driver.
- Do not install the driver underneath the controller or other equipment vulnerable to heat.
- Check ventilation if the ambient temperature of the driver exceeds 50 °C (122 °F).
- Be sure to install the driver vertically (vertical position).

Connection

The following figure is a connection example when an electromagnetic brake motor is used.

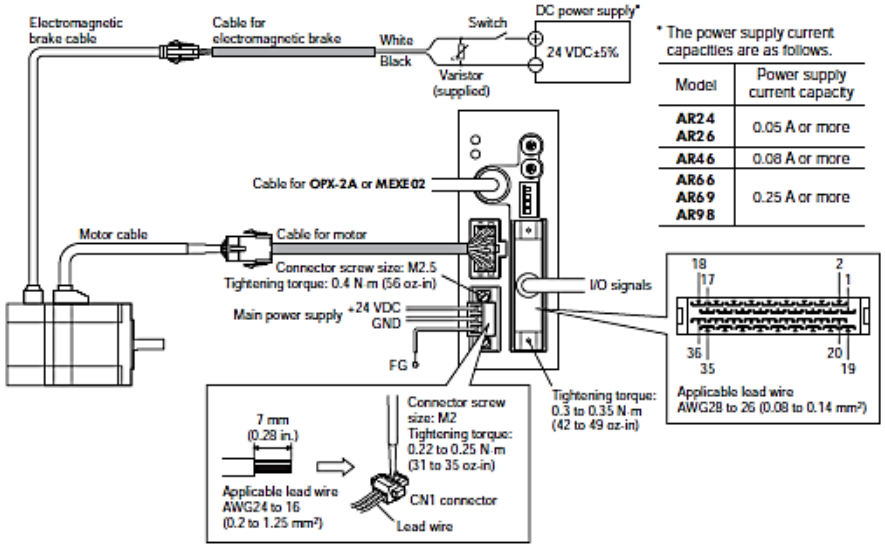

* The power supply current capacities are as follows.

Model	Power supply current capacity
AR24 **AR26**	0.05 A or more
AR46	0.08 A or more
AR66 **AR69** **AR98**	0.25 A or more

■Main power supply current capacity

Model	Input power supply voltage	Power supply current capacity
AR14	24 VDC±10%	0.4 A or more
AR15		0.5 A or more
AR24 AR26		0.9 A or more
AR46	24 VDC±10% 48 VDC±5%	1.4 A or more
AR66		3.1 A or more
AR69		3.0 A or more
AR98		2.5 A or more

■Notes about connection

●General

- Have the connector plugged in securely. Insecure connector connection may cause malfunction or damage to the motor or driver.
- When cycle the power or plugging/unplugging the connector, turn off the power and wait for the POWER LED to turn off.

●Connecting the motor

- When unplugging the connector, do so while pressing the latches on the connector.
- When installing the motor to a moving part, use an accessory flexible cable offering excellent flexibility.
- If the distance between the motor and driver is extended to 20 m (65.6 ft.) or longer, use a power supply of 24±4% VDC.
- The lead wires of the "cable for electromagnetic brake" have polarities, so connect them in the correct polarities. If the lead wires are connected with their polarities reversed, the electromagnetic brake will not operate properly.

●Connecting the I/O signals

- Be certain the I/O signals cable is as short as possible. The maximum input frequency will decrease as the cable length increases.

●Connecting the power supply

Do not wire the power supply cable of the driver in the same cable duct with other power line or motor cable. Doing so may cause malfunction due to noise.
Pay attention to the polarity of the power supply. Reverse-polarity connection may cause damage to the driver.

⚠Caution The main power supply connector (CN1), data edit connector (CN4) and I/O signal connector (CN5) of the driver are not electrically insulated. When grounding the positive terminal of the power supply, do not connect any equipment (PC, etc.) whose negative terminal is grounded. Doing so may cause the driver and these equipment to short, damaging both.

■I/O connector pin assignment

Pin No	Operating mode		Name	
	Positioning operation	Push-motion operation *1	Positioning operation	Push-motion operation *1
1	–		–	
2	GND		Ground connection	
3	ASG+		A-phase pulse output (Line driver)	
4	ASG−			
5	BSG+		B-phase pulse output (Line driver)	
6	BSG−			
7	TIM1+		Timing output (Line driver)	
8	TIM1−			
9	ALM+		Alarm output	
10	ALM−			
11	WNG+		Warning output	
12	WNG−			
13	END+		Positioning completion output	
14	END−			
15	READY+/AL0+ *1		Operation ready complete output/Alarm code output 0	
16	READY−/AL0− *1			
17	TLC+/AL1+ *1		Torque limit output/ Alarm code output 1	
18	TLC−/AL1− *1			
19	TIM2+/AL2+ *1		Timing output (Open collector)/Alarm code output 2	
20	TIM2−/AL2− *1			
21	GND		Ground connection	
22	IN-COM		Input common	
23	**C-ON** *2		Current ON input	
24	CLR/ALM-RST		Deviation clear input/ Alarm reset input	
25	CCM		Current control mode ON input	
26	CS	T-MODE *1	Resolution selection input	Push-motion operation ON
27	–	M0 *1	–	Push-current setting selection input
28	RETURN	M1 *1	Return to electrical home operation	
29	P-RESET	M2 *1	Position reset input	
30	FREE		Excitation OFF	
31	CW+/PLS+		CW pulse input/Pulse input (+5 V or line driver)	
32	CW−/PLS−			
33	CW+24 V/PLS+24 V		CW pulse input/Pulse input (+24 V)	
34	CCW+24 V/DIR+24 V		CCW pulse input/Direction input (+24 V)	
35	CCW+/DIR+		CCW pulse input/Direction input (+5 V or line driver)	
36	CCW−/ DIR−			

*1 The signal will become effective if the applicable setting has been changed using the accessory **OPX-2A** (sold separately) or **MEXE02**.

*2 Factory setting of the C-ON input logic is "normally open." Be sure to turn the C-ON input ON when operating the motor. Set the C-ON input logic to "normally closed" when the C-ON input is not used.

Setting

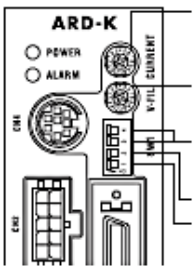

Current setting switch (Factory setting: F)
Set a desired operating current. The operating current to be set is the maximum output current multiplied by the operating current rate (%).

Speed filter setting switch (Factory setting: 1)
The motor response to input pulses can be adjusted.

Resolution switch (Factory setting: OFF)
Set a desired resolution per revolution of the motor output shaft.

Keep this switch in the OFF position.

Pulse input mode select switch
Set a desired pulse input mode of the driver.
OFF: 2-pulse input mode
ON: 1-pulse input mode

■ Note

- The new settings of the resolution switches or pulse input mode select switch will become effective after the power is cycled.
- Excessively low operating current may cause a problem in starting the motor or holding the load in position. Do not lower the operating current more than necessary.
- When changing the resolution using the CS input, use the switches in "No.3: OFF"/"No.4: OFF" or "No.3: OFF"/"No.4: ON" combination. If the CS input is turned ON when "No.3: ON" is selected, the resolution will not be changed.

●Resolution

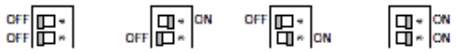

Resolution 1000 P/R (Factory setting) | Resolution 500 P/R | Resolution 10000 P/R | Resolution 5000 P/R

●Operating current

Dial setting	Operating current rate (%)	Dial setting	Operating current rate (%)
0	6.3	8	56.3
1	12.5	9	62.5
2	18.8	A	68.8
3	25.0	B	75.0
4	31.3	C	81.3
5	37.5	D	87.5
6	43.8	E	93.8
7	50.0	F	100 (Factory setting)

●Speed filter

Dial setting	Speed filter time constant (ms)	Dial setting	Speed filter time constant (ms)
0	0	8	30
1	1 (Factory setting)	9	50
2	2	A	70
3	3	B	100
4	5	C	120
5	7	D	150
6	10	E	170
7	20	F	200

Safety precautions

The precautions described below are intended to prevent danger or injury to the user and other personnel through safe, correct use of the product. Use the product only after carefully reading and fully understanding these instructions.

⚠Warning

Handling the product without observing the instructions that accompany a "Warning" symbol may result in serious injury or death.

General

- Do not use the product in explosive or corrosive environments, in the presence of flammable gases, locations subjected to splashing water, or near combustibles. Failure to do so may result in fire or injury.
- Assign qualified personnel the task of installing, wiring, operating/controlling, inspecting and troubleshooting the product. Failure to do so may result in fire, injury or damage to equipment.
- When the driver generates an alarm (protective functions is triggered), take measures to hold the moving part in place since the motor stops and loses its holding torque. Failure to do so may result in injury or damage to equipment.
- When the driver generates an alarm (protective functions is triggered), first remove the cause and then clear the protection function. Continuing the operation without removing the cause of the problem may cause malfunction of the motor and driver, leading to injury or damage to equipment.

Installation

- Install the driver in the enclosure in order to prevent injury.

Connection

- Keep the driver's input power voltage within the specified range. Failure to do so may result in fire.
- For the driver's power supply, use a DC power supply with reinforced insulation on its primary and secondary sides. Failure to do so may result in electric shock.
- Connect the cables securely according to the wiring diagram. Failure to do so may result in fire.
- Do not forcibly bend, pull or pinch the cable. Doing so may cause fire.

Operation

- Turn off the driver power in the event of a power failure. Or the motor may suddenly start when the power is restored and may cause injury or damage to equipment.
- Do not turn the FREE input to ON while the motor is operating. The motor will stop and lose its holding power. Doing so may result in injury or damage to equipment.

Repair, disassembly and modification

- Do not disassemble or modify the driver. Doing so may cause injury. Refer all such internal inspections and repairs to the branch or sales office from which you purchased the product.

⚠Caution

Handling the product without observing the instructions that accompany a "Caution" symbol may result in injury or property damage.

General

- Do not use the driver beyond its specifications. Doing so may result in injury or damage to equipment.
- Keep your fingers and objects out of the openings in the driver. Failure to do so may result in fire or injury.
- Do not touch the driver during operation or immediately after stopping. The surface is hot and may cause a skin burn(s).

Installation

- Do not leave anything around the driver that would obstruct ventilation. Doing so may result in damage to equipment.

Connection

- The main power supply connector (CN1), data edit connector (CN4) and I/O signal connector (CN5) of the driver are not electrically insulated. When grounding the positive terminal of the power supply, do not connect any equipment (PC, etc.) whose negative terminal is grounded. Doing so may cause the driver and these equipment to short, damaging both.

Operation

- Use a motor and driver only in the specified combination. An incorrect combination may cause a fire.
- Provide an emergency stop device or emergency stop circuit external to the equipment so that the entire equipment will operate safely in the event of a system failure or malfunction. Failure to do so may result in injury.
- Before supplying power to the driver, turn all input signals to the driver OFF. Otherwise, the motor may start suddenly at power ON and cause injury or damage to equipment.
- Before moving the motor directly with the hands, confirm that the FREE input turns ON. Failure to do so may result in injury.
- Immediately when trouble has occurred, stop running and turn off the driver power. Failure to do so may result in fire or injury.

Disposal

- To dispose of the driver, disassemble it into parts and components as much as possible and dispose of individual parts/components as industrial waste.

Precautions for use

This section covers limitations and requirements the user should consider when using the product.

- Always use the cable (supplied or accessory) to connect the motor and driver.

Be sure to use the cable (supplied or accessory) to connect the motor and driver. In the following condition, an appropriate accessory cable must be purchased separately.

- If a flexible cable is to be used.
- If a cable of 3 m (9.8 ft.) or longer is to be used.
- If a motor and driver package without a cable was purchased.

- Perform the insulation resistance test or dielectric strength test separately on the motor and the driver.

Performing the insulation resistance test or dielectric strength test with the motor and driver connected may result in damage to the product.

- Saving data to the NV memory

Do not turn off the main power supply while writing the data to the NV memory and 5 seconds after the completion of writing the data. Doing so may abort writing the data and cause a EEPROM error alarm to generate. The NV memory can be rewritten approx. 100,000 times.

- Motor excitation at power ON

Simply turning on the power will not excite the motor. To excite the motor, always turn the C-ON input ON.
It is possible to set the motor to be excited automatically after the power has been turned on, by changing the applicable driver parameter using the accessory **OPX-2A** (sold separately) or **MEXE02**.

- Overvoltage alarm by regeneration energy

The overvoltage alarm will generate depending on the operating condition. When an alarm is generated, review the operating conditions.

- Note on connecting a power supply whose positive terminal is grounded

The main power supply connector (CN1), data edit connector (CN4) and I/O signal connector (CN5) of the driver are not electrically insulated. When grounding the positive terminal of the power supply, do not connect any equipment (PC, etc.) whose negative terminal is grounded. Doing so may cause the driver and these equipment to short, damaging both. Use the accessory **OPX-2A** (sold separately) to set data, etc.

- Do not perform push-motion operation with geared types.

Doing so may cause damage to the motor or gear part.

General specifications

Operation environment	Degree of protection	IP20
	Ambient temperature	0 to +50 °C (+32 to +122 °F) (non-freezing)
	Humidity	85% or less (non-condensing)
	Altitude	Up to 1000 m (3300 ft.) above sea level
	Surrounding atmosphere	No corrosive gas, dust, water or oil
Storage environment Shipping environment	Ambient temperature	−20 to +60 °C (−4 to +140 °F) (non-freezing)
	Humidity	85% or less (non-condensing)
	Altitude	Up to 3000 m (10000 ft.) above sea level
	Surrounding atmosphere	No corrosive gas, dust, water or oil

Combinations of motors and drivers

- □ will be filled with **A** (single shaft), **B** (double shaft) or **M** (with electromagnetic brake).
  For **AR14S** and **AR15S**, □ indicates **A** (single shaft) or **B** (double shaft).
  For geared type, □ indicates **A** (single shaft) or **M** (with electromagnetic brake).
- ■ represents a number indicating the gear ratio.
- ○ indicates the cable length (**-1**, **-2**, **-3**) when the connection cable is supplied.

●Standard type

Model	Motor model	Driver model
AR14S□K○	ARM14S□K	ARD-K
AR15S□K○	ARM15S□K	
AR24S□K○	ARM24S□K	
AR26S□K○	ARM26S□K	
AR46S□K○	ARM46S□K	
AR46□K○	ARM46□K	
AR66S□K○	ARM66S□K	
AR66□K○	ARM66□K	
AR69S□K○	ARM69S□K	
AR69□K○	ARM69□K	
AR98S□K○	ARM98S□K	
AR98□K○	ARM98□K	

●TH geared type

Model	Motor model	Driver model
AR24S□K-T■○	ARM24S□K-T■	ARD-K
AR46S□K-T■○	ARM46S□K-T■	
AR46□K-T■○	ARM46□K-T■	
AR66S□K-T■○	ARM66S□K-T■	
AR66□K-T■○	ARM66□K-T■	
AR98S□K-T■○	ARM98S□K-T■	
AR98□K-T■○	ARM98□K-T■	

●PS geared type

Model	Motor model	Driver model
AR24SAK-PS■○	ARM24SAK-PS■	ARD-K
AR46S□K-PS■○	ARM46S□K-PS■	
AR46□K-PS■○	ARM46□K-PS■	
AR66S□K-PS■○	ARM66S□K-PS■	
AR66□K-PS■○	ARM66□K-PS■	
AR98S□K-PS■○	ARM98S□K-PS■	
AR98□K-PS■○	ARM98□K-PS■	

●PN geared type

Model	Motor model	Driver model
AR24SAK-N■○	ARM24SAK-N■	ARD-K
AR46S□K-N■○	ARM46S□K-N■	
AR46□K-N■○	ARM46□K-N■	
AR66S□K-N■○	ARM66S□K-N■	
AR66□K-N■○	ARM66□K-N■	
AR98S□K-N■○	ARM98S□K-N■	
AR98□K-N■○	ARM98□K-N■	

●Harmonic geared type

Model	Motor model	Driver model
AR24S□K-H■○	ARM24S□K-H■	ARD-K
AR46S□K-H■○	ARM46S□K-H■	
AR46□K-H■○	ARM46□K-H■	
AR66S□K-H■○	ARM66S□K-H■	
AR66□K-H■○	ARM66□K-H■	
AR98S□K-H■○	ARM98S□K-H■	
AR98□K-H■○	ARM98□K-H■	

- Unauthorized reproduction or copying of all or part of this manual is prohibited.
- Oriental Motor shall not be liable whatsoever for any problems relating to industrial property rights arising from use of any information, circuit, equipment or device provided or referenced in this manual.
- Characteristics, specifications and dimensions are subject to change without notice.
- While we make every effort to offer accurate information in the manual, we welcome your input. Should you find unclear descriptions, errors or omissions, please contact the nearest office.
- **Orientalmotor** and **αSTEP** are registered trademark or trademark of Oriental Motor Co., Ltd., in Japan and other countries.

• Please contact your nearest Oriental Motor office for further information.

ORIENTAL MOTOR U.S.A. CORP.
Technical Support Tel:(800)468-3982
8:30 A.M. to 5:00 P.M., P.S.T. (M-F)
7:30 A.M. to 5:00 P.M., C.S.T. (M-F)
www.orientalmotor.com

ORIENTAL MOTOR DO BRASIL LTDA.
Tel:+55-11-3266-6018
www.orientalmotor.com.br

ORIENTAL MOTOR (EUROPA) GmbH
Headquarters Düsseldorf, Germany
Technical Support Tel:00 800/22 55 66 22
www.orientalmotor.de

ORIENTAL MOTOR (UK) LTD.
Tel:01256-347090
www.oriental-motor.co.uk

ORIENTAL MOTOR (FRANCE) SARL
Tel:01 47 86 97 50
www.orientalmotor.fr

ORIENTAL MOTOR ITALIA s.r.l.
Tel:02-93906346
www.orientalmotor.it

ORIENTAL MOTOR CO., LTD.
Headquarters Tokyo, Japan
Tel:03-6744-0361
www.orientalmotor.co.jp

ORIENTAL MOTOR ASIA PACIFIC PTE. LTD.
Singapore
Tel:1800-8420280
www.orientalmotor.com.sg

ORIENTAL MOTOR (MALAYSIA) SDN. BHD.
Tel:1800-806161
www.orientalmotor.com.my

ORIENTAL MOTOR (THAILAND) CO., LTD.
Tel:1800-888-881
www.orientalmotor.co.th

ORIENTAL MOTOR (INDIA) PVT. LTD.
Tel:+91-80-41125586
www.orientalmotor.co.in

TAIWAN ORIENTAL MOTOR CO., LTD.
Tel:0800-060708
www.orientalmotor.com.tw

SHANGHAI ORIENTAL MOTOR CO., LTD.
Tel:400-820-6516
www.orientalmotor.com.cn

INA ORIENTAL MOTOR CO., LTD.
Korea
Tel:080-777-2042
www.inaom.co.kr

ORIENTAL MOTOR CO., LTD.
Hong Kong Branch
Tel:+852-2427-9800

CE Marking

■Low Voltage Directives

Because the input power supply voltage of this product is 24 VDC/48 VDC, it is not subject to the Low Voltage Directive but install and connect this product as follows.

- This product is designed and manufactured to be installed within another device. Install the product in an enclosure.
- For the driver power supply, use a DC power supply with reinforced insulation on its primary and secondary sides.

■EMC Directive

This product has received EMC compliance under the conditions specified in "Example of motor and driver installation and wiring" on USER MANUAL.
Since the compliance of the final machinery with the EMC Directive will depend on such factors as the configuration, wiring, layout and risk involved in the control-system equipment and electrical parts, it therefore must be verified through EMC measures by the customer of the machinery.

• Applicable Standards

EMI	EN 61000-6-4 EN 61800-3 EN 55011 group 1 class A
EMS	EN 61000-6-2 EN 61800-3

Input/output power ratings

Frame size [mm (in.)]	Model	Motor model	Driver model	Input		Output current
				Voltage	Current	
20 (0.79)	**AR14**	ARM14	ARD-K	24 VDC	0.4 A	0.43 A
	AR15	ARM15			0.5 A	0.52 A
28 (1.10) 30 (1.18)	**AR24**	ARM24			0.9 A	0.88 A
	AR26	ARM26				
42 (1.65)	**AR46**	ARM46		24 VDC 48 VDC	1.4 A	1.48 A
60 (2.36)	**AR66**	ARM66			3.1 A	2.55 A
	AR69	ARM69			3.0 A	
85 (3.35) 90 (3.54)	**AR98**	ARM98			2.5 A	

APPENDIX C

GOLDEN DRAGON PLUS WITH CHIP LEVEL CONVERSION (CLC)

Golden DRAGON Plus with Chip Level Conversion (CLC)
Lead (Pb) Free Product - RoHS Compliant

LUW W5AM

Vorläufige Daten / Preliminary Data

Besondere Merkmale
- **Gehäusetyp:** weißes SMD Gehäuse, klarer Silikon - Verguss, klare Silikonlinse, Chip level conversion
- **Typischer Lichtstrom:** 113 lm bei 350 mA bis zu 267 lm bei 1 A
- **Besonderheit des Bauteils:** hocheffiziente Lichtquelle bei geringem Platzbedarf
- **Farbort:** x = 0,31, y = 0,32 nach CIE 1931 (weiß)
- **typische Farbtemperatur:** 6500 K
- **Abstrahlwinkel:** 170°
- **Technologie:** ThinGaN
- **optischer Wirkungsgrad:** 128 lm/W bei 100 mA
- **Gruppierungsparameter:** Lichtstrom, Farbort
- **Verarbeitungsmethode:** für alle SMT-Bestücktechniken geeignet
- **Lötmethode:** Reflow Löten
- **Vorbehandlung:** nach JEDEC Level 4
- **Gurtung:** 24-mm Gurt mit 200/Rolle, ø180 mm
- **ESD-Festigkeit:** ESD-sicher bis 2 kV nach JESD22-A114-D

Features
- **package:** white SMD package, colorless clear silicone resin, clear silicone lens, chip level conversion
- **typical Luminous Flux:** 113 lm at 350 mA up to 267 lm at 1 A
- **feature of the device:** high efficient lightsource at low space
- **color coordinates:** x = 0.31, y = 0.32 acc. to CIE 1931 (white)
- **typ. color temperature:** 6500 K
- **viewing angle:** 170°
- **technology:** ThinGaN
- **optical efficiency:** 128 lm/W at 100 mA
- **grouping parameter:** luminous flux, color coordinates
- **assembly methods:** suitable for all SMT assembly methods
- **soldering methods:** reflow soldering
- **preconditioning:** acc. to JEDEC Level 4
- **taping:** 24 mm tape with 200/reel, ø180 mm
- **ESD-withstand voltage:** up to 2 kV acc. to JESD22-A114-D

Anwendungen
- Blitzlicht
- Hinterleuchtung (Werbebeleuchtung, Allgemeinbeleuchtung)
- Leseleuchten
- Ersatz von Kleinst-Glühlampen
- Fassadenbeleuchtung im Innen- und Außenbereich
- Display Hinterleuchtung mit hohem Helligkeitsbedarf
- Dekorative Beleuchtung
- Signal- und Symbolleuchten zur Orientierung
- Markierungsbeleuchtung (Stufen, Fluchtwege, u.ä.)
- Straßenbeleuchtung
- Tunnelbeleuchtung
- Deckenleuchten

Applications
- Flashlight
- backlighting (illuminated advertising, general lighting)
- reading lamps
- substitution of micro incandescent lamps
- indoor and outdoor commercial and residential architectural lighting
- display backlight where high brightness is required
- decorative and entertainment lighting
- signal and symbol luminaire for orientation
- marker lights (e.g. steps, exit ways, etc.)
- street lighting
- tunnel lighting
- ceiling light

Bestellinformation
Ordering Information

Typ Type	Emissions-farbe Color of Emission	Lichtstrom[1] Seite 20 Luminous Flux[1] page 20 I_F = 350 mA Φ_V (mlm)	Lichtstärke[2] Seite 20 Luminous Intensity[2] page 20 I_F = 350 mA I_V (mcd)	Bestellnummer Ordering Code
LUW W5AM-KYLX-6P7Q	white	82.000 ... 130.000	26.500 (typ.)	Q65110A7564
LUW W5AM-KZLY-6P7R	white	97.000 ... 150.000	30.900 (typ.)	Q65110A8397
LUW W5AM-LXLY-6P7R	white	112.000 ... 150.000	32.800 (typ.)	Q65110A8399

Bestellinformation
Ordering Information

Typ Type	Farbtemperatur color temperature	Lichtstrom[1] Seite 20 Luminous Flux[1] page 20 I_F = 350 mA Φ_V (mlm)	Lichtstärke[2] Seite 20 Luminous Intensity[2] page 20 I_F = 350 mA I_V (mcd)	Bestellnummer Ordering Code
LUW W5AM-KYLX-4C8E	6500 K	82.000 ... 130.000	26.500 (typ.)	Q65110A9531
LUW W5AM-KYLX-4E8G	5700 K	82.000 ... 130.000	26.500 (typ.)	Q65110A9533

*Anm.: Die oben genannten Typbezeichnungen umfassen die bestellbaren Selektionen. Diese bestehen aus wenigen Helligkeitsgruppen (siehe **Seite 8** für nähere Informationen). Es wird nur eine einzige Helligkeitsgruppe pro Gurt geliefert. Z.B.: LUW W5AM-KZLY-6P7R bedeutet, dass auf dem Gurt nur eine der Helligkeitsgruppen KZ, LX oder LY enthalten ist.*
Um die Liefersicherheit zu gewährleisten, können einzelne Helligkeitsgruppen nicht bestellt werden.

*Gleiches gilt für die Farben, bei denen Farbortgruppen gemessen und gruppiert werden. Pro Gurt wird nur eine Farbortgruppe geliefert. Z.B.: LUW W5AM-KZLY-6P7R bedeutet, dass auf dem Gurt nur eine der Farbortgruppen -6P bis -7R enthalten ist (siehe **Seite 5** für nähere Information).*
Um die Liefersicherheit zu gewährleisten, können einzelne Farbortgruppen nicht bestellt werden.

*Note: The above Type Numbers represent the order groups which include only a few brightness groups (see **page 8** for explanation). Only one group will be shipped on each reel (there will be no mixing of two groups on each reel). E.g. LUW W5AM-KZLY-6P7R means that only one group KZ, LXor LY will be shippable for any one reel.*
In order to ensure availability, single brightness groups will not be orderable.

*In a similar manner for colors where chromaticity coordinate groups are measured and binned, single chromaticity coordinate groups will be shipped on any one reel. E.g. LUW W5AM-KZLY-6P7R means that only 1 chromaticity coordinate group -6P to 7R will be shippable on each reel (see **page 5** for explanation).*
In order to ensure availability, single chromaticity coordinate groups will not be orderable.

Grenzwerte
Maximum Ratings

Bezeichnung Parameter		Symbol Symbol	Wert Value	Einheit Unit
Betriebstemperatur Operating temperature range		T_{op}	– 40 ... + 110	°C
Lagertemperatur Storage temperature range		T_{stg}	– 40 ... + 110	°C
Sperrschichttemperatur Junction temperature		T_j	125	°C
Durchlassstrom Forward current (T_A=25°C)	(min.) (max.)	I_F I_F	100 1000	mA mA
Stoßstrom Surge current $t \leq 10$ µs, $D = 0.005$, T_A=25°C		I_{FM}	2000	mA
Sperrspannung Reverse voltage (T_A=25°C)		V_R	not designed for reverse operation	V
Leistungsaufnahme Power consumption (T_A=25°C)		P_{tot}	3.8	W

Kennwerte
Characteristics
(T_A = 25 °C)

Bezeichnung Parameter		Symbol Symbol	Wert Value	Einheit Unit
Farbkoordinate x nach CIE 1931[5) Seite 20] Chromaticity coordinate x acc. to CIE 1931[5) page 20] I_F = 350 mA	(typ.)	x	0.31	–
Farbkoordinate y nach CIE 1931[5) Seite 20] Chromaticity coordinate y acc. to CIE 1931[5) page 20] I_F = 350 mA	(typ.)	y	0.32	–
Abstrahlwinkel bei 50 % I_V (Vollwinkel) Viewing angle at 50 % I_V	(typ.)	2φ	170	Grad deg.
Durchlassspannung [6 Seite 20)] Forward voltage[6) page 20] I_F = 350 mA	(min.) (typ.) (max.)	V_F V_F V_F	2.7 3.2 3.7	V V V
Sperrstrom Reverse current	(max.)	I_R	not designed for reverse operation	µA
Optischer Wirkungsgrad Optical efficiency I_F = 100 mA	(typ.)	η_{opt}	128	lm/W
Wärmewiderstand Thermal resistance Sperrschicht/Lötpad Junction/soldering point	 (typ.) (max.)	 $R_{th\ JS}$ $R_{th\ JS}$	 6.5 11*	 K/W K/W

*R_{th}(max) basiert auf statistischen Werten
R_{th}(max) is based on statistic values

Farbortgruppen[5] Seite 20
Chromaticity coordinate groups[5] page 20

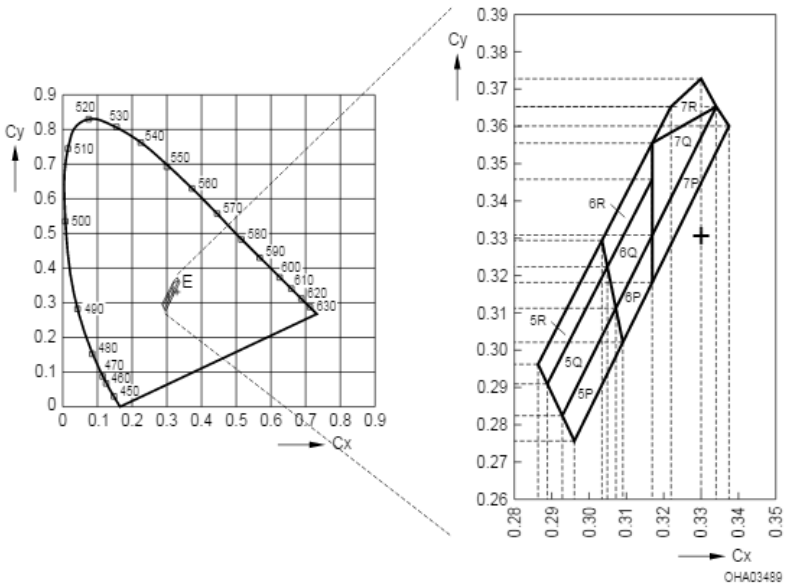

Gruppe Group	Cx	Cy
5P	0.296	0.276
	0.293	0.282
	0.307	0.311
	0.309	0.302
6P	0.309	0.302
	0.307	0.311
	0.317	0.331
	0.317	0.318
7P	0.317	0.318
	0.317	0.331
	0.334	0.365
	0.338	0.360

Gruppe Group	Cx	Cy
5Q	0.293	0.282
	0.289	0.291
	0.305	0.322
	0.307	0.311
6Q	0.307	0.311
	0.305	0.322
	0.317	0.346
	0.317	0.331
7Q	0.317	0.331
	0.317	0.356
	0.334	0.365
	0.317	0.331

Gruppe Group	Cx	Cy
5R	0.289	0.291
	0.287	0.296
	0.304	0.329
	0.305	0.322
6R	0.305	0.322
	0.304	0.329
	0.317	0.356
	0.317	0.346
7R	0.317	0.356
	0.322	0.365
	0.330	0.373
	0.334	0.365

Farbortgruppen[5) Seite 20]
Chromaticity coordinate groups[5) page 20]

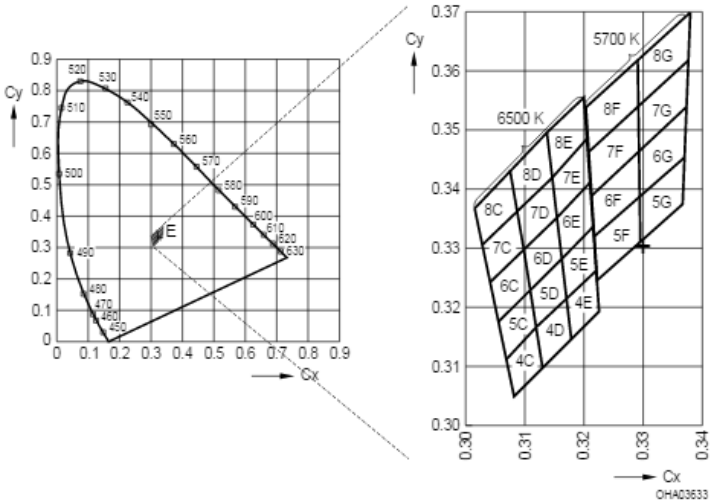

Gruppe Group	Cx	Cy
4C	0.308	0.305
	0.307	0.311
	0.312	0.316
	0.313	0.310
5C	0.307	0.311
	0.306	0.318
	0.311	0.323
	0.312	0.316
6C	0.306	0.318
	0.304	0.324
	0.310	0.330
	0.311	0.323
7C	0.304	0.324
	0.303	0.330
	0.309	0.336
	0.310	0.330
8C	0.303	0.330
	0.302	0.337
	0.308	0.343
	0.309	0.336

Gruppe Group	Cx	Cy
5F	0.322	0.324
	0.322	0.332
	0.329	0.338
	0.329	0.331
6F	0.322	0.332
	0.321	0.339
	0.329	0.346
	0.329	0.338
7F	0.321	0.339
	0.321	0.346
	0.329	0.354
	0.329	0.346
8F	0.321	0.346
	0.320	0.354
	0.329	0.362
	0.329	0.354
5G	0.329	0.331
	0.329	0.338
	0.337	0.345
	0.337	0.337

Gruppe Group	Cx	Cy
4D	0.313	0.310
	0.312	0.316
	0.317	0.321
	0.318	0.314
5D	0.312	0.316
	0.311	0.323
	0.316	0.328
	0.317	0.321
6D	0.311	0.323
	0.310	0.330
	0.315	0.335
	0.316	0.328
7D	0.310	0.330
	0.309	0.336
	0.315	0.342
	0.315	0.335
8D	0.309	0.336
	0.308	0.343
	0.314	0.349
	0.315	0.342
4E	0.318	0.314
	0.317	0.321
	0.322	0.326
	0.323	0.319
5E	0.317	0.321
	0.316	0.328
	0.322	0.333
	0.322	0.326
6E	0.316	0.328
	0.315	0.335
	0.321	0.341
	0.322	0.333
7E	0.315	0.335
	0.315	0.342
	0.321	0.348
	0.321	0.341
8E	0.315	0.342
	0.314	0.349
	0.320	0.355
	0.321	0.348

Gruppe Group	Cx	Cy
6G	0.329	0.338
	0.329	0.346
	0.337	0.353
	0.337	0.345
7G	0.329	0.346
	0.329	0.354
	0.338	0.362
	0.337	0.353
8G	0.329	0.354
	0.329	0.362
	0.338	0.370
	0.338	0.362

Helligkeits-Gruppierungsschema
Brightness Groups

Helligkeitsgruppe Brightness Group	Lichtstrom[1) Seite 20] Luminous Flux[1) page 20] Φ_V (mlm)	Lichtstärke[2) Seite 20] Luminous Intensity[2) page 20] I_V (mcd)
KY	82.000 ... 97.000	22.400 (typ.)
KZ	97.000 ...112.000	26.100 (typ.)
LX	112.000 ...130.000	30.200 (typ.)
LY	130.000 ...150.000	35.000 (typ.)

Anm.: Die Standardlieferform von Serientypen beinhaltet eine Familiengruppe. Diese besteht aus wenigen Helligkeitsgruppen. Einzelne Helligkeitsgruppen sind nicht bestellbar.

Note: The standard shipping format for serial types includes a family group of only a few individual brightness groups. Individual brightness groups cannot be ordered.

Gruppenbezeichnung auf Etikett
Group Name on Label
Beispiel: KY-6P
Example: KY-6P

Helligkeitsgruppe Brightness Group	Farbortgruppe Chromaticity Coordinate Group
KY	6P

Anm.: In einer Verpackungseinheit / Gurt ist immer nur eine Helligkeitsgruppe enthalten.

Note: No packing unit / tape ever contains more than one brightness group.

Relative spektrale Emission[2) Seite 20]
Relative Spectral Emission[2) page 20]
V(λ) = spektrale Augenempfindlichkeit / Standard eye response curve
$\Phi_{rel} = f(\lambda)$; T_A = 25 °C; I_F = 350 mA

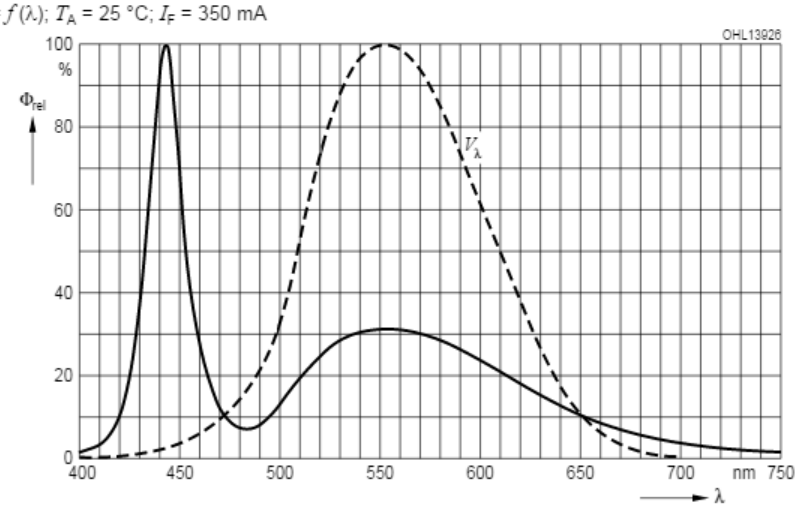

Abstrahlcharakteristik[2) Seite 20]
Radiation Characteristic[2) page 20]
$I_{rel} = f(\varphi)$; T_A = 25 °C

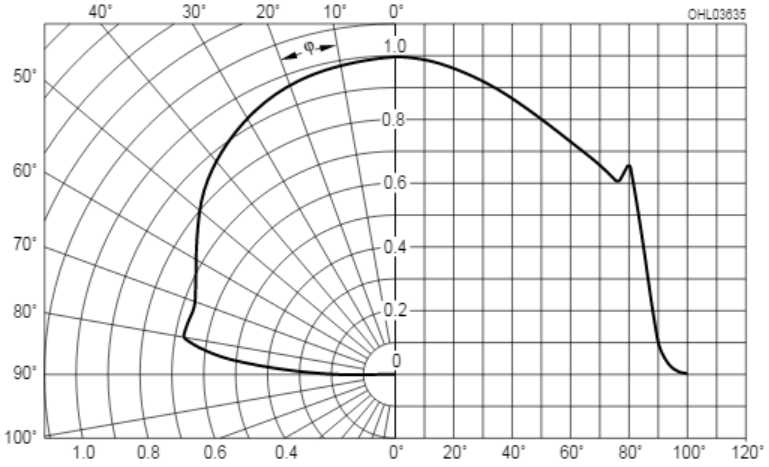

Durchlassstrom[2) Seite 20]
Forward Current[2) page 20]
$I_F = f(V_F)$; T_A = 25 °C

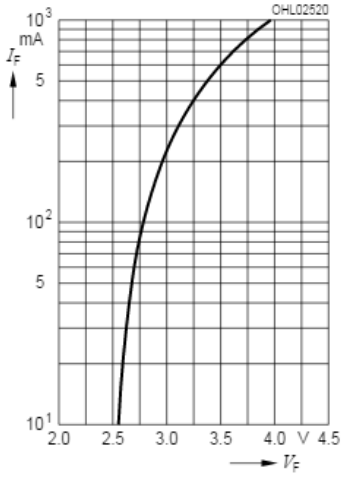

Relative Lichtstrom[2) 7) Seite 20]
Relative Luminous Flux[2) 7) page 20]
$\Phi_V/\Phi_{V(350\ mA)} = f(I_F)$; T_A = 25 °C

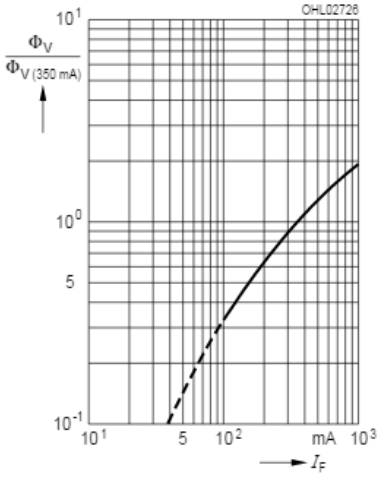

Farbortverschiebung[2) Seite 20]
Chromaticity Coordinate Shift[2) page 20]
x, y = $f(I_F)$; T_A = 25 °C

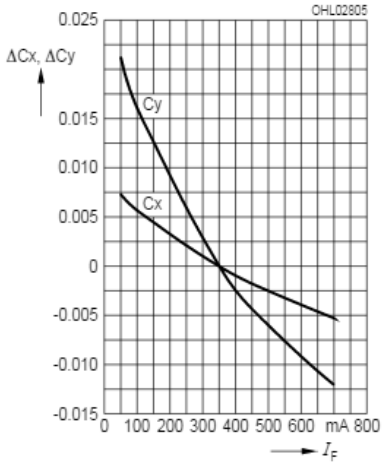

APPENDIX D

HAND-HELD DIGITAL MULTIMETER

Test Equipment Depot
1-800-517-8431
99 Washington Street
Melrose, MA 02176
Fax 781-665-0780
TestEquipmentDepot.com

D11

Hand-Held Digital Multimeter

GDM-394(3 3/4Digits)

FEATURES

* 3999 Counts Auto/Manual Ranging
* Capacitance, Frequency Measurement
* Continuity Beeper/Diode Test
* High Energy Fused For 10A Range
* Data Hold/Relative Mode

GDM-396(3 3/4Digits)

FEATURES

* 3999 Counts Auto/Manual Ranging
* High Energy Fused for 10A Range
* Capacitance, Frequency Measurement
* Continuity Beeper/Diode Test
* Data Hold/Relative Mode
* True RMS/RS232C

GDM-395(3 3/4Digits)

FEATURES

* Slim Pocket Digital Multimeter
* 3999 Counts Auto/Manual Ranging
* Capacitance, Frequency Measurement
* Continuity Beeper/Diode Test
* Data Hold/Relative Mode

SPECIFICATIONS

DC VOLTAGE
Range: 200mV, 2V, 20V, 200V, 1000V (GDM-451/356)
400mV, 4V, 40V, 400V, 1000V (GDM-394/396)
400mV, 4V, 40V, 400V, 600V (GDM-395)
200mV, 2V, 20V, 200V, 500V (GDM-350A)
Best Accuracy: ± (0.05%rdg + 3digits) for GDM-451
± (0.8%rdg + 1digit) for GDM-394/396
± (0.5%rdg + 1digit) for GDM-356
± (0.7%rdg + 3digits) for GDM-395
± (0.5%rdg + 2digits) for GDM-350A
Input Impedance: 10MΩ

AC VOLTAGE (40Hz ~ 400Hz)
Range: 2V, 20V, 200V, 750V (GDM-451/356)
4V, 40V, 400V, 750V (GDM-394/396)
4V, 40V, 400V, 600V (GDM-395)
200V, 500V (GDM-350A)
Best Accuracy: ± (0.5%rdg + 10 digits) for GDM-451
± (1%rdg + 5 digits) for GDM-394/396
± (2.3%rdg + 5digits) for GDM-395
± (0.8%rdg + 3digits) for GDM-356
± (1.2%rdg + 10 digits) for GDM-350A
Input Impedance: 10MΩ(5MΩ for GDM-350A)(2MΩ for GDM-451)

DC CURRENT
Range: 2mA, 20mA, 200mA, 20A (GDM-451)
400uA,4mA,40mA,400mA,4A,10A(GDM-394/396)
200uA, 2mA, 20mA, 200mA, 10A (GDM-350A)
20mA, 200mA, 20A (GDM-356)
Best Accuracy: ± (0.5%rdg + 5digits) for GDM-451
± (1%rdg + 2 digits) for GDM-394/396/350A
± (0.8%rdg + 1digit) for GDM-356

AC CURRENT (50Hz ~ 400Hz)
Range: 20mA, 200mA, 20A (GDM-451/356)
400uA,4mA,40mA,400mA,4A,10A(GDM-394/396)
Best Accuracy: ± (0.8%rdg + 10 digits) for GDM-451
± (1.5%rdg + 5digits) for GDM-394/396
± (1%rdg + 3 digits) for GDM-356

RESISTANCE
Range: 200Ω ~ 200MΩ 7 ranges (GDM-451)
200Ω ~ 200MΩ 7 ranges (GDM-356)
400Ω ~ 40MΩ 6 ranges (GDM-394/395/396)
200Ω ~ 20MΩ 6 ranges (GDM-350A)
Best Accuracy: ± (0.3%rdg + 1 digit) for GDM-451
± (1%rdg +2 digits) for GDM-394/396
± (2%rdg +5 digits) for GDM-395
± (0.8%rdg + 1 digit) for GDM-356
± (0.8%rdg + 2 digits) for GDM-350A

CONTINUITY BEEPER
Buzzer sounds if conductance less than 70Ω

DIODE TEST
Open Voltage: 3.0V typical (1.5V Typical for GDM-395)

CAPACITANCE
Range: 2nF, 20nF, 2μF, 20μF (GDM-451)
20nF, 200nF, 2μF, 100μF (GDM-356)
40nF,400nF,4μF,40μF,100μF(GDM-394/395/396)
Best Accuracy: ± (3%rdg + 40 digits) for GDM-451
± (3%rdg +5 digits) for GDM-394/396
± (5%rdg +10 digits) for GDM-395
± (4%rdg + 3 digits) for GDM-356

FREQUENCY
Range: 1Hz~20kHz (GDM-451/356)
10Hz ~ 10MHz (GDM-394/396)
1Hz~99.9kHz (GDM-395)
Best Accuracy: ± (1.5%rdg + 5 digits) for GDM-451/356
± (0.1%rdg + 3digits) for GDM-394/396
± (0.7%rdg + 3digits) for GDM-395

TEMPERATURE(℃)
Range: -40℃~1000℃
Best Accuracy: ±1%+30 (GDM-451)
±1%+3 (GDM-396/356/350A)

SPECIAL FUNCTION
Duty cycle, Auto Ranging (GDM-394/396)
True RMS, RS232C (GDM-396)

LCD DISPLAY
4 1/2 digits (GDM-451), 3999 counts (GDM-394/395/396),
3 1/2 digits (GDM-356/350A)

POWER SOURCE
Single 9V battery (6F22), Cell Battery for GDM-395(CR2032)

ACCESSORIES
Instruction manual , Battery , Test leads

DIMENSIONS & WEIGHT
85(W) x 177(H) x 40(D) mm , Approx.330g (GDM-394/396)
80(W) x 165(H) x 38.3(D) mm, Approx. 275g (GDM-451/356)
73.5(W) x 130(H) x 35(D) mm, Approx. 156g (GDM-350A)
56(W) x 110(L) x 11.5(D) mm, Approx. 97g (GDM-395)

Test Equipment Depot
1-800-517-8431
99 Washington Street
Melrose, MA 02176
Fax 781-665-0780
TestEquipmentDepot.com

Hand-Held Digital Multimeter

GDM-451(4 1/2Digits)

FEATURES

* 4 1/2Digits 19999 counts
* Manual Ranging
* Continuity Check/DiodeTest
* Data Hold
* Temperature Measurement
* Capacitance, Frequency Measurement

GDM-356(3 1/2Digits)

FEATURES

* 3 1/2 Digits 1999 counts
* Manual Ranging
* Continuity Beeper/Diode Test
* Capacitance Measurement
* Frequency, Temperature Measurement

GDM-350A(3 1/2Digits)

FEATURES

* 3 1/2 Digits 1999 counts
* Manual Ranging
* Continuity Beeper/Diode Test
* Temperature Measurement

SELECTION GUIDE

Special Function	GDM-451	GDM-394	GDM-396	GDM-356	GDM-350A	GDM-395
Max. Display	19999	3999	3999	1999	1999	3999
Fused 10A Range		✓	✓			
Auto Ranging		✓	✓			✓
Diode	✓	✓	✓	✓	✓	✓
Continuity	✓	✓	✓	✓	✓	✓
Capacitance	✓	✓	✓	✓		✓
Frequency	20k	10M	10M	20k		100k
Temperature	✓		✓	✓	✓	
Duty Cycle(%)		✓	✓			✓
True RMS			✓			
Relative mode		✓	✓			✓
Data Hold	✓	✓	✓	✓	✓	✓
RS232C			✓			
Display Backlight	✓	✓	✓	✓	✓	

ORDERING INFORMATION

GDM-451	4 1/2 Digits Hand-Held DMM
GDM-396	3 3/4 Digits Hand-Held DMM with True R.M.S, Measurement and RS-232C Inter face
GDM-394	3 3/4 Digits Hand-Held DMM
GDM-395	3 3/4 Digits Hand-Held DMM
GDM-356	3 1/2 Digits Hand-Held DMM
GDM-350A	3 1/2 Digits Hand-Held DMM

APPENDIX E

High acceptance angle optical fiber based daylighting system using two-stage reflective non-imaging dish concentrator

ELSEVIER

Available online at www.sciencedirect.com

ScienceDirect

Energy Procedia 105 (2017) 498 – 504

Energy Procedia

The 8th International Conference on Applied Energy – ICAE2016

High acceptance angle optical fiber based daylighting system using two-stage reflective non-imaging dish concentrator

Onubogu Nneka Obianuju, Kok-Keong Chong*

Lee Kong Chian Faculty of Engineering and Science, University Tunku Abdul Rahman, Jalan Sungai Long, Bandar Sungai Long, 43000 Kajang, Selangor, Malaysia

Abstract

It has been observed that lighting systems consume a significant amount of energy in high-rise buildings even during the daytime. To save power consumption and improve indoor environments, daylighting can be implemented for the interior of buildings by guiding sunlight via optical fibers. In this paper, we propose a new two-stage reflective non-imaging dish concentrator (NIDC) consisted of reflective primary and secondary mirrors that focus sunlight onto high acceptance angle optical fibers located at the target of the concentrator. The optical fibers can guide the concentrated sunlight into the interior area of the building. The new concentrating type of daylighting system was designed, fabricated and evaluated. Under normal sunny day condition with solar irradiance of 1000 W/m², the calculated average illuminance for our prototype daylighting system with a reflective area of 0.2 m² is 647.94 lux to illuminate an office area of 6.3 m², which is also equivalent to illuminate a bigger area of 8.164 m² based on standard average illumination of 500 lux.

Peer-review under responsibility of the scientific committee of the 8th International Conference on Applied Energy.

Keywords: daylighting; solar concentrator; raytracing; optical fiber; illuminance; NIDC

1. Introduction

Daylight building is estimated to reduce lighting energy consumption by 50–80% [1]. Direct use of sunlight is environmental friendly, cheaper and a greener way to produce daylighting inside a building than indirectly through electricity from non-renewable sources. Moreover, direct use of sunlight for daylighting is more efficient than converting light energy to electrical energy and back to light energy as this process involves a lot of losses during power conversion. Green building status by daylighting can be achieved with several methods but it is more effective and pollution free to guide the sunlight through the optical fibers and into the building.

* Corresponding author. Tel.: +603-90860288; fax: +603-90193886.
E-mail address: chongkk@utar.edu.my, kokkeong_c@yahoo.com

Peer-review under responsibility of the scientific committee of the 8th International Conference on Applied Energy.
doi:10.1016/j.egypro.2017.03.347

Studies in the past have revealed that various kinds of conventional concentrators such as Fresnel lens, heliostat, parabolic concentrator, compound parabolic concentrator, etc. have been employed for daylighting and have been tested for coupling with optical fibers to guide the sunlight [2-7]. Most of these concentrators are expensive, having low acceptance angle, or producing non-uniform concentrated sunlight. Non-imaging dish concentrator (NIDC) has been previously used for concentrator photovoltaic system [8-18]. The newly proposed active daylighting system consists of a non-imaging dish concentrator, which can have a low rim angle with respect to the selected optical fiber with a high acceptance angle as compared to conventional solar concentrators; can produce high solar concentration ratio with reasonably uniform illumination on the receiver. The new design is proposed to have two stages reflection, in which flat primary reflectors (mirrors) are designed to face the sun and secondary reflectors (mirrors) are located above but facing the primary mirrors so as to reflect the sunlight to the optical fiber aperture located at the center of the primary mirror arrangement.

The main aim of this proposed daylighting system design using solar concentrator, optical fiber and dual-axis solar tracker is to have the lowest possible cost compared to the existing ones and highest possible efficiency. More so, dual-axis solar tracking system can maximize the intensity of the sunlight input and provide constant intensity of the sunlight in order to have uniform distribution of solar flux.

2. Solar concentrator design

The proposed solar concentrator was designed based on the concept of the Cassegrain reflector that is widely used in reflecting telescopes. It is a combination of a primary concave mirror and a secondary convex mirror [19]. The incident ray strikes on the primary reflector and is reflected to the secondary reflector which reflects the rays to the target or focus. For the proposed design, concave and convex (parabolic) mirrors were found to be very expensive. Therefore, square flat mirrors to be tilted were used as primary and secondary reflectors while the target is a bundle of plastic optical fibers (POF).

2.1 2D Optical Ray-tracing

A readily available powerful, Java-based virtual optical bench called OpticalRay Tracer was used to verify the optical design of our system. Ray-tracing was performed in 2D from the primary mirror to the secondary mirror and then to the optical fiber. This was done mainly to get the required dimension for the secondary mirror as the dimension of each primary mirror was set to be 5 cm × 5 cm with a thickness of 0.2 cm. Each set consisted of four primary mirrors for easy adjustment with a distance of 0.5 cm from each other, which are all supposed to reflect to one secondary mirror located 60 cm above the primary mirror and finally reflects the light rays to the optical fiber. The total dimension of one set (4 mirrors) of primary mirrors is 10.5 cm × 10.5 cm. Since OpticalRay Tracer does ray-tracing in 2D, only two primary mirrors in a set of the four mirrors can be simulated. Two sets of reflections were simulated and the estimated size of the secondary mirror for all reflected rays to fit in was found to be 8 cm × 8 cm.

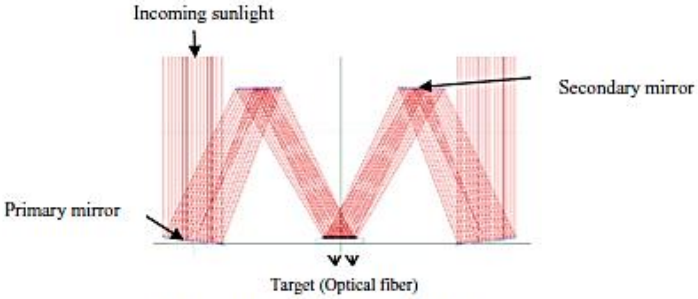

Fig. 1. 2D Raytracing using OpticalRay Tracer

2.2 3D CAD design of solar concentrator and prototype fabrication

After ray-tracing was completed, 3-D drawing of the entire structure was made in Solid Works and then the prototype was fabricated accordingly at the campus of Universiti Tunku Abdul Rahman, Bandar Sungai Long, Malaysia.

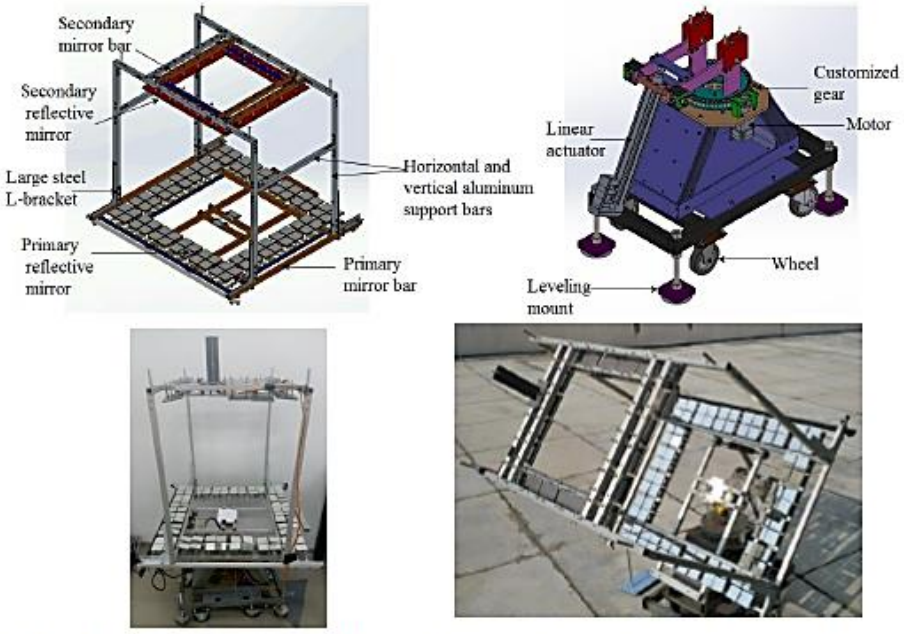

Fig. 2. (a) Parts of the upper portion of the dish concentrator in Solid Works; (b) Parts of the lower portion of the dish concentrator in Solid Works; (c) Prototype of the active solar daylighting system; (d) Prototype testing on the roof top of Universiti Tunku Abdul Rahman.

The prototype of non-imaging dish concentrator was fabricated with a sun-tracking mechanism comprised of a linear actuator (model: EAC4R-E300-ARMKE-2) to perform elevation motion (from 0° to 50°) and a stepper motor (model: PK264A2-SG50) connected to customized spur gears to perform azimuth motion (from 0° to 360°). The concentrator can track the sun in a dual-axis motion.

2.3 Given and calculated parameters of Two-stage non-imaging dish concentrator

From Figure 2, the weight of the upper portion of the concentrator is 16 kg and the weight of the whole concentrator is 42.2 kg. The height of the upper portion of the concentrator is 79 cm and the height of the entire structure is 135 cm. The size of the frame where the mirrors are located is 91 cm × 81 cm. Other parameters are listed in Table. 1.

Table 1. Given and calculated parameters of Two-stage non-imaging dish concentrator (NIDC)

Parameters	Value	Parameters	Value
Area of one primary mirror (cm^2)	25	Total loss (from cut-back testing + coupling loss) (%)	45.7
Number of primary mirrors	80	Typical solar radiation, I (W/m^2)	1000
Area of 80 primary mirrors, A (m^2)	0.2	Visible light (%)	47
Specular reflectivity of sliver coated mirrors, *ρm*	0.94	Infrared ray (%)	46
Hot Mirror transmissibility of visible light	0.98	Ultraviolet light (%)	7
Core reflective index of POF	1.49	Power captured by all the primary mirrors (W) = I x A =1000 W/m^2 x 0.2 m^2	200
Numerical aperture of POF	0.50	Power after two-stage reflection (W) = 200W x 0.94 x 0.94	176.72
Maximum operating temperature of POF (°C)	70	Visible light power as 47% of total spectrum (W) = 176.72W x 0.47	83.06
Length of POF (m)	10	Visible light after the hot mirror filter (W) = 83.06W x 0.98	81.399
Acceptance angle of POF (°)	30	Illuminance (lm) = luminous efficacy x power of visible light =104 lm/W x 81.399W	8465.48
Average value of direct beam luminous efficacy (lm/W) *provided by Lim and Ahmad based on Malaysian climate [20]	104		
Transmission loss of POF (dB/km)	200 max.		

Plastic optical fibers (POF) with model number CK-120 and 3 mm diameter each made of polymethyl metacrylate (PMMA) were placed at the center of the lower stage of the concentrator, which is the target area. Plastic optical fibers were selected because they are cheaper as compared to silica optical fibers and have a large core diameter for transmitting larger amount of light via total internal reflection.

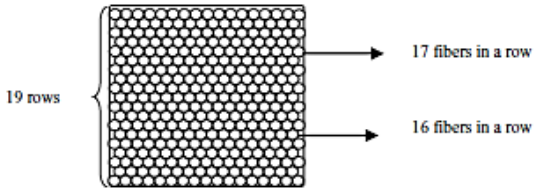

Fig. 3. Optical fibers arrangement in the target with area of 50 mm × 50 mm

The target area in which the fibers are located in the prototype solar concentrator is (50 × 50) mm^2 = 2500 mm^2. From calculations as shown in Table 1, the prototype solar concentrator is expected to deliver approximately 8465.48 lumens to the optical fibers. Thus, we can calculate the lumen that one optical fiber can transmit. First, the cross sectional area of each fiber is π × (1.5 mm)^2 = 7.07 mm^2. This means that one fiber can transmit (7.07 mm^2 × 8465.48 lm) / 2500 mm^2 = 23.94 lm. Since the optical fiber used is 10 m in length, the total loss incurred based on calibration of cutback testing and coupling loss is 45.7 %. Thus, the lumen emerged at the other end of 10 m optical fiber is expected as (23.94 lm × 54.3 %) = 13.00 lm (equivalent to 2.06 lux per fiber for 6.3 m^2 standard office area).

For daylighting from optical fiber in a standard office area of 6.3 m^2, the lumens required to achieve 500 lux was calculated as 3150 lm and therefore the total number of optical fibers needed is 3150/13 ≈ 242.3 fibers. As shown in Fig. 3, the target area can accommodate up to 314 optical fibers, which can provide an average illuminance of 13.00 lm × 314 = 4082 lm (or 647.94 lux for office area of 6.3 m^2). Hence, we can accomplish more than the required illuminance value for a standard office area with our prototype concentrator design. If an average illuminance of 500 lux is required, the average illuminance of our prototype design with 647.94 lux for a space of 6.3 m^2 can be used to illuminate a bigger office area of (647.94 lux × 6.3 m^2) / 500 lux = 8.164 m^2. The size of the solar concentrator can also be increased further to illuminate a larger office area.

To compensate the intermittent natural daylight especially when the illumination is less than the required level, light emitting diodes (LEDs) with model no. LUW W5AM-KYLX-4E8G were used as complementary artificial light source. In this case, LED was chosen because it consumes less power and has a long lifetime. As stated in the data sheet [21], one LED can produce 104 lm/W with the forward voltage (V_f) of 3.2 V, current of 350 mA and electrical input power of 1.12 W. For LEDs to fully illuminate an office area of 8.164 m^2, 4082 lm will be needed to achieve 500 lux and therefore about 35 LEDs with total rated electrical power of 1.12 W × 35 = 39.2 W will be needed. It means that the total lumens produced by our prototype daylighting system are equivalent to 35 LEDs with 1.12 W each. Considering the collected solar power by the prototype as 200 W (refer to Table 1), the equivalent power conversion efficiency can be calculated as (100 × 39.2 W)/200 W = 19.6 %.

3. Conclusion

The design and construction of a high acceptance angle optical fiber based daylighting system using two-stage non-imaging dish concentrator (NIDC) have been presented and evaluated. The results of our calculation has shown that our system has the capacity to illuminate an office area of 6.3 m^2 with a higher average illuminance of 647.94 lux under a normal sunny day of solar irradiance 1000 W/m^2, which is also equivalent to a larger area of 8.164 m^2 based on standard average illumination of 500 lux.

Acknowledgements

The authors would like to express their sincere gratitude to Ministry of Energy, Green Technology, and Water (AAIBE Trust Fund) with vote account 4356/001, and UTAR Research Fund 2014 Cycle 2 with project number IPSR/RMC/UTARRF/2014-C2/C02 and vote account 6200/C91 for their financial support.

References

[1] U.S. Green Building Council; 1995. Green Building Rating Systems -Draft Recommendations for a U.S. Rating System. Bethesda, Md.

[2] Ullah I, Shin S. Highly concentrated optical fiber-based daylighting systems for multi-floor office buildings. *Energy and Buildings* 2014;**72**:246-261.

[3] Song J, Zhu Y, Jin Z, Yang Y. Daylighting system via fibers based on two-stage sun-tracking model. *Sol Energy* 2014;**108**:331–9. doi:10.1016/j.solener.2014.07.021.

[4] Muhs J. Design and analysis of hybrid solar lighting and full-spectrum solar energy systems. *American Solar Energy Society's*. Madison, Wisconsin; July 16-21; 2000.

[5] Sapia C. Daylighting in buildings: Developments of sunlight addressing by optical fiber. *Sol Energy*, 2013;**89**:113-121.

[6] Schlegel G, Burkholder F, Klein S, Beckman W, Wood B and Muhs J. Analysis of a full spectrum hybrid lighting system. *Sol Energy*, 2004; **76**(4):359-368.

[7] Ullah I, Shin S. Concept of solar tower for daylighting in multi-floor buildings. *J Green Sct Tech 2013;* **1**(2):79-84.

[8] Chong KK, Siaw FL, Wong CW, Wong GS. Design and construction of non-imaging planar concentrator for concentrator photovoltaic system. *Renew Energy* 2009;**34**:1364–1370. doi:10.1016/j.renene.2008.09.001

[9] Chong KK, Wong CW, Siaw FL, Yew TK. Solar flux distribution analysis of Non-Imaging Planar Concentrator for the application in concentrator photovoltaic system. Conf. Rec. IEEE Photovolt. Spec. Conf., 2010;**132**:3013–3018. doi:10.1109/PVSC.2010.5614112

[10] Chong KK, Wong CW, Yew TK, Tan MH. Solar Concentrator Assembly. US Patent, Application no: 13/901,519 (pending) filed on 23rd May 2013.

[11] Chong KK, Wong CW, Yew TK, Tan MH. Dense-array concentrator photovoltaic system utilizing non-imaging dish concentrator and array of crossed compound parabolic concentrators. US Patent, Application no: 14/462,891 (pending) filed on 19th August 2014.

[12] Wong CW, Chong KK, Tan MH. Performance optimization of dense-array concentrator photovoltaic system considering effects of circumsolar radiation and slope error. Optics Express 2015;**23**:A841-A857.

[13] Yew TK, Chong KK, Lim BH. Performance study of crossed compound parabolic concentrator as secondary optics in non-imaging dish concentrator for the application of dense-array concentrator photovoltaic system. *Sol Energy* 2015;**120**:296-309.

[14] Siaw FL, Chong KK, Wong CW. A comprehensive study of dense-array concentrator photovoltaic system using non-imaging planar concentrator. *Renew Energy* 2014;**62**:542-555.

[15] Chong KK, Lau SL, Yew TK, Tan PCL. Design and development in optics of concentrator photovoltaic system. *Renew and Sustainable Energy Reviews* 2013;**19**:598-612.

[16] Tan MH, Chong KK, Wong CW. Optical characterization of nonimaging dish concentrator for the application of dense-array concentrator photovoltaic system. *Applied Optics* 2014; **53**:475-486.

[17] Tan MH, Chong KK. Influence of self-weight on electrical power conversion of dense-array concentrator photovoltaic system. *Renew Energy* 2015;**87**:445–457.

[18] Chong KK, Wong CW, Siaw FL, Yew TK. Optical characterization of nonimaging planar concentrator for the application in concentrator photovoltaic system. *Journal of Sol Energy Engineering* 2010;132:011011.

[19] ASGH Mirror Workshop. The Cassegrain Project; 2012. Available online at: http://mirrorworkshop.mtbparker.com/cassegrainStory.html

[20] Lim Y, Ahmad MH. Daylighting as a sustainable approach for high-rise office in tropics. *Intl J Real Estate Studies* 2013;**8** (1):31-42

[21] Golden DRAGON plus Datasheet Version 1.1, LUW W5AM. *OSRAM Opto Semiconductors GmbH* 2015, viewed 5 April 2016. Available online at: http://www.osram-os.com/Graphics/XPic9/00197237_0.pdf/LUW%20W5AM%20-%20GD%20PLUS%20WHITE%20(EnglishDeutsch).pdf.

Biography

Onubogu Nneka Obianuju is a 1st class Mechanical Engineering graduate of Coventry University, United Kingdom (2012) who is now pursuing her Master's Degree (By Research) at Lee Kong Chian Faculty of Engineering and Science; Universiti Tunku Abdul Rahman, Sungai Long Campus, Malaysia under a project supervised by Prof. Kok-Keong Chong.

Kok-Keong Chong received B.Sc. (Hons) in Physics from University of Malaya in 1998 and Ph.D. (Optical Engineering) degree from Universiti Teknologi Malaysia in 2002. His research interests includes concentrating solar power, solar cell technology, renewable energy and energy efficiency etc.

APPENDIX F

Design and construction of active daylighting system using two-stage non-imaging solar concentrator

ARTICLE IN PRESS

Applied Energy xxx (2017) xxx–xxx

Contents lists available at ScienceDirect

Applied Energy

journal homepage: www.elsevier.com/locate/apenergy

Design and construction of active daylighting system using two-stage non-imaging solar concentrator

Kok-Keong Chong *, Nneka Obianuju Onubogu, Tiong-Keat Yew, Chee-Woon Wong, Woei-Chong Tan

Lee Kong Chian Faculty of Engineering and Science, University Tunku Abdul Rahman, Jalan Sungai Long, Bandar Sungai Long, 43000 Kajang, Selangor, Malaysia

HIGHLIGHTS

- 2S-NISC has low rim angle, high tolerance to pointing error, uniform illumination.
- A reflective area of 0.2 m^2 is capable of illuminating an office area of 7.8 m^2.
- Average solar concentration ratio is 66.6 suns with standard deviation 3.0 suns.
- Power conversion efficiency of 2S-NISC prototype with the area of 0.2 m^2 is 22%.
- For interest rate 4% and fuel inflation rate 2%, payback period is 6.1 years.

GRAPHICAL ABSTRACT

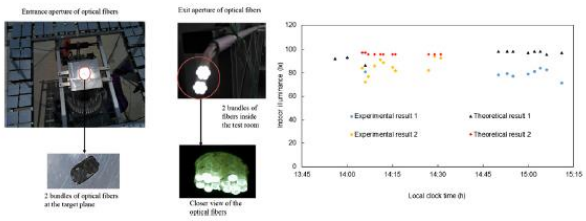

ARTICLE INFO

Article history:
Received 23 January 2017
Received in revised form 18 May 2017
Accepted 31 May 2017
Available online xxxx

Keywords:
Daylighting
Non-imaging solar concentrator
Uniform illumination
Optical fiber
Indoor illuminance

ABSTRACT

Since lighting accounts for 20% of global electricity consumption in buildings, daylighting system is an important solution to achieve energy savings in lighting and to reduce carbon dioxide emissions. However, most of the existing fiber-optics daylighting systems are expensive, sensitive to pointing error and complicated in optical design in which multi-stage focusing devices are needed to minimize non-uniformity of focused sunlight. To overcome the aforementioned problems, we propose a novel active daylighting system using two-stage non-imaging solar concentrator (2S-NISC) inspired by our previous experience in non-imaging optics. The 2S-NISC prototype consists of 80 primary facet mirrors with a dimension of 5 cm × 5 cm each, 20 secondary facet mirrors with a dimension of 8 cm × 8 cm each, and densely packed plastic optical fibers as a daylight distribution system. Considering the input solar power of 170 W, the equivalent power conversion efficiency of 2S-NISC prototype is obtained as 22%. For economic analysis, the proposed active daylighting system using 2S-NISC with optimized collective area of 4 m^2 is estimated to cost USD 1231.20. Considering the interest rate of 4% and fuel inflation rate of 2%, the total payback period is determined as 6.1 years, which is reasonable because the active daylighting system can last for at least 15 years.

1. Introduction

In the world today, fossil fuels are the major sources of energy which when burned for power generation releases greenhouse gases consisted mostly of carbon dioxide (CO_2). The major concern in the overwhelming consumption of fossil fuels is the possibility of global climate change caused by increased levels of CO_2 and other greenhouse gases in the upper atmosphere. This issue has led to the search for environment-friendly solutions to sustain human activities even in illuminating buildings. It is a known fact that lighting system is one of the major energy consumptions in

* Corresponding author.
E-mail addresses: chongkk@utar.edu.my, kokkeong_c@yahoo.com (K.-K. Chong).

http://dx.doi.org/10.1016/j.apenergy.2017.05.188
0306-2619/

Please cite this article in press as: Chong K-K et al. Design and construction of active daylighting system using two-stage non-imaging solar concentrator. Appl Energy (2017), http://dx.doi.org/10.1016/j.apenergy.2017.05.188

Nomenclature

2S-NISC	two-stage non-imaging solar concentrator
NIPC	non-imaging planar concentrator
NIDC	non-imaging dish concentrator
2-D	2-dimensional
3-D	3-dimensional
POF	plastic optical fiber
L	the distance between the primary reflector and the secondary reflector
$C_{measured}$	measured solar concentration ratio
W/m^2	Watt per square meter
lx	lux
lm	lumen
Mt	million tons
kW h	kilowatt hours
MV	megavolts
MW	megawatts
TW h	terawatt hours
DNI or I	direct normal irradiance
GSI	global solar irradiance
ω	half rim angle
dB/km	decibel per km
lm/W	lumen per Watt
mrad	milliradian
CPV	concentrator photovoltaic
$I_{sc\text{-}1}$	short-circuit current under concentrated solar flux (reading from CPV cell 1)
$I_{sc\text{-}2}^{DNI}$	short-circuit current under one sun contributed by DNI only (reading from CPV cell 2)
C_{avg}	average solar concentration ratio
$\Delta C_{measured}$	measurement error of solar concentration ratio (number of suns)
$\Delta I_{sc\text{-}1}$	measurement error of short circuit current 1
$\Delta I_{sc\text{-}2}$	measurement error of short circuit current 2
V_{DNI}	DNI voltage
V_{GSI}	GSI voltage
ΔV_{DNI}	measurement error of DNI voltage
ΔV_{GSI}	measurement error of GSI voltage
$Illum_{theo}$	theoretical result of indoor illuminance
A_{fiber}	cross-sectional area of plastic optical fiber
% VL	percentage of visible light in the solar spectrum
$T_{hot\ mirror}$	transmissivity of hot mirror to visible light
L_{fiber}	total transmission loss via optical fiber
N_{fiber}	number of plastic optical fibers
E_L	the average value of direct beam luminous efficacy
A_{illum}	indoor illuminance area
R_{facet}	reflectivity of primary/secondary facet mirror

buildings to cause a large amount of CO_2 emissions even during the daytime [1]. The total CO_2 emissions attributed to lighting were estimated to be 1900 Mt, which was about 7% of the total global CO_2 emissions from flaring of fossil fuels for power generation [2,3]. Increase of energy consumption in lighting due to the rapid growth in population will continuously generate a substantial rise in greenhouse gas emissions, which justifies the necessity to encourage energy conservation in the lighting sector.

The Energy Information Administration (EIA) estimated that the residential and commercial sectors in the United States consumed about 279 billion kWh of electricity for lighting in 2016. It was about 10% of the total electricity consumed by both of these sectors and about 7% of the total electricity consumption in the United States [4]. For agricultural sector, artificial lights are widely used in various applications such as area lighting, task (packaging and processing) lighting, and to provide illumination for livestock, animal housing, poultry as well as plant growth. In the United States, electricity consumed by agricultural operations was approximately 0.14 quadrillion BTU, which was mainly driven by lighting and ventilation-related energy expenses in the livestock and greenhouse areas [5,6]. In Europe, the interiors of medium and large buildings utilize about 40% of the total electrical energy for illumination only [7]. In South Asia, lighting consumes approximately 132 TW h, which is about 15% of the total electricity consumption [8]. In Malaysia, approximately 30% of the total energy produced is consumed by lighting in buildings in which Zakaria et al. highlighted that over 40% of the carbon emissions in Malaysia are from the existing buildings and communities [9,10]. The International Energy Agency (IEA) stated that lighting accounts for around 20% of global electricity consumption in buildings [11].

Solar energy as one of the most abundant clean energy sources on earth should be fully explored to meet the energy saving demands. It has been estimated that a building with efficient daylighting system can reduce energy consumption for lighting by 50–80% in which daylighting is generally defined as introducing natural light into a building for illumination [12]. Direct use of sunlight is a more sustainable way to illuminate the interior space of a building than the indirect use of photovoltaic module for converting solar energy to electrical energy and back to light energy as the multiple conversion processes involve significant energy losses. In principle, there are two different methods of daylight harnessing for achieving green building status via energy conservation: passive daylighting system that is stationary and active daylighting system that requires sun-tracking mechanism. There are many studies on how passive and active daylighting systems can contribute in energy saving for the building. Chow et al. examined the daylighting performance towards energy saving including economic and environmental benefits for a 13-storey atrium building in Hong Kong. The total potential energy savings per year is 43,003 kW h and the average emissions of CO_2, SO_2, NO_X and particulate could be reduced annually by 32,252 kg, 440 kg, 42.4 kg and 2.1 kg respectively [13]. Galasiu et al. demonstrated that passive daylighting systems in a building could reduce the average amount of electricity consumed by 50–60% in comparison to utilizing artificial lights from 6 AM to 6 PM under a clear sky without blinds [14]. Jenkins and Newborough predicted the annual energy savings for lighting in a range of 56–62% by accounting for the daylight contribution from windows and roof lights in a six-storey office building [15]. Zain-Ahmed et al. demonstrated that the use of daylighting strategies in Malaysian buildings could achieve 10% of energy savings [16]. Elmualin et al. presented a daylighting system using dichroic material as a light pipe to transmit visible sunlight into a room, which is capable of removing approximately half of the solar heat in daylight and thereby saving electrical energy consumption for both cooling as well as lighting [17]. Berardi proved that aerogel windows can offer a solution for energy saving by providing a better distribution of daylight while reducing the solar heat gain in buildings [18]. An integrated meta-model daylighting, heating, ventilating and air conditioning system developed by Kim et al. has shown an average of 13.7% energy savings against the conventional method throughout three months of observation in winter [19]. On the other hand, Pohl and Anselm

Please cite this article in press as: Chong K-K et al. Design and construction of active daylighting system using two-stage non-imaging solar concentrator. Appl Energy (2017), http://dx.doi.org/10.1016/j.apenergy.2017.05.188

demonstrated how an active daylighting system using heliostats with supplementary fluorescent lamps allow power savings of 40–60% as compared to a conventional electric lighting system based on their measurement results [20]. More so, Ullah and Whang verified that a hybrid system consisted of Light Emitting Diodes (LED) and a bundle of optical fibers connected to a parabolic concentrator can save an average electrical lighting energy of 50% [21]. Ghisi and Tinker evaluated that the integration of active daylighting and artificial lighting system can potentially save energy ranging from 8% to 82.3% for seven cities in Brazil and ranging from 56.0% to 89.2% for one city in the UK based on climatic data [22].

From past studies on active daylighting systems, various kinds of conventional concentrators i.e. Fresnel lens, heliostat, parabolic concentrator, compound parabolic concentrator, etc., were deployed to concentrate sunlight, and optical fibers were used to distribute the daylight throughout the building [23–28]. Ullah and Shin proposed a novel approach of the daylighting system by guiding highly concentrated sunlight via optical fibers to illuminate the interior space of a large-scale multi-floor building [23]. Their proposal is complicated in optical design cum expensive in cost with the requirement of three stage line focused optical system that includes primary concentrator as a parabolic trough or Linear Fresnel lens, secondary concentrator as a parabolic reflector or collimating plano-concave lens and tertiary concentrator as a trough compound parabolic concentrator [23]. For point focus solar concentrator, Song et al. proposed an active daylighting system with high accuracy dual axis sun-tracking system wherein their system was comprised of five lenses (100 mm in diameter) for sunlight focusing and optical fibers (10 m in length & 2 mm in diameter) for daylight transmission [24]. Nevertheless, this design is complicated because it requires high tracking accuracy with the pointing error of less than 0.07° in order to maintain the loss at 14%. Both Muhs [25] and Schelegel et al. [26] analyzed an integrated hybrid lighting system that uses a two-axis tracking parabolic dish concentrator with cold mirrors. Albeit the components of this system are commercially available, it is still expensive to be constructed with a cost of USD 3000 for a collective area of 2 m^2 [25]. Similarly, Sapia [27] presented a daylighting system composed of a sun-tracking primary parabolic collector and a secondary collector (cold mirrors). The total expected cost of the proposed system is as high as 6538 euros for a parabolic collector with a diameter of 2.6 m.

Theoretical modeling plays a vital role in evaluating the optical performance of active daylighting systems. Most of the existing theoretical modeling for daylighting systems were implemented using LightTools software [23,28,29,30]. LightTools is an optical simulation tool used to design the optical components of an active daylighting system and to estimate the illuminance levels in the interior space. On the other hand, Ullah and Shin [23] designed the illuminance level of a room using software called DIALux, which is a 3-D design program where real lighting effects can be created in a room, street or an open-air area.

For cost effectiveness, non-imaging focusing technologies have been deployed in the application of concentrator photovoltaic (CPV) system and solar furnace system, which can be grouped based on the nature of sun-tracking manners: on-axis tracking configuration [31–41], and off-axis tracking configuration [42–52]. There are several merits of adopting non-imaging optics in a large solar concentrator with segmented mirror facets for the application in active daylighting system. The focused image of a non-imaging optical device can be tailored to accommodate different receiver designs in both shape and dimension by producing uniform illumination. Additionally, the multi-faceted design of a non-imaging solar concentrator allows a flexibility to increase the focal distance and thus to reduce the rim angle. Inspired by the aforementioned advantages, we propose a two-stage non-imaging solar concentrator (2S-NISC) consisted of primary and secondary reflectors for application in active daylighting system. The primary reflector is comprised of many flat facet mirrors designed to track the sun and to collect the incident sunrays. The secondary reflector is also comprised of flat facet mirrors positioned above the primary reflector to reflect the sunrays from the primary reflector towards the receiver at the center of the solar concentrator where the optical fibers are located. The double reflections design can minimize the bending angle of optical fibers, which can distribute the daylight throughout the building with the least light leakage especially for locations beyond the reach of any window. This idea is novel and original because it is the first design of active daylighting system using non-imaging focusing technology. To prove the feasibility of the idea, we also report on the practical implementation and economic assessment of the newly proposed active daylighting system in this paper. Our design has great potential to serve as an alternative active daylighting solution based on the following advantages: (1) The optical design of 2S-NISC has low rim angle, which is important for effective collimation of daylight towards the desired area by reducing wastage through illuminating undesired areas such as walls. Besides, it also minimizes the coupling loss between the solar concentrator and optical fiber. (2) Non-imaging solar concentrator only use flat facet mirrors as reflectors, which makes the manufacturing and assembling processes simpler as compared to other concentrators such as the parabolic dish, Fresnel lens, parabolic troughs. (3) Since 2S-NISC concentrates sunlight by superposing all solar images of flat facet mirrors into one, the incident angles of solar rays cast by any individual facet mirror are constant across the receiver and dependent on the position of the facet mirror. It makes the light transmission loss in the fiber less sensitive to pointing error of the sun-tracking system as compared to parabolic dish or Fresnel lens. (4) Finally, the proposed 2S-NISC is capable of producing uniform illumination of concentrated sunlight, which is highly required by daylighting systems.

2. Design and construction of prototype

2.1. Prototype of two-stage non-imaging solar concentrator (2S-NISC)

The 3-D designs of the primary and secondary reflectors were made in the platform of SolidWorks as shown in Fig. 1(a), where *L* is the distance between the primary and the secondary reflectors, 70 cm. All the facet mirrors were modeled in LightTools (optical simulation software) according to their respective tilting angles to perform optical analysis. Fig. 1(b) illustrates the schematic diagram of the 2S-NISC prototype to show how the sunrays are focused onto the input aperture of the optical fibers in 3-D view. Fig. 1(c) shows all mirror assembly sets and their counterpart secondary facet mirrors labeled with numbers, where the same number means that the specific mirror assembly set will superpose all their solar images to the target via its corresponding secondary facet mirror.

2.2. 3-D optical design and simulation result

LightTools software based on 3-D ray-tracing method was used to analyze the solar flux distribution of the 2S-NISC prototype with the specification as listed in Table 1. In the theoretical study, we assume that the solar irradiance of sunlight incident on the primary facet mirror is 1000 W/m^2 (or equivalent to 1 sun) and all the facet mirrors have perfect reflectance. Besides, a light source with a dimension slightly larger than the dimension of the 2S-NISC prototype is generated to emulate sunrays with the solar disc half angle of 4.65 mrad. It is important to guarantee that the ray-tracing process has covered the entire primary reflector of

Please cite this article in press as: Chong K-K et al. Design and construction of active daylighting system using two-stage non-imaging solar concentrator. Appl Energy (2017), http://dx.doi.org/10.1016/j.apenergy.2017.05.188

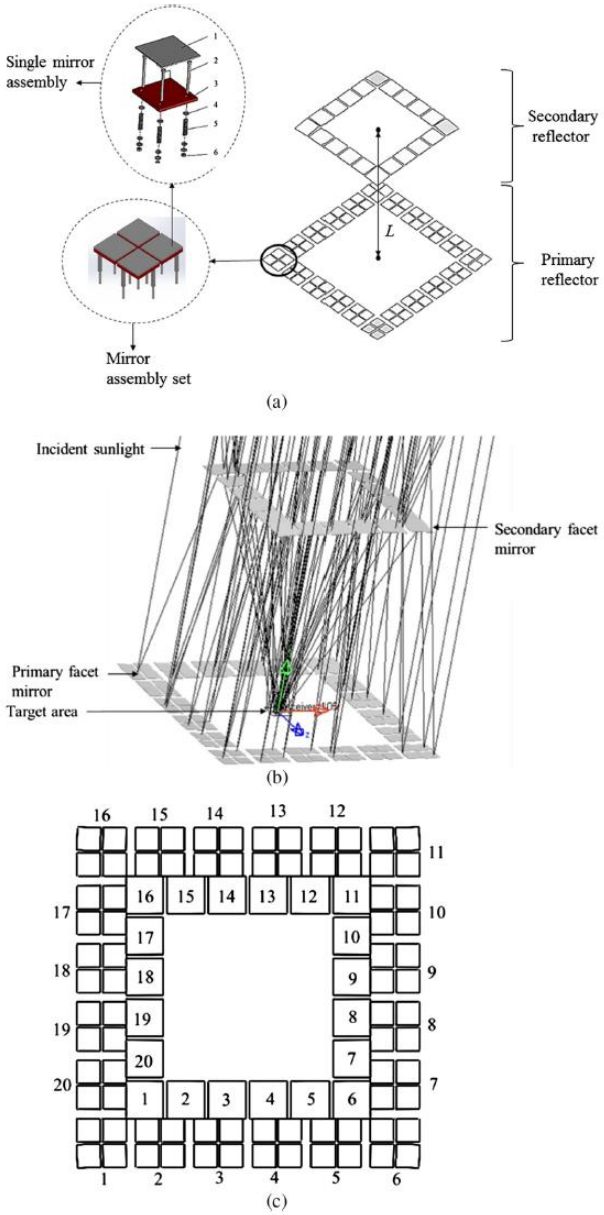

Fig. 1. (a) 3-D configuration of the primary and secondary reflectors in SolidWorks; (b) 3-D view to show the numerical modeling of 2S-NISC using ray-tracing technique; (c) Top view to show the arrangements of primary and secondary facet mirrors: all mirror assembly sets and their counterpart secondary facet mirrors labeled with numbers. The same number means that the specific mirror assembly set will superpose all their solar images to the target via its corresponding secondary facet mirror.

Please cite this article in press as: Chong K-K et al. Design and construction of active daylighting system using two-stage non-imaging solar concentrator. Appl Energy (2017), http://dx.doi.org/10.1016/j.apenergy.2017.05.188

Table 1
Specifications and design parameters for the prototype of two-stage non-imaging solar concentrator (2S-NISC).

Number of mirror assembly sets in primary reflector	20
Number of primary facet mirrors per mirror assembly set	4
Number of secondary facet mirrors in the secondary reflector	20
Dimension of primary facet mirror	5 cm × 5 cm × 0.2 cm (thickness)
Dimension of secondary facet mirror	8 cm × 8 cm × 0.2 cm (thickness)
Dimension of mirror assembly set	10.5 cm × 10.5 cm
Gap between primary facet mirrors in mirror assembly set	0.5 cm
Gap between two adjacent mirror assembly sets	2 cm
Gap between two adjacent secondary facet mirrors	0.8 cm
Dimension of primary reflector frame	73 cm × 73 cm
Dimension of secondary reflector frame	52 cm × 52 cm
Reflective area of primary reflector	0.2 m^2
Reflective area of secondary reflector	0.13 m^2
Perpendicular distance between primary and secondary reflectors	70 cm
Half rim angle of 2S-NISC	24°
Total height of 2S-NISC	1.53 m
Total weight of 2S-NISC	42.2 kg
Model of plastic optical fiber	CK-120
External diameter of plastic optical fiber	3 mm
Total length of plastic optical fiber	10 m

the 2S-NISC in the simulation. Since the central region of the secondary reflector is an empty space, there are direct sunrays incident on the receiver without going through any reflector. For each simulation, 20 million rays were traced for achieving a reasonably good resolution in the solar flux distribution plot. Fig. 2 (a) depicts the simulated result of focused image formed at the receiver plane without pointing error. The simulated solar flux distribution is viewed as a flat top region with average solar concentration ratio (C_{avg}) of 76 suns in the central region covering the area of 38 mm × 38 mm and gradually decreasing towards the edge to form a total focused image size of 65 mm × 65 mm. The percentage of energy within the uniform illumination area is 57.3% in which the average solar concentration ratio of 76 suns is mainly contributed by the solar concentrator (75 suns) and direct sunlight (1 sun). The percentage of energy is increased to 74.6% for C_{avg} of more than 60 suns, and the percentage of energy is 88.7% for C_{avg} of more than 38 suns. In Fig. 2(b), the spillage loss versus receiver dimension was plotted to analyze the optimal dimension of the target area. Lastly, the target dimension of 50 mm × 50 mm (the same size as the primary facet mirror) was selected due to low spillage loss (11.6%). With reasonably good uniformity of solar flux distribution produced by the 2S-NISC, it is highly recommended for active daylighting application. The solar flux distribution contributed by the reflector is inevitably spread over a larger area with solar concentration ratio on the target area lesser than that of the number of primary facet mirrors due to both the cosine loss and

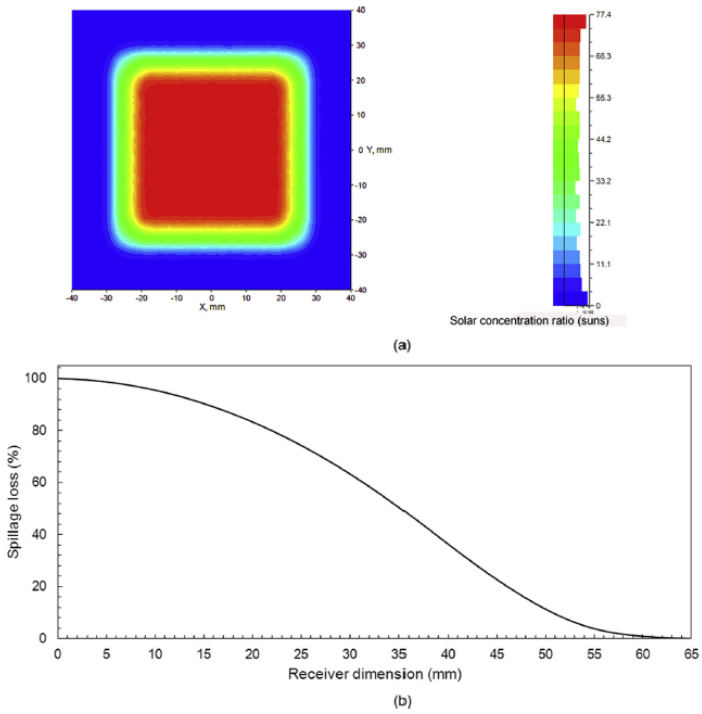

Fig. 2. 2-D plot of simulated result showing solar flux distribution at the target area of the two-stage non-imaging solar concentrator (2S-NISC) prototype and (b) graph of spillage loss versus receiver dimension.

Please cite this article in press as: Chong K-K et al. Design and construction of active daylighting system using two-stage non-imaging solar concentrator. Appl Energy (2017), http://dx.doi.org/10.1016/j.apenergy.2017.05.188

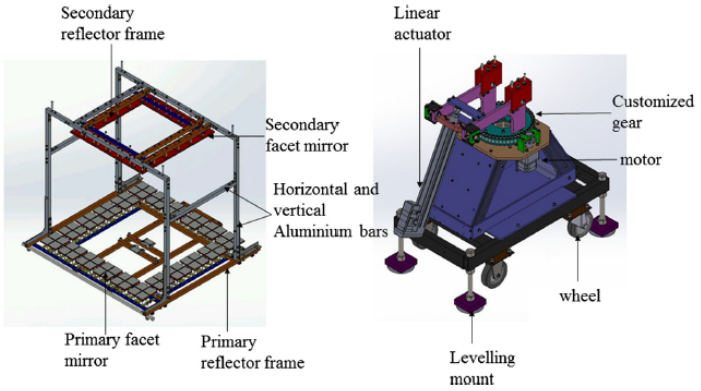

Fig. 3. (a) 3-D drawing of the mechanical frame of the 2S-NISC prototype with reflector in SolidWorks; (b) 3-D drawing of the base structure of the 2S-NISC prototype with sun-tracking mechanism in SolidWorks.

solar disc effect. This numerical result will be used to compare with the experimental result.

2.3. Prototype of two-stage non-imaging solar concentrator (2S-NISC)

For on-site data collection, the 2S-NISC prototype was constructed on the rooftop of the building in Universiti Tunku Abdul Rahman located at a longitude of 101.79° and latitude of 3.04°. The mechanical structure of the 2S-NISC prototype can be categorized into two parts: a mechanical frame with reflectors as shown in Fig. 3(a), and the base structure with the sun-tracking mechanism as shown in Fig. 3(b).

The mechanical frame was manufactured using 2 cm × 2 cm aluminum hollow square bars of 2 mm thickness due to its superior characteristics including lightweight and corrosion resistance. For the primary reflector frame, two aluminum hollow bars with a distance of 8.5 cm apart joined at the edges to form a square frame were used to support the primary mirror assembly set. Then, PVC plate was cut into rectangular shapes to have a dimension of 12.5 cm × 1 cm × 0.5 cm (thickness) and was fixed across the two aluminum hollow bars so that the primary facet mirrors can be fixed on it using bolts & nuts. Similarly, the mechanical frame of the secondary reflector was prepared using two aluminum hollow bars with a distance of 6 cm apart to support the facet mirrors on each side of the square frame. Four aluminum hollow bars were used to join between the primary reflector frame and the secondary reflector frame.

Eighty flat facet mirrors with a dimension of 5 cm × 5 cm × 0.2 cm (thickness) were fixed on the primary reflector frame to form a total of twenty mirror assembly sets as illustrated in Fig. 1(a). The gap between two primary facet mirrors within each mirror assembly set was 0.5 cm while two mirror assembly sets were separated apart by 2 cm. Each facet mirror consisted of six parts as shown in Fig. 1(a), i.e. (1) flat mirror, (2) three bolts (M4 × 60 mm), (3) PVC plate (mirror frame), (4) washers (5) compression spring (6) nuts. There were three contact points for each facet mirror via the bolt-spring assemblies in which one of them acted as the pivot point and the remaining two were adjustable. Therefore, each facet mirror can be tilted freely by manually turning the nuts of the adjustable bolt-spring sets to align the solar image towards the target. Silicone paste was used to join the facet mirror to the PVC plates (mirror frame), which can provide stability to the mirror position after alignment.

The base structure was made of mild steel bars and plates in order to support the entire weight of the mechanical frame. A door beneath the pedestal was made of 0.2 cm thick PVC plates to house all electronic components of the 2S-NISC prototype. Custom-made connectors were fixed on the top most part of the solar concentrator base structure for connecting the mechanical frame. Four wheels were fixed underneath the base structure for easy movement of the 2S-NISC prototype. Four adjustable leveling mounts were also attached to the base for stability when the prototype was positioned on the rooftop during operation.

The sun-tracking mechanism of the 2S-NISC prototype was installed on the base structure to ensure good rigidity. Azimuth driving mechanism was comprised of a stepper motor connected to a sprocket gear engaged with a custom-made gear (multiple screws on two rotating circular hollow plates) for transmitting azimuth movement to the mechanical frame in 360°. The hollow space at the central region of the custom-made gear can minimize the bending angle of the optical fibers from the target area to the test room. The elevation driving mechanism was a linear actuator fixed to the mechanical frame via a shaft to perform elevation motion from 0° to 50°. Before a decision was made for the linear actuator as well as its optimal position in the mechanical structure, Finite Element Analysis (FEA) was carried out to determine the minimum force required for moving the mechanical frame up and down.

The 2S-NISC prototype can track the sun in a dual-axis motion. The latest version of the Arduino MEGA 2560 is used as a platform to host our sun-tracking program for implementing the control system. The sun-tracking system is designed as a structural closed-loop control system, and the feedbacks of the rotational angles about azimuth and elevation axes are carried out by using two 9-bit absolute encoders with a resolution of 512 counts/revolution or equivalent to 0.70° per count. At first, the sun-tracking algorithm calculates azimuth and elevation angles according to the date, local clock time, standard time zone and latitude and longitude of the site location before sending control pulse and interrupt signals to the driving mechanism in repeated loops. Then, the calculated elevation and azimuth angles are compared with the current positions of the solar concentrator to obtain a differential value in position. If the positional difference in angular degree is greater than the resolution of the optical encoder, i.e. 0.70°, the program will command the relevant stepper motor to move the solar concentrator to the latest calculated position. The specification of the 2S-NISC prototype is listed in Table 1. The weight of the mechanical frame

Please cite this article in press as: Chong K-K et al. Design and construction of active daylighting system using two-stage non-imaging solar concentrator. Appl Energy (2017), http://dx.doi.org/10.1016/j.apenergy.2017.05.188

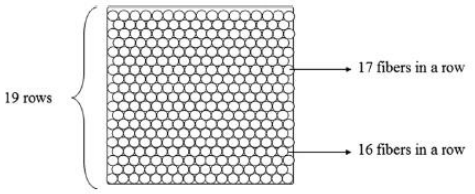

Fig. 4. Arrangement of optical fibers on the target plane with area of 50 mm × 50 mm.

including reflectors is 16 kg and the weight of the entire 2S-NISC prototype including the driving mechanism is 42.2 kg. The dimension of the mechanical frame is 91 cm × 81 cm.

2.4. Solar daylighting system using 2S-NISC prototype

High-performance plastic optical fibers (POF) with model CK-120 were selected because of its cost effectiveness, flexibility and large core diameter that can transmit more light via total internal reflection. Each plastic fiber consisted of a core made of polymethylmethacrylate (PMMA) and cladding made of fluorinated Polymer. The core diameter of the POF was 2.945 mm with the external diameter of 3 mm including the cladding. The entrance aperture of the optical fibers was fixed at the central region of the primary reflector to face the sun perpendicularly in order to minimize the bending angle of the optical fibers and thus reduce bending losses during daylight transmission. The half acceptance angle of the PMMA is 30° (total acceptance angle = 2 × 30°); where the half acceptance angle is defined as the maximum angle relative to the central axis of the optical fiber at which the light rays can enter and transmit through the optical fiber. It is also indicated that the maximum emitting angle of the light rays at the exit of the optical fiber would also be the same as the half acceptance angle.

To prevent melting and downgrading of the POF after a long exposure time under concentrated sunlight, a hot mirror filter is placed just before the entrance aperture of the fibers to filter away an average of 98% of infrared ray and an average of 70% of ultraviolet light (below 380 nm and above 710 nm). The hot mirror has a

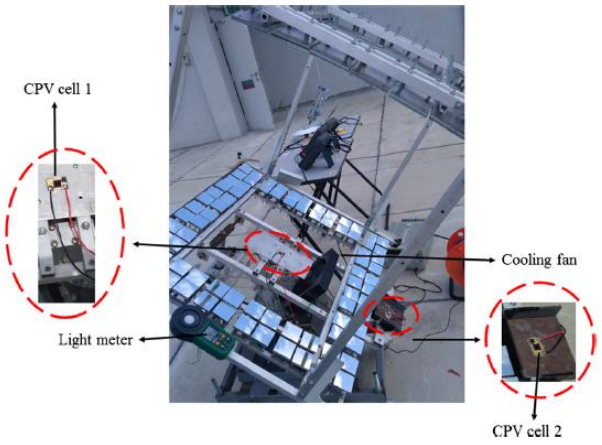

Fig. 5. Experimental setup to measure the solar concentration ratio of the two-stage non-imaging solar concentrator (2S-NISC) by using CPV cells.

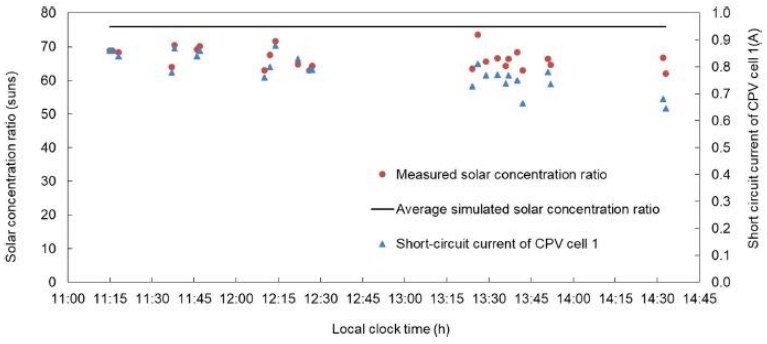

Fig. 6. Graph to show the relationship of short-circuit current of CPV cell 1 and solar concentration ratio (measured and simulated results) versus local clock time on 14th December 2016.

Please cite this article in press as: Chong K-K et al. Design and construction of active daylighting system using two-stage non-imaging solar concentrator. Appl Energy (2017), http://dx.doi.org/10.1016/j.apenergy.2017.05.188

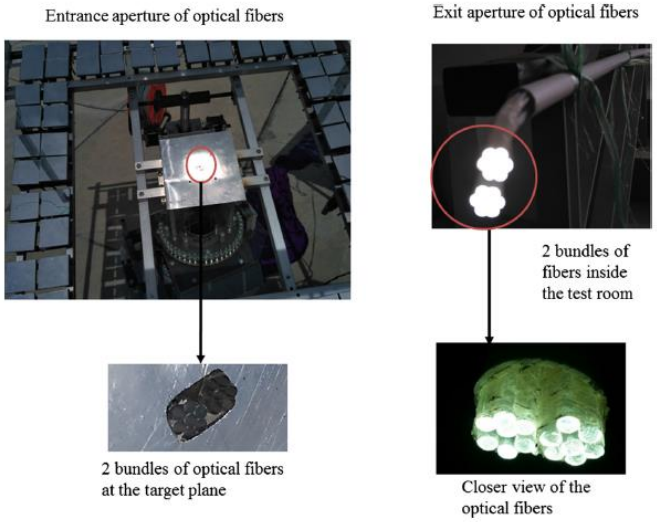

Fig. 7. Experimental setup to measure the indoor illuminance produced by the active daylighting system consisted of two-stage non-imaging solar concentrator (2S-NISC) and two bundles of optical fibers with total length of 10 m.

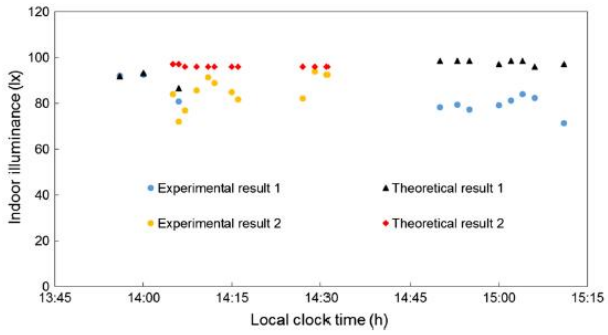

Fig. 8. Graph to show a comparison between theoretical and experimental results for the indoor illuminance of the active daylighting system versus local clock time on 30th December 2016 and 16th February 2017.

high transmissibility of 98% for visible light. To protect the fibers from scratches, dust and dirt, they are neatly inserted inside a black foam embraced by insulated pipe.

The optimized target area in which the POFs were located in the prototype of the solar concentrator is $50 \times 50\ mm^2$ and Fig. 4 shows that this optimized area can accommodate 314 optical fibers for indoor illumination. From the calculations as shown in Table 2, the prototype is expected to deliver 8143.2 lm of daylight to the optical fibers.

Based on the known average solar flux distribution, we can calculate the average lumen that one optical fiber can transmit. Since the cross-sectional area of each optical fiber is $\pi \times (1.5\ mm)^2 = 7.07\ mm^2$, one fiber can transmit an average of $(7.07\ mm^2 \times 8143.2\ lm)/2500\ mm^2 = 23$ lm. For an optical fiber with a length of 10 m, we have calibrated the incurred transmission and coupling losses as 45.7% through cutback technique. Thus, the average lumen emerging at the exit aperture of 10 m length optical fiber is expected as (23 lm × 54.3%) = 12.49 lm.

For daylighting via optical fiber in a standard office area of $6.3\ m^2$, the lumens required to achieve 500 lx (standard illuminance for visibility) is 3150 lm and therefore the total number of optical fibers needed is $3150/12.49 \approx 252$ fibers. As shown in Fig. 4, the target area can accommodate 314 optical fibers, which can supply an average luminous flux of 12.49 lm × 314 = 3921.9 lm (or 622.5 lux for office area of $6.3\ m^2$). Theoretically, we can accomplish more than the required illuminance value for a standard office area with our prototype. If an average illuminance of 500 lux is required, the average illuminance of our prototype design with 622.5 lux for a space of $6.3\ m^2$ can be used to illuminate a bigger office area of $(622.5\ lux \times 6.3\ m^2)/500\ lux = 7.8\ m^2$.

Please cite this article in press as: Chong K-K et al. Design and construction of active daylighting system using two-stage non-imaging solar concentrator. Appl Energy (2017), http://dx.doi.org/10.1016/j.apenergy.2017.05.188

Table 2
Design specifications for the prototype of active daylighting system using two-stage non-imaging solar concentrator (2S-NISC).

Parameters	Value	Parameters	Value
Area of each primary facet mirror (cm^2)	25	Direct normal irradiance (DNI), I (W/m^2)[*5]	1000
Number of primary facet mirrors	80	Percentage of visible light in solar spectrum, %*VL* (%)[*6]	47
Total area of all primary facet mirrors, $A_{Reflector}$ (m^2)	0.2	Percentage of infrared light in solar spectrum (%)	46
Target area (m^2) (0.05 m × 0.05 m)[*1]	0.0025	Percentage of ultraviolet light in solar spectrum (%)	7
Transmissibility of visible light for hot mirror[*2]	0.98	Uniform illumination area of concentrated flux, $A_{uniform}$ (mm^2) = (38 mm × 38 mm)[*7]	1444
Core reflective index of POF	1.49	Average solar concentration ratio within the target area of 50 mm × 50 mm (suns)[*8]	68
Numerical aperture of POF	0.50	Input solar power within the target area of 50 mm × 50 mm (W) = (68 × 1000 × 0.0025)	170
Maximum operating temperature of POF (°C)	70	Visible light power as 47% of full solar spectrum (W) = 170 W × 0.47	79.9
Minimum operating temperature of POF (°C)	−55	Input light power after the hot mirror filter (W) = 79.9 W × 0.98	78.3
Length of POF (m)	10	Illuminance (lm) = luminous efficacy × input light power = 104 lm/W × 78.3 W	8143.2
Half acceptance angle of POF (°)	30		
Average value of direct beam luminous efficacy (lm/W) as provided by Lim and Ahmad based on Malaysian climate [53][*3]	104		
Transmission loss of POF (dB/km)	≤200		
Total transmission loss via fiber, L_{fiber} (%)[*4]	45.7		

Note: The parameters and values with * are very important in the calculation and are explained as follows:

[*1] The target area is the area where sunlight is focused onto by the solar concentrator and it is also fully covered by the input apertures of the optical fibers.

[*2] A hot mirror is a dielectric mirror that reflects infrared and ultraviolet portions of sunlight but allows visible light to pass through. Thereby, it is important to protect the bundle of optical fibers from overheating that can cause the plastic fiber to melt or burn. The transmissibility of hot mirror for visible light is as high as 98%.

[*3] Direct beam luminous efficacy is the ratio of daylight illuminance to solar irradiance measured in the unit of lumens per Watt (SI unit). The average value in Malaysia is 104 lm/W.

[*4] Transmission loss of plastic optical fiber is the light power loss in exponential rate with distance as the light travels along the plastic optical fiber. The amount of loss is quantified in the unit of dB/km.

[*5] Direct normal irradiance (DNI) is the direct component of solar power reaching the earth per square meter. The standard value of DNI is given as 1000 W/m^2.

[*6] Visible light is only a portion of the solar spectrum that is visible to the human eye, which is 47%.

[*7] Uniform illumination area of concentrated flux is the area in the central region of the solar flux distribution in which solar concentration ratio is almost constant. It can happen because this region has all the solar images of the flat facet mirrors overlapped perfectly.

[*8] Average solar concentration ratio is the average solar irradiance integrated over the target area of 5 cm × 5 cm divided by the solar irradiance incident on the collector aperture. From the numerical simulation result using LightTools, we can obtain the value of average solar concentration ratio as 68 suns.

To supplement the intermittent daylighting especially when illumination is less than the required level, light-emitting diodes (LEDs) with model no. LUW W5AM-KYLX-4E8G are proposed as complementary artificial light source because they consume less power and have a long lifetime. It is a high power LED with a white light source at color temperature of 5700 K, which is in the similar range of daylight ranging from 5000 K to 6000 K. As stated in the datasheet [54], each of the LEDs can produce 104 lm/W with the forward voltage (V_f) of 3.2 V, current of 350 mA and electrical input power of 1.12 W. For the LEDs to fully illuminate an office area of 7.8 m^2, we need 3921.9 lm to achieve 500 lx and hence a total of 34 LEDs with rated electrical power of 37.7 W is required. It means that the total illuminance produced by our active daylighting prototype is equivalent to 34 LEDs with 1.12 W each. Considering the input solar power of 170 W collected by the prototype (refer to Table 2), the equivalent power conversion efficiency can be calculated as (37.7 W/170 W) × 100% = 22%.

3. Results and discussion

3.1. Experimental result

The experimental setup for measuring solar concentration ratio of 2S-NISC prototype is revealed in Fig. 5. The following instruments were employed: multimeter 1 – to measure the short-circuit current of CPV cell 1 that is placed under concentrated sunlight (I_{sc-1}), multimeter 2 – to measure short-circuit current of CPV cell 2 that is placed under one sun (I_{sc-2}), a digital light meter fixed on the mechanical frame - to measure illuminance of sunlight, a pyranometer – to measure global solar irradiance (GSI), and a pyrheliometer – to measure the direct normal irradiance (DNI). To ensure accurate measurement, all instruments were tilted to face the sun perpendicularly at all times.

For the measurement under one sun, the short-circuit current of CPV cell 2 contributed by DNI only (I_{sc-2}^{DNI}) can be calculated using the following equation:

$$I_{sc-2}^{DNI} = I_{sc-2} \times \frac{DNI}{GSI} \tag{1}$$

where I_{sc-2} is the measured short-circuit current of CPV cell 2 (mA) exposing to GSI under one sun, DNI is the direct normal irradiance measured by the pyrheliometer (W/m^2) and GSI is the global solar irradiance measured by the pyranometer (W/m^2).

After obtaining both I_{sc-2}^{DNI} and I_{sc-1}, the measured solar concentration ratio of 2S-NISC prototype, $C_{measured}$, can be computed using the following equations:

$$C_{measured} = \frac{I_{sc-1}}{I_{sc-2}^{DNI}} \tag{2}$$

$$C_{measured} = \frac{I_{sc-1}}{I_{sc-2}} \times \frac{GSI}{DNI} \tag{3}$$

where I_{sc-1} is the measured short-circuit current of CPV cell 1 (A) exposing to the concentrated sunlight that is located at the central region of the receiver.

To measure the solar concentration ratio of the 2S-NISC prototype, readings were taken during a sunny day with some clouds in the sky for local clock time from 11:15 h to 14:33 h on 14th December 2016 and all the data are listed in Table 3. Fig. 6 shows the relationship of measured solar concentration ratio and the short-circuit current of CPV cell 1 under high concentrated sunlight versus local clock time as compared to the simulated solar concentration ratio. The measured solar concentration ratio of the 2S-NISC prototype fluctuated between 62 suns and 74 suns throughout the period of measurement. The variation is attributed to random error during measurement of short-circuit currents from CPV cell 1 and

Please cite this article in press as: Chong K-K et al. Design and construction of active daylighting system using two-stage non-imaging solar concentrator. Appl Energy (2017), http://dx.doi.org/10.1016/j.apenergy.2017.05.188

Table 3
Data collection on 14th December 2016 for the short-circuit currents of CPV cell 1 and 2, GSI, DNI, measured and uncertainty of solar concentration ratio at the receiver of the two-stage non-imaging solar concentrator (2S-NISC) prototype.

Local time (h)	GSI (W/m^2)	DNI (W/m^2)	DNI/GSI ratio	I_{sc-2} (mA)	I_{sc-1} (A)	Measured solar concentration ratio (suns)	Uncertainty of measured solar concentration ratio, $C_{measured}$ (suns)
11:15	1022	912	0.89	13.99	0.86	68.8	±1.4
11:16	1022	912	0.89	13.98	0.86	68.9	±1.4
11:18	1034	900	0.87	14.10	0.84	68.4	±1.4
11:37	1107	888	0.80	15.19	0.78	64.0	±1.3
11:38	1144	900	0.79	15.67	0.87	70.5	±1.4
11:46	1192	888	0.74	16.30	0.84	69.2	±1.4
11:47	1192	900	0.76	16.25	0.86	70.1	±1.4
12:10	1204	888	0.74	16.35	0.76	63.1	±1.3
12:12	1180	888	0.75	15.73	0.80	67.6	±1.4
12:14	1229	925	0.75	16.33	0.88	71.6	±1.5
12:22	1156	925	0.80	16.00	0.83	64.8	±1.3
12:26	1204	925	0.77	16.33	0.79	63.0	±1.3
12:27	1192	912	0.77	16.04	0.79	64.4	±1.3
13:24	1119	863	0.77	14.88	0.73	63.4	±1.3
13:26	1119	851	0.76	14.51	0.81	73.6	±1.5
13:29	1119	863	0.77	15.20	0.77	65.6	±1.3
13:33	1095	838	0.77	15.13	0.77	66.5	±1.4
13:36	1046	826	0.79	14.56	0.74	64.3	±1.3
13:37	1034	826	0.80	14.50	0.77	66.4	±1.4
13:40	998	789	0.79	13.88	0.75	68.4	±1.4
13:42	985	764	0.78	13.62	0.67	62.9	±1.3
13:51	1058	838	0.79	14.88	0.78	66.3	±1.4
13:52	1046	814	0.78	14.66	0.74	64.5	±1.3
14:32	985	715	0.73	14.06	0.68	66.7	±1.4
14:33	985	727	0.74	14.12	0.65	62.1	±1.3

2, which can be caused by several factors including temperature variation of CPV cell, the accuracy of sun-tracking and measurement error of the multimeter (±1.2% for current and ±0.8% for voltage). From the average measured solar concentration ratio of 66.6 suns with a standard deviation of 3.0 suns and the simulated average solar concentration ratio of 76 suns, the reflectivity of the facet mirror can be estimated as $\sqrt{\frac{66.6-1}{76-1}} = 0.935$. (Note: we subtract one sun in the formula because the direct sunlight from the central region of the secondary reflector does not affect the reflectivity of the facet mirrors).

The uncertainty of measured solar concentration ratio ($\Delta C_{measured}$) is dependent on the measurement error of the short-circuit current of CPV cell 1 (ΔI_{sc-1}), measurement error of the short-circuit current of CPV cell 2 (ΔI_{sc-2}), the measurement error of DNI voltage (ΔV_{DNI}) and the measurement error of GSI voltage (ΔV_{GSI}) as shown in the following expression:

$$\left(\frac{\Delta C_{measured}}{C_{measured}}\right)^2 = \left(\frac{\Delta I_{sc-1}}{I_{sc-1}}\right)^2 + \left(\frac{\Delta I_{sc-2}^{DNI}}{I_{sc-2}^{DNI}}\right)^2 + \left(\frac{\Delta V_{DNI}}{V_{DNI}}\right)^2 + \left(\frac{\Delta V_{GSI}}{V_{GSI}}\right)^2 \quad (4)$$

$$\Delta C_{measured} = \sqrt{\left[\left(\frac{\Delta I_{sc-1}}{I_{sc-1}}\right)^2 + \left(\frac{\Delta I_{sc-2}^{DNI}}{I_{sc-2}^{DNI}}\right)^2 + \left(\frac{\Delta V_{DNI}}{V_{DNI}}\right)^2 + \left(\frac{\Delta V_{GSI}}{V_{GSI}}\right)^2\right]} C_{measured} \quad (5)$$

where ΔI_{sc-1} and ΔI_{sc-2} are ±1.2%; ΔV_{DNI} and ΔV_{GSI} are ±0.8% as provided in the instruction manual of the multimeter [55]. Given that DNI = V_{DNI}/8.11 and GSI = V_{GSI}/8.22, both values of 8.11 and 8.22 are constants as provided by the specifications of the pyranometer and the pyrheliometer respectively.

In the case study, we used fourteen POF's with specification as revealed in Table 1 to guide the sunlight from the 2S-NISC prototype to the test room. Seven optical fibers were grouped as one bundle in a hexagonal arrangement and the second bundle was made an exact replica of the first bundle. The optical fibers were first prepared in the laboratory by cutting each to a length of 10 m, followed by polishing the surface using different grades of sandpapers from the most coarse to the finest grade (600, 800, 1000, 1200 & 1500) to achieve an even and smooth surface. The surface roughness of optical fiber is an important factor to determine the light coupling efficiency between air and fiber. In the region of uniform illumination area (38 mm × 38 mm) of the prototype, two bundles of optical fibers were fixed firmly with entrance aperture oriented perpendicularly relative to the incident sunlight as illustrated in Fig. 7. The other end of the fiber was connected to the test room where the illuminance from the optical fibers was measured using a digital light meter (MASTECH MS6612 with a spectral range between 320 nm and 730 nm).

Inside the test room, the indoor illuminance was measured at a distance of 2 m from the exit aperture of the optical fibers at different times of the day when the DNI was found stable. The background illuminance values were subtracted from the measured indoor illuminance values in the test room during data collection. The experimental setup to measure the indoor illuminance of the active daylighting system using the 2S-NISC prototype inside the test room was similar to the previous experiment except that CPV cell 1 was replaced by the optical fibers. The experiments were conducted on 30th December 2016 and 16th February 2017 in which all the five parameters (DNI, GSI, illuminance, short-circuit currents for both CPV cell 1 and CPV cell 2) were recorded concurrently.

In Table 4, the deviation between experimental and theoretical results increases sharply from 7% at 14:06 h to 20% at 14:50 h and slightly reduces to 15% at 15:04 h on 30th December 2016. In Table 5, the deviation also increases suddenly from 14% to 26% during the local time from 14:05 h to 14:06 h, but it dropped significantly from 20% to 11% during the local time between 14:07 h and 14:09 h on 16th February 2017. These phenomena indicated that the deviation could be caused by both systematic and random errors. Systematic error is mainly caused by the pointing error of

Please cite this article in press as: Chong K-K et al. Design and construction of active daylighting system using two-stage non-imaging solar concentrator. Appl Energy (2017), http://dx.doi.org/10.1016/j.apenergy.2017.05.188

Table 4
Comparison between experimental and theoretical results for indoor illuminance using fourteen 10 m long plastic optical fibers connected to the prototype of the active daylighting system on 30th December 2016.

Local time (h)	DNI (W/m^2)	Indoor illuminance (lx)		Deviation between experimental and theoretical results (%)	Uncertainty of experimental result for indoor illuminance (lx)
		Experimental result	Theoretical result		
13:56	851	92.0	91.9	0.0	±5.5
14:00	863	92.7	93.3	1.0	±5.6
14:06	802	80.8	86.6	7.0	±4.8
14:50	913	78.4	98.6	20.0	±4.7
14:53	913	79.6	98.6	19.0	±4.8
14:55	913	77.4	98.6	21.0	±4.6
15:00	900	79.2	97.2	19.0	±4.8
15:02	913	81.3	98.6	17.0	±4.9
15:04	913	84.0	98.6	15.0	±5.0
15:06	888	82.5	95.9	14.0	±4.9
15:11	900	71.4	97.2	27.0	±4.3

Table 5
Comparison between experimental and theoretical results for indoor illuminance using fourteen 10 m long plastic optical fibers connected to the prototype of the active daylighting system on 16th February 2017.

Local time (h)	DNI (W/m^2)	Indoor illuminance (lx)		Deviation between experimental and theoretical results (%)	Uncertainty of experimental result for indoor illuminance (lx)
		Experimental result	Theoretical result		
14:05	900	84.0	97.2	14.0	±5.0
14:06	900	72.1	97.2	26.0	±4.3
14:07	888	76.9	95.9	20.0	±4.6
14:09	888	85.8	95.9	11.0	±5.1
14:11	888	91.3	95.9	5.0	±5.5
14:12	888	88.9	95.9	7.0	±5.3
14:15	888	85.0	95.9	11.0	±5.1
14:16	888	81.8	95.9	15.0	±4.9
14:27	888	82.2	95.9	14.0	±4.9
14:29	888	94.0	95.9	2.0	±5.6
14:31	888	92.7	95.9	3.0	±5.6

the sun-tracking system. In fact, the accuracy of the sun-tracking system relies on the resolution of a 9-bit absolute encoder where the control system only activates the driving system to track the sun after the absolute encoder has sensed the sun position being deviated by 0.70° away from the perfect tracking condition. When the pointing error is increased, the optical fiber at the target area would still receive the focused sunlight but the illuminance output is affected significantly by light transmission loss due to the increase of the incident angle relative to the optical fiber [24]. Despite a higher tolerance of 2S-NISC prototype towards pointing error as compared to the conventional solar concentrator, the increase in the incident angle can still cause more transmitted sunlight to leak out from the optical fiber. To be cost saving in our prototype design, we intentionally employed a lower resolution of absolute encoder to provide a feedback signal of the sun position with the pointing error of up to 0.70° and the experimental result has shown that the transmission loss is still within the acceptable range. On the other hand, random error is mainly caused by the measurement error of the light meter with the uncertainty value of ±6% [56]. The uncertainty of the measured indoor illuminance can be determined as measured indoor illuminance × 6%.

To analyze the performance of the active daylighting system, we compared between experimental and theoretical results of indoor illuminance as shown in Fig. 8. To calculate the theoretical result of the indoor illuminance produced by the prototype of the active daylighting system ($\mathrm{Illum}_{\mathrm{theo}}$), the following formula is applied:

$$\mathrm{Illum}_{\mathrm{theo}} = ((C_{avg} - 1)R_{\mathrm{facet}}^2 + 1) \times \mathbf{I} \times \%VL \times (1 - L_{\mathrm{fiber}}) \times T_{\mathrm{hot\ mirror}} \times E_{\mathrm{L}} \times \frac{A_{\mathrm{fiber}}}{A_{\mathrm{illum}}} \times N_{\mathrm{fiber}} \quad (6)$$

where C_{avg} is the average solar concentration ratio, which is equal to 76 suns in the uniform illumination area; **I** is the direct normal irradiance (W/m^2); A_{fiber} is the cross-sectional area of the plastic optical fiber ($\pi \times 1.5^2$ mm^2);$\%VL$ is the percentage of visible light in the solar spectrum (47%); $T_{\mathrm{hot\ mirror}}$ is the transmissivity of hot mirror to visible light (98%); L_{fiber} is the total transmission loss for a 10 m long plastic optical fiber (45.7%); N_{fiber} is the number of plastic optical fibers (14 fibers); E_{L} is the average value of direct beam luminous efficacy (104 lm/W); A_{illum} is the indoor illuminance area; R_{facet} is the reflectivity of primary/secondary facet mirrors (93.5%).

In the above expression, the indoor illumination area, A_{illum}, has to be determined by perceiving that the light meter is placed at a distance of 2 m from the aperture of the fibers in the test room. From Fig. 9, the indoor illumination area can be computed if the half rim angle (ω) of the solar concentrator is known.

The half-rim angle (ω) of the 2S-NISC prototype is obtained as $\tan^{-1}\frac{31.1}{70} = 24°$, which is also equal to the maximum incident angle of sunrays relative to the entrance aperture of the POF. Since the maximum incident angle of sunrays is 24° relative to the fiber aperture, the maximum exit angle of sunrays should also be 24° and the indoor illumination area at a distance of 2 m from the exit aperture of POF can be attained as 1.586 m^2.

4. Cost analysis of optical fiber based two-stage non-imaging solar concentrator (2S-NISC)

For direct normal irradiance of 1000 W/m^2, the prototype of 2S-NISC with a total collective area of 0.2 m^2 can provide an average illuminance of 500 lx (3921.9 lm) to a room area of 7.8 m^2 via 314 plastic optical fibers. As concluded from section 2.4, the indoor illuminance produced by the 2S-NISC prototype is equivalent to 34

Please cite this article in press as: Chong K-K et al. Design and construction of active daylighting system using two-stage non-imaging solar concentrator. Appl Energy (2017), http://dx.doi.org/10.1016/j.apenergy.2017.05.188

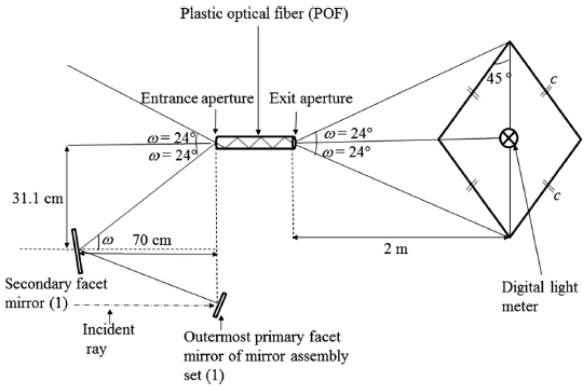

Fig. 9. Diagram to show how the half rim angle and indoor illuminance area are calculated.

Table 6
Summary of estimated breakdown cost for constructing an active daylighting system using two-stage non-imaging solar concentrator (2S-NISC) with collective area of 4 m^2.

	USD
Mechanical support structure	200.00
Flat facet mirrors	131.20
Adjustable frames with screws	100.00
Automatic sun-tracking module	700.00
Base structure and miscellaneous	100.00
Total cost	1231.20

LEDs with the rated electrical power of 37.7 W so that the equivalent power conversion efficiency is found as 22%.

Since the prototype of 2S-NISC with a total collective area of 0.20 m^2 is not a final commercial product, the hardware design and manufacturing cost are not fully optimized. For economic analysis, the optimized collective area of 2S-NISC is proposed as 4 m^2 with the estimated breakdown cost as listed in Table 6 in order to levelize the cost of the sun-tracking system and the mechanical structure. In this design, the total reflective area of the primary reflector is 4 m^2 and total reflective area of the secondary reflector is 2.56 m^2. Based on our previous experience, the collective area of 4 m^2 is the most manageable size for a solar concentrator by considering various factors of practical implementation in which the height of the solar concentrator is about 2 m (close to the average human height) and the total weight of the flat mirrors with a thickness of 3 mm is about 51 kg (manageable by driving devices) [57]. For the flat facet mirrors with a total reflective area of 6.56 m^2, the total cost is only USD 131.20 based on the standard quoted price for a solar grade flat mirror with 3 mm thickness at the price of USD 20/m^2. Nevertheless, the costs of parabolic trough and linear Fresnel lens are USD 400/m^2 and USD 200/m^2 respectively as provided by Ullah et al. [23]. According to Vu et al., the cost of the commercially available automatic sun-tracking module is USD 700 [30]. From Table 5, the total cost of the daylighting system with a total collective area of 4 m^2 can be estimated as USD 1231.20. From our prototype design, the total collective area of 0.2 m^2 can produce the equivalent electrical power of 37.7 W. Proportionally, the total collective area of 4 m^2 can provide indoor illuminance equivalent to the electrical power of 754 W, which is equivalent to USD 1.63 /W.

For economic viability, the payback period of the active daylighting system can be determined by the following formulas [58,59]:

$$n_{pay} = -\frac{\ln\left[1 - S_{total} i'/P_{ann}\right]}{\ln(1+i')} \tag{7}$$

in which

$$\text{in which} \quad i' = \left(\frac{1+i}{1+j}\right) - 1 \tag{8}$$

where i is the interest rate or discounted rate, j is the fuel inflation rate, S_{total} is the total capital cost of the active daylighting system, P_{ann} is the annual energy cost saving (USD/year). For instance, let us consider a discounted form of calculation with the interest rate of 4% if a loan is made to build the active daylighting system with a capacity equivalent to generating 754 W of electricity for lighting up a building and the fuel inflation rate is 2%. The annual energy saving to light up the building can be calculated as 0.754 kW × 6 h/day × 365 days by assuming the annual average of daily direct normal irradiation as 6 kW h/m^2. The annual electrical energy saving by the active daylighting system is 1651.3 kW h, which is equivalent to the annual consumption of USD 214.7 in the electric bill provided that the electricity rate is USD 0.13 per kW h. Table 6 shows the breakdown cost of all the components for constructing the active daylighting system and the total expenses of the whole system is USD 1231.20. With the use of annual saving from the electricity bill to pay for the installment of the loan, the total payback period can be calculated from Eq. (7) as 6.1 years, which is quite reasonable because the daylighting system can last for at least 15 years. On the other hand, the total payback period is found as 5.4 years for undiscounted form by including the fuel inflation rate at 2%. This shows that the active daylighting system using 2S-NISC has the potential of being affordable if it can be mass-produced with an improved mechanical design and light transmission system as compared to the existing fiber optics daylighting systems. The price of the plastic optical fiber varies with its length and 10 m length was only used for experimental purpose. Studies have shown that the shorter the length of the optical fiber, the lesser the losses and the more the transmittance. Therefore, for real-world implementation, the fiber length ranging between 2 m and 6 m would be recommended to transmit daylight from the solar concentrator on the rooftop to the interior parts of a building [23].

Please cite this article in press as: Chong K-K et al. Design and construction of active daylighting system using two-stage non-imaging solar concentrator. Appl Energy (2017), http://dx.doi.org/10.1016/j.apenergy.2017.05.188

Table 7
Comparison between existing daylighting systems and the proposed active daylighting system using two-stage non-imaging solar concentrator (2S-NISC).

	Daylighting Technology	Technical details and performance	Economic and cost-benefit analysis
Single axis tracking	Three-stage reflective type of linear focusing design: Parabolic Trough + parabolic reflector + Trough CPC [23]	Input aperture area of parabolic trough = 1000 mm × 570 mm Focal length of parabolic trough = 450 mm Input aperture area of secondary parabolic reflector = 15 mm × 570 mm Focal length of parabolic reflector = 456.7 mm Input aperture area of Trough CPC = 15 mm × 570 mm 2 mm plastic optical fiber (POF) + silica optical fiber (SOF) matched together with index matching gel are used for light transmission. Total floor area of illumination = 60 m^2 Low solar concentration ratio; less than 100 suns It is expandable while requiring only a single tracking module. A hybrid system where LEDs are used as a complimentary light source.	High-cost design: Parabolic trough costs USD 400/m^2. Automatic tracking module costs USD 400 A complicated optical system consisting of three stages of focusing devices. The costs for the secondary parabolic reflector, trough CPC, and mechanical structure are not provided by the researchers The total cost is more than USD 800/m^2. The prorated cost at a collective area of 4 m^2 is more than **USD 3200**
	Three-stage refractive type of linear focusing design: Linear Fresnel lens + Collimating lens (plano-concave lens) + Trough CPC [23]	Input aperture area of Fresnel lens = 1000 mm × 570 mm Focal length of Fresnel lens = 775 mm Input aperture area of plano-concave lens lens = 15 mm × 570 mm Focal length of plano-concave lens = 23.27 mm Input aperture area of Trough CPC = 15 mm × 570 mm Silica optical fiber (SOF) + 2 mm plastic optical fiber (POF) are used for light transmission Total floor area of illumination = 60 m^2 Linear Fresnel lens is easily manageable and widely available for rapid manufacturing Low solar concentration ratio; less than 100 suns It is expandable while requiring only a single tracking module. A hybrid system where LEDs are used as a complimentary light source	High-cost design: Linear Fresnel lens cost USD 200/m^2 Automatic tracking module costs USD 400 A complicated optical system consisting of three stages of focusing devices. The costs of the plano-concave lens, trough CPC, and mechanical structure are not provided by the researchers The total cost is more than USD 600/m^2 The prorated cost at a collective area of 4 m^2 is more than **USD 2400**
Dual axis tracking	Full spectrum parabolic mirror hybrid daylighting system [25,26]: Primary concentrator (circular parabolic mirror) + Secondary element (cold mirror) + thermal photovoltaic array for electricity generation + light distribution system (flexible large core optical fibers) + Luminaires and controls	Radius of aperture for primary parabolic dish = 0.8 m Radius of curvature of primary parabolic dish = 3.675 m Input radius of the aperture is 0.125 m for secondary optical element integrated with concentrating photovoltaic cell. The distance between primary and secondary concentrators = 1450 mm. Optical fiber with large core diameter of 18 mm is used for light transmission 95% coupling efficiency, assuming 100% reflectivity of the mirrors and no reflection losses coupling into the fiber. Hybrid lighting control system	Projected loss of 50% for single-storey application and additional 15–20% for second-storey applications The cost of manufacturing in commercial quantities is high (about USD 3000 for a 2 m^2 collector that can illuminate only a single-storey building); Installation cost of USD 3/ft^2 The prorated cost at a collective area of 4 m^2 is **USD 6000**
	Hybrid parabolic two-stage daylighting system by Sapia [27]: Sun-tracking primary parabolic collector + secondary collector + 10 m long, 3 mm diameter plastic optical fibers	This work was a theoretical study only. The performance analysis is based on MATLAB simulation result: Diameter of parabolic collector = 2.6 m Total collective area = 4.48 m^2 Parabolic collector efficiency = 95% Diameter of secondary collector = 1.03 m Efficiency of secondary collector = 90% Total number of optical fibers for the system = 145 Input available power = 1344 W Fiber optics efficiency (10 m) = 0.63 Overall system efficiency = 21% Output power = 282.24 W Illumination room area = 100 m^2	Very expensive to be manufactured: 2.6 m diameter parabolic primary concentrator costs 250 euros. Secondary optical element costs 380 euros. Solar tracking system costs 700 euros. Total expected cost of the system with collective area of 4.48 m^2 is 6538 euros (or USD 6995.66 at the rate of 1 euro = 1.07 USD). The prorated cost at a collective area of 4 m^2 is **USD 6246.13**

(continued on next page)

Table 7 *(continued)*

	Daylighting Technology	Technical details and performance	Economic and cost-benefit analysis
		Output light flux obtained = 43,500 lm by assuming that solar light efficiency = 180 lm/W and maximum light flux for each optical fiber = 350 lm	
	Modified optical fiber daylighting system with sunlight transportation in free space [30]: It is comprised of: • Primary concentrator (Point focus Fresnel lens) • Truncated cone tapered plastic optical fiber with 6 mm large core diameter • Collimator (parabolic mirror & convex lens) • Light distributor (Directing flat mirrors & two linear fresnel lenses placed perpendicularly to diffuse parallel light for indoor illumination)	Diameter of Fresnel lens = 340 mm Focal length of Fresnel lens = 350 mm Groove pitch of Fresnel lens = 1 mm Material of Fresnel lens is PMMA Collimator specification: Diameter of parabolic mirror = 50 mm with focal length of 4 mm, diameter of convex lens = 15 mm with focal length of 11 mm, Thickness of concentrating module = 350 mm Distance between Fresnel lens and receiver = 3 mm Uniformity of light on the receiver = 85% Prototype optical system efficiency = 50.7% Degradation of plastic Fresnel lens over time due to the effect of ultraviolet and infrared rays. Very complicated optical system because it consists of many stages of optical devices	High cost for real life implementation: 5 × 5 arrays of Fresnel lens cost (USD 40/lens) = USD 720 The cost of eighteen POFs with 1 m length (the POF price is USD 3.9/m) = USD 70.20 Mechanical bracket costs = USD 1000 18 extended hot mirrors cost = USD 990 18 collimators cost = USD 540 Total cost of 36 mirrors = USD 72 Automatic dual axis sun tracking system costs = USD 700 (Cost of one distributer in mass production is estimated as USD 10) Cost of 18 distributers = USD 180 For a total collective area of 2.27 m^2, the total cost of the whole system = USD 4272 The prorated cost at a collective area of 4 m^2 is **USD 7527.75**
	Two stage non-imaging solar concentrator (2S-NISC) Solar concentrator: Primary reflector & secondary reflector Light guide: Plastic optical fibers	Total reflective area of the primary reflector = 4 m^2 Total reflective area of the secondary reflector = 2.56 m^2. Half rim angle of concentrator = 24° The equivalent power conversion efficiency = 22%. The total collective area of 4 m^2 can provide indoor illuminance equivalent to the electrical power of 754 W The 2S-NISC has the following advantages: 1. The reflectors consisted of only flat mirrors 2. Low rim angle 3. Uniform illumination at the target area 4. High tolerance to pointing error of sun-tracking system	Low-cost design for a collective area of 4 m^2: Cost of primary and secondary flat facet mirrors = USD 131.20 Cost of mechanical support structure = USD 200 Cost of adjustable frames with screws = USD 100 Cost of automatic sun-tracking module = USD 700 Cost of base structure and miscellaneous = USD 100 For a collective area of 4 m^2, the total cost of the system is **USD 1231.20**

For reliability test, we have operated and tested our prototype on the rooftop for one year where the system is robust and stable in performance. Mechanical driving devices such as the stepper motor connected to a sprocket gear engaged with a custom-made gear for azimuth motion and the linear actuator for elevation motion are highly reliable and durable. The control system of the tracking system can track the sun as programmed and there has been no malfunction. The solar grade facet mirrors specially designed for outdoor operations are durable and the reflectivity can be maintained well after one year of operation. The adjustable frame with screws used to hold the mirrors in their aligned positions is rigid and remain in their fixed position after one year.

Table 7 presents a comparison of our active daylighting system with some selected existing fiber optics daylighting systems in terms of technical details, performance, economic and cost-benefit analysis.

According to the economic analysis as listed in Table 7, the 2S-NISC system has been demonstrated as the most cost-effective system among all the active daylighting systems with the lowest manufacturing cost of USD 1231.20 at a collective area of 4 m^2. In practice, the active daylighting system using 2S-NISC would be installed on the rooftop and the concentrated sunlight is guided and distributed by using plastic optical fibers to different rooms in the building. The total collective area of 2S-NISC is determined by the total space area of the building needed to be illuminated. For illuminating the room, hybrid lighting system is recommended so that the exit apertures of plastic fibers and the LEDs are positioned in an alternating arrangement to form a 2-D array, and then covered by the diffusers to provide uniform indoor illumination. To maintain consistent illuminance at all times, the illumination level of the LEDs would be adjusted to compensate the fall of daylight from the required illuminance standard. An electrical lighting control system with a photosensor is used to maintain the standard illuminance level of the interior via closed loop feedback system. To optimize the transmission loss in the fibers, the 2S-NISC should be placed on the rooftop of a building with a maximum height of not more than two storeys so that every corner of the interior space is achievable by the plastic optical fibers with a maximum length of 6 m. The recommended length of plastic optical fiber to have good transmittance is about 6 m in which a 3 m long fiber gives a transmittance of 87% and an 8 m long fiber gives a transmittance of 72% [23]. However, a much longer fiber length is possible if low loss fused silica optical fiber can be manufactured at an affordable price.

5. Conclusion

The design and construction of active daylighting system using 2S-NISC have been presented and evaluated in detail. From our calculation, the prototype of active daylighting system with collective area of 0.2 m^2 is capable of uniformly illuminating an office area of 7.8 m^2 with average illuminance of 500 lx. This indoor illuminance is equivalent to 34 LEDs with rated electrical power of 37.7 W. Considering the input solar power of 170 W, the power conversion efficiency of 2S-NISC prototype can be determined as 22%. From the numerical simulation, the average solar concentration ratio of prototype is 76 suns and the percentage of energy within the uniform illumination area is 57.3%. The percentage of energy is increased to 74.6% for C_{avg} of more than 60 suns, and the percentage of energy becomes 88.7% for C_{avg} of more than 38 suns. With reasonably uniform solar flux distribution produced by 2S-NISC, it is highly recommended for the active daylighting system. The measured solar concentration ratio of the 2S-NISC prototype fluctuated between 62 suns and 74 suns in such a way that the average measured solar concentration ratio is 66.6 suns with a standard deviation of 3.0 suns. Comparing with the simulated solar concentration ratio of 76 suns, the reflectivity of the facet mirror can be estimated as 93.5%.

In Table 4, the deviation between experimental and theoretical results increases sharply from 7% at 14:06 h to 20% at 14:50 h and slightly reduces to 15% at 15:04 h on 30th December 2016. In Table 5, the deviation also suddenly increases from 14% at 14:05 h to 26% at 14:06 h but then dropped significantly from 20% at 14:07 h to 11% at 14:09 h on 16th February 2017. These phenomena indicated that the deviation could be caused by both systematic (due to pointing error of the sun-tracking system) and random errors (due to measurement error of the light meter). To be cost saving in our prototype, we intentionally employed a lower resolution 9-bit absolute encoder to provide feedback signal of the sun position with the pointing error of 0.70°. The experimental result has shown that the transmission loss caused by the low tracking accuracy is still within the acceptable range.

Since the prototype of 2S-NISC with total collective area of 0.20 m^2 is not a final commercial product manufactured in mass quantity, the hardware design and construction costs are not fully optimized. For economic analysis, the optimized collective area of 2S-NISC is proposed as 4 m^2 with the total estimated cost of USD 1231.20 to levelize the cost of the sun-tracking system and the mechanical structure. With the use of annual saving from the electric bill to pay for the installment of the loan at the interest rate of 4% and fuel inflation rate of 2%, the total payback period can be calculated as 6.1 years, which is quite reasonable because the active daylighting system can have a lifetime of more than 15 years. On the other hand, the total payback period is calculated as 5.4 years for undiscounted form with the fuel inflation rate of 2%. For a comparison with some existing fiber optics daylighting designs, our daylighting system has shown its significance in energy saving, cost-effectiveness and having great potential for commercial application.

Acknowledgements

The authors would like to express their sincere gratitude to Ministry of Energy, Green Technology, and Water (AAIBE Trust Fund) with vote account 4356/001. Furthermore, authors would like to thank UTAR Research Fund 2014 Cycle 2 with project number IPSR/RMC/UTARRF/2014-C2/C02 (vote account 6200/C91) and UTAR Research Fund 2016 Cycle 2 with project number IPSR/RMC/UTARRF/2016-C2/C04 (vote account 6200/CC2) for their financial support.

References

[1] Chhetri AB, Islam MR. Inherently-sustainable technology developments. New York: Nova Science Publishers, Inc.; 2008.
[2] International Energy Agency (IEA). Light's labour's lost: policies for energy-efficient lighting. France: IEA Publications; 2006.
[3] Baggini A, Sumper A. Electrical energy efficiency: technologies and applications. United Kingdom: John Wiley and Sons; 2012.
[4] EIA (US Energy Information Administration). Independent statistics and analysis: how much electricity is used for lighting in the United States; 2017.
[5] US Census Bureau. 2006 Manufacturing energy consumption survey. US Census Bureau, Washington; 2007.
[6] USDA Natural Resources Conservation Service. Conserving energy in agricultural lighting. Energy conservation series. NRCS New Jersey, Somerset, NJ; 2012.
[7] Martirano LA. Smart lighting control to save energy. In: Proceedings of the 2011 IEEE 6th international conference on intelligent data acquisition and advanced computing systems (IDAACS), Prague, Czech Republic, 15–17 September; 2011, p. 132–8.
[8] TERI. The Energy and Resources Institute. Regional report on the transition to efficient lighting in South Asia, New Delhi; 2014.
[9] Al-Mofleh A, Taib S, Mujeebu M, Salah W. Analysis of sectoral energy conservation in Malaysia. Energy 2009;34:733–9.
[10] Zakaria R, Foo KS, Zin R Mohamad, Yang J, Zolfagharian Samaneh. Potential retrofitting of existing campus buildings to green buildings. Appl Mech Mater 2012;178–181:42–5.

Please cite this article in press as: Chong K-K et al. Design and construction of active daylighting system using two-stage non-imaging solar concentrator. Appl Energy (2017), http://dx.doi.org/10.1016/j.apenergy.2017.05.188

[11] International Energy Agency (IEA). 25 Energy policy recommendations. France; 2011.
[12] U.S. Green Building Council. Green building rating systems - draft recommendations for a U.S. rating system. Bethesda (MD); 1995.
[13] Chow SKH, Li DHW, Lee EWM, Lam JC. Analysis and prediction of daylighting and energy performance in atrium spaces using daylight-linked lighting controls. Appl Energy 2013;112:1016–24.
[14] Galasiu AD, Atif MR, MacDonald RA. Impact of window blinds on daylight-linked dimming and automatic on/off lighting controls. Sol Energy 2004;76:523–44.
[15] Jenkins D, Newborough M. An approach for estimating the carbon emissions associated with office lighting with a daylight contribution. Appl Energy 2007;84:602–22.
[16] Zain-Ahmed A, Sopian K, Othman M, Sayigh A, Surendran P. Daylighting as a passive solar design strategy in tropical buildings: a case study of Malaysia. Energy Convers Manage 2002;43:1725–36.
[17] Elmualim AA, Smith S, Riffat SB, Shao L. Evaluation of dichroic material for enhancing light pipe/natural ventilation and daylighting in an integrated system. Appl Energy 1999;62:253–66.
[18] Berardi U. The development of a monolithic aerogel glazed window for an energy retrofitting project. Appl Energy 2015;154:603–15.
[19] Kim W, Jeon Y, Kim Y. Simulation-based optimization of an integrated daylighting and HVAC system using the design of experiments method. Appl Energy 2016;162:666–74.
[20] Pohl W, Anselm C. Report of EC-funded Joule-Craft research project: development of an economic and energy saving heliostat technology for room illumination, publishable final report, contract no. JOR3-CT98-7042. Aldrans: Bartenbach LichtLabor GmbH; 2001.
[21] Ullah I, Whang AJ. Development of optical fiber-based daylighting system and its comparison. Energies 2015;8:7185–201. http://dx.doi.org/10.3390/en8077185.
[22] Ghisi E, Tinker JA. Evaluating the potential for energy savings on lighting by integrating fiber optics in buildings. Build Environ 2006;41(12):1611–21.
[23] Ullah I, Shin S. Highly concentrated optical fiber-based daylighting systems for multi-floor office buildings. Energy Build 2014;72:246–61.
[24] Song J, Zhu Y, Jin Z, Yang Y. Daylighting system via fibers based on two-stage sun-tracking model. Sol Energy 2014;108:331–9. http://dx.doi.org/10.1016/j.solener.2014.07.021.
[25] Muhs J. Design and analysis of hybrid solar lighting and full-spectrum solar energy systems July. Madison (Wisconsin): American Solar Energy Society's; 2000. p. 16–21.
[26] Schlegel G, Burkholder F, Klein S, Beckman W, Wood B, Muhs J. Analysis of a full spectrum hybrid lighting system. Sol Energy 2004;76(4):359–68.
[27] Sapia C. Daylighting in buildings: developments of sunlight addressing by optical fiber. Sol Energy 2013;89:113–21.
[28] Ullah I, Shin S. Concept of solar tower for daylighting in multi-floor buildings. J Green Sci Technol 2013;1(2):79–84.
[29] Ullah I, Shin S. Development of optical fiber-based daylighting system with uniform illumination. J Opt Soc Korea 2012;16:247–55.
[30] Vu N-H, Pham T-T, Shin S. Modified optical fiber daylighting system with sunlight transportation in free space. Opt Express 2016;24:26.
[31] Chong KK, Siaw FL, Wong CW, Wong GS. Design and construction of non-imaging planar concentrator for concentrator photovoltaic system. Renew Energy 2009;34:1364–70. http://dx.doi.org/10.1016/j.renene.2008.09.001.
[32] Chong KK, Wong CW, Siaw FL, Yew TK. Solar flux distribution analysis of non-imaging planar concentrator for the application in concentrator photovoltaic system. Conf Rec IEEE Photovolt Spec Conf 2010;132:3013–8. http://dx.doi.org/10.1109/PVSC.2010.5614112.
[33] Chong KK, Wong CW, Yew TK, Tan MH. Solar concentrator assembly. US patent, application no: 13/901,519 (pending) filed on 23rd May 2013.
[34] Chong KK, Wong CW, Yew TK, Tan MH. Dense-array concentrator photovoltaic system utilizing non-imaging dish concentrator and array of crossed compound parabolic concentrators. US patent, application no: 14/462,891 (pending) filed on 19th August 2014.
[35] Wong CW, Chong KK, Tan MH. Performance optimization of dense-array concentrator photovoltaic system considering effects of circumsolar radiation and slope error. Opt Express 2015;23:A841–57.
[36] Yew TK, Chong KK, Lim BH. Performance study of crossed compound parabolic concentrator as secondary optics in non-imaging dish concentrator for the application of dense-array concentrator photovoltaic system. Sol Energy 2015;120:296–309.
[37] Siaw FL, Chong KK, Wong CW. A comprehensive study of dense-array concentrator photovoltaic system using non-imaging planar concentrator. Renew Energy 2014;62:542–55.
[38] Chong KK, Lau SL, Yew TK, Tan PCL. Design and development in optics of concentrator photovoltaic system. Renew Sustain Energy Rev 2013;19:598–612.
[39] Tan MH, Chong KK, Wong CW. Optical characterization of nonimaging dish concentrator for the application of dense-array concentrator photovoltaic system. Appl Opt 2014;53:475–86.
[40] Tan MH, Chong KK. Influence of self-weight on electrical power conversion of dense-array concentrator photovoltaic system. Renew Energy 2015;87:445–57.
[41] Chong KK, Wong CW, Siaw FL, Yew TK. Optical characterization of nonimaging planar concentrator for the application in concentrator photovoltaic system. J Sol Energy Eng 2010;132:011011.
[42] Lim BH, Chong KK, Lim CS, Lai AC. Latitude-orientated mode of non-imaging focusing heliostat using spinning-elevation tracking method. Sol Energy 2016;135:253–64.
[43] Chong KK, Tan MH. Range of motion study for two different sun-tracking methods in the application of heliostat field. Sol Energy 2011;85:1837–50.
[44] Chong KK, Tan MH. Comparison study of two different sun-tracking methods in optical efficiency of heliostat field. Int J Photoenergy 2010;1–10.
[45] Chen YT, Chong KK, Bligh TP, Chen LC, Jasmy Y, Kannan KS, et al. Non-imaging focusing heliostat. Sol Energy 2001;71(3):155–64.
[46] Chen YT, Chong KK, Lim BH, Lim CS. Study of residual aberration for non-imaging focusing heliostat. Sol Energy Mater Sol Cells 2003;79(1):1–20.
[47] Chen YT, Chong KK, Lim CS, Lim BH, Tan BK, Lu YF. Report on the second prototype of non-imaging focusing heliostat and its application in food processing. Sol Energy 2005;79(3):280–9.
[48] Chen YT, Chong KK, Lim CS, Lim BH, Tan KK, Omar A, Bligh TP, Tan BK, Ghazally I. Report of the first prototype of non-imaging focusing heliostat and its application in high temperature solar furnace. Sol Energy 2002;72(6):531–44.
[49] Chen YT, Kribus A, Lim BH, Lim CS, Chong KK, Karni J, Buck R, Pfahl A, Bligh TP. Comparison of two sun tracking methods in the application of heliostat field. ASME J Sol Energy Eng 2004;126(1):1–7.
[50] Chong KK. Optical analysis for simplified astigmatic correction of non-imaging focusing heliostat. Sol Energy 2010;84(8):1356–65.
[51] Chong KK. Optimization of nonimaging focusing heliostat in dynamic correction of astigmatism for a wide range of incidence angles. Opt Lett 2010;35(10):1614–6.
[52] Chong KK, Lim CY, Hiew CW. Cost-effective solar furnace system using fixed geometry Non-Imaging Focusing Heliostat and secondary parabolic concentrator. Renew Energy 2011;36(5):1595–602.
[53] Lim Y, Ahmad MH. Daylighting as a sustainable approach for high-rise office in tropics. Intl J Real Estate Stud 2013;8(1):31–42.
[54] Golden DRAGON plus Datasheet Version 1.1. LUW W5AM.OSRAM Opto Semiconductors GmbH; 2015 [viewed 5 April 2016].
[55] User manual for GW INSTEK GDM-394/396.
[56] Instruction manual for MASTECH Digital Light Meter MS6612.
[57] Chong KK, Yew TK, Wong CW, Tan MH, Tan WC, Lim BH. Dense-array concentrator photovoltaic prototype using non-imaging dish concentrator and an array of cross compound parabolic concentrators. Appl Energy; 2017 [in press].
[58] Goswami DY, Kreith F, Kreider JF. Principles of solar energy engineering. 2nd ed. Philadelphia (PA): Taylor & Francis; 1999.
[59] Chong KK, Chay KG, Chin KH. Study of a solar water heater using stationary V-trough collector. Renew Energy 2012;39:207–15.

Please cite this article in press as: Chong K-K et al. Design and construction of active daylighting system using two-stage non-imaging solar concentrator. Appl Energy (2017), http://dx.doi.org/10.1016/j.apenergy.2017.05.188